HIGH-THROUGHPUT SYNTHESIS OF METAL-ORGANIC FRAMEWORKS THROUGH MIXED LIGAND CO-ASSEMBLY AND TOPOLOGICAL DESIGN

A Dissertation

by

STEPHEN A FORDHAM

Submitted to the Office of Graduate and Professional Studies of
Texas A&M University
in partial fulfillment of the requirements for the degree of

DOCTOR OF PHILOSOPHY

Chair of Committee,	Hong-Cai Joe Zhou
Committee Members,	Kim R. Dunbar
	Sarbajit Banerjee
	Hung-Jue Sue
Head of Department,	Simon North

December 2016

Major Subject: Chemistry

ABSTRACT

The focus of this research is to investigate the synthesis of novel mixed linker metal-organic frameworks (MOFs) composed of pyrozolate and imidazolate based linkers through a mixed-ligand co-assembly process. In MOF synthesis, judicious selection of metal containing nodes combined with symmetric ligands can provide a modicum of predictability to the ultimate structure of the framework. Traditionally, carboxylate ligands have been heavily utilized for the construction of porous materials; however, nitrogen based ligands have not been as frequently used. Of the MOF family, zeolitic imidazolate frameworks (ZIFs) have been the most widely studied material composed of nitrogen-based ligands; however, these frameworks have primarily been constructed from only tetrahedral building units with zinc and cobalt metal nodes, which severely limits the diversity of such frameworks.

After an introduction of MOF materials and high throughput synthesis, we investigate the synthesis of new MOFs through mixed-linker co-assembly. An uncommon $Pyrazole_3Cu_3OL_3$ building unit is observed in two new MOFs, PCN-351 and PCN-352. The first MOF, PCN-351 exhibits three distinct channels and small pores. PCN-352 is composed of molecular polyhedral cages and exhibits enhanced porosity and surface area. Additionally, high-throughput synthesis will allow for the systematic study of MOF formation under varying reaction conditions. Structural predictability is often limited, due to the many kinetic and thermodynamic factors that contribute to MOF formation including metal selection, ligand selection (connectivity, bonding angles, solubility, etc.), solvent selection, modulating agents, and pH values. This project will use a Chemspeed

SLT-Swing robotic synthetic platform to exploit combinatorial chemistry methods in MOF synthesis. Utilizing the robotic platform, solvothermal reactions can be screened to optimize MOF formation through selection of solvent, determination of optimal reactant concentrations (metal to ligand ratios, modulation reagents, etc.), and determination of appropriate reaction temperature. This project builds upon the previously discover mixed-linker MOFs using ligand co-assembly. Ligand extension has often been used to study reticular chemistry for the formation of MOFs with enhanced porosity. Herein, we will explore the effect of linker length in the formation and symmetry of MOFs. A series of MOFs have been synthesized using the mixed linker co-assembly procedure and exhibit tuneable surface area and porosity.

Finally, we explore the use of porphyrin linkers in the synthesis of mesoporous MOFs (PCN-228, PCN-229 and PCN-230). Porphyrin linkers are highly conjugated systems that have been shown to eliminate interpenetration of MOFs. In this work a series of elongated porphyrin linkers with Zr_6 metal nodes have been studied and show enhanced porosity and stability. We build upon the synthesis of porphyrin MOFs, using high-throughput synthesis and the mixed ligand co-assembly method, to construct a copper based porphyrin MOF isostructural to the reported zirconium MOFs.

In summary, several new mixed linker MOFs have been developed though a ligand co-assembly process and provide an interesting new direction for the development of materials with enhanced porosity through topological design. Additionally, high-throughput methods are a powerful tool for the synthesis of novel MOFs.

DEDICATION

To Mr. Jason Cole, Dr. Jan Gryko, and Dr. Joe Zhou,

For many years of inspiration, guidance, and a push when needed

ACKNOWLEDGEMENTS

First, I would like to thank the teachers of Ranburne High School for instilling in me the drive to succeed and the ability to take on the world. Thank you to Mr. Jason Cole for sharing your love of science and for pushing me every step along the way.

I would like to acknowledge Mignon C. Smith and the J. Craig and Page T. Smith Scholarship Foundation for the many years of financial and emotional support, specifically Mrs. Mildred Adams, Mrs. Sandy Gannaway, Mr. Urist McCauley, and Mrs. Ahrian Tyler Dudley. I appreciate the wonderful professors at Jacksonville State University, Dr. Al Nichols, Dr. Nixon Mwebi, Dr. Brent Helms, Dr. Nagarajan Vasumathi, Dr. Eugene Knight, and Mr. Doug Nelson for a lifetime of memories and knowledge. A very special thanks to Dr. Jan Gryko for unwavering passion for research and the countless hours of mentorship and guidance. Bernice George and Amy Grano were amazing colleagues and taught me so many of my vital laboratory skills.

I thank Texas A&M University and the Department of Chemistry. I am proud to be part of a wonderful tradition of excellence and a large aggie family. Dr. Hong-Cai Joe Zhou has been a tremendous advisor and mentor. I am very grateful to have been part of this lab and have enjoyed all the challenges and personal development along the way. I appreciate the leader, researcher, and professional you have guided me to become. I appreciate all the wonderfully brilliant researcher from the Zhou research group, both past and present. I thank Dr. Trevor Makal for his exemplary leadership, Ying-Pin Chen for many long hours solving my crystal structures, and Dawei Feng and many other group members for hours of discussions. I would also like to thank Zac Perry and Mat Bosch for

helping to refine my thoughts. A special thanks to Heather Li for the beautiful MOF pictures throughout this work. Undergraduate Students, Mario Cosio, Mitchel Johnson, and Madison Hass greatly contributed to this research and I thank them for all the hard work. I would like to acknowledge my committee members, Dr. Kim Dunbar, Dr. Sarbajit Banerjee, and Dr. Hung-Jue Sue for thoughtful conversation, guidance, and support. My research would not be possible without the support of the Methane Opportunities for Vehicular Energy (MOVE) Program under the Award Number DE-AR0000249 and the Welch Foundation under Award Number A-1725.

I also thank Dr. Greg Halder, Dr. Andrey Yakavenko, and Dr. Yu-Sheng Chen for help with the diffraction studies at Argonne National Laboratory. ChemMatCARS Sector 15 is principally supported by the Divisions of Chemistry (CHE) and Material Research (DMR), National Science Foundation under grant number NSF/CHE-1346572. Research performed at ChemMatCARS and Beamline 17-BM used resources of the Advanced Photon Source, a U.S. Department of Energy (DOE) Office of Science User Facility operated for the DOE Office of Science by Argonne National Laboratory under Contract No. DE-AC02-06CH11357. I thank Dr. Simon Teat at Lawrence Berkeley National Laboratory at Beam lime 11.3.1. Research performed used resources of the Advanced Light Source, supported by the Director, Office of Science, Office of Basic Energy Sciences, of the U. S. Department of Energy under Contract No. DE-AC02-05CH11231.

Lastly, I thank my family and friends for seeing me through till the end. I could not have possibly accomplished this feat without the encouragement and social distractions of so many friends including Bryan and Rachel Sutton, Nathan Harris,

Rachael Ginn, Samantha Gacasan, Autumn Zuchelli, Bart and Caitlin Stevens, Allen and Adriana Lunsford, Jill Ellenbarger, Rita Silbernagel, Xuan Wang, Morgan Shirley, Sandy Horton, Katie Farley, Greg and Shawna Waetzig and many, many more. I am blessed with wonderful parents, Denita Terrell and Allan Fordham, and appreciate all their love and encouragement along the way. I am blessed beyond measure to have loving grandparents and great-grandparents, Bea and Tony Flournoy, Bunk and Irene Capes, Papa Rick Fordham, and Neal and Mary Ola Fordham, who have given me so much love, joy, and wisdom. Lastly, I thank my brothers, Samuel Fordham and Seth Willbanks, for being my pillars and for the steady academic competition. Thank you all.

NOMENCLATURE

ANG	Adsorbed Natural Gas
BET	Brunauer-Emmett-Teller
CNG	Compressed Natural Gas
DMA	*N*,*N*-Dimethyl Acetamide
DMF	*N*,*N*-Dimethyl Formamide
DMSO	Dimethyl Sulfoxide
DOE	United States Department of Energy
LNG	Liquefied Natural Gas
MeOH	Methanol
MOF	Metal-Organic Framework
MOP(s)	Metal-Organic Polyhedron(Polyhedra)
NMR	Nuclear Magnetic Resonance
PCN	Porous Coordination Network
PXRD	Powder X-Ray Diffraction
SBB	Supramolecular Building Block
SBU	Secondary Building Unit
TGA	Thermogravimetric Analysis
ZIF	Zeolitic Imidazolate Framework

TABLE OF CONTENTS

LIST OF FIGURES

Page

Page

Page

LIST OF REACTION SCHEMES

LIST OF TABLES

1. INTRODUCTION*

Metal-organic frameworks (MOFs) as a class of inorganic-organic hybrid materials have become an exceedingly popular field of supramolecular chemistry. Perhaps the most desirable property is the structurally tuneable nature of these advanced materials that lead to a wide array of potential applications. Judicious selection of metal nodes in combination with the infinite array of organic ligands that function as linkers yield an unlimited class of highly porous, functional materials. This section will provide an introduction to traditional MOF materials and provide insight into several classical carboxylate MOF examples. Zeolitic imidazolate frameworks (ZIFs) will be discussed to demonstrate the ability to construct porous materials based with metal-nitrogen bonds. Lastly, the development of MOFs with nitrogen-based linkers will be briefly explored.

* (Pages 2-10) Reproduced with permission from "Lanthanide Metal-Organic Frameworks: Syntheses, Properties, and Potential Applications" Fordham, S.; Wang, X.; Bosch, M.; Zhou, H.-C., In Structure and Bonding, Cheng, P.; Ed. Springer: Berlin Heidelberg, 2015, 163, 1-27. Copyright Springer 2015

Porous materials have attracted a significant amount of attention during the past few decades in scientific and technological research. Porous materials have significant surface area, which makes them capable of adsorbing and interacting with small molecules and ions on their inner surface. Classic inorganic porous materials contain activated carbon, silica gels, activated alumina, molecular sieve, zeolites, and mesoporous silica. Extensive studies have focused on the development of new classes of porous materials, such as MOFs.

Traditional porous materials have limitations of either pore size or surface area. Silica gels, activated carbon, and activated alumina are all amorphous (irregular arrangement of pores) polymers containing micro- and mesopores (micropore is defined as pores smaller than 2 nm and mesopores between 2 and 50 nm) with a wide pore size distribution. From the perspective of materials, the wide pore size distribution, the micropores, and limited surface area hamper the utilization of those pores. MOFs, also known as porous coordination polymers (PCPs), are defined as 1, 2, or 3 dimensional coordination networks with potential porosity.[1-3] MOFs are connected by coordination bonds through self-assembly between inorganic metal-containing units (generally known as secondary building units SBUs) and organic linkers to form a rigid uniform crystalline hybrid materials.[2, 4-6]

In general, MOFs are prepared via solvothermal or hydrothermal reactions, in which metal salts and organic linkers are heated in the presence of high boiling point and polar solvents (dialkyl formamides, dimethyl sulfoxide, or water) in a sealed vessel. In order to prepare a highly crystalline materials in dilute liquid phase condition, a reaction

time of hours to days is needed for the crystallization process.[7] The synthesis of MOFs can be quite delicate due to a variety of factors greatly impacting the formation of crystalline material that can be easily characterized through traditional techniques. In general, the main factors that contribute to MOF formation include temperature, pressure, reactant solubility, pH, and concentrations of metal salts and ligands. These Lewis acid-base reactions often lead to the formation of amorphous precipitate from the rapid deprotonation of the ligand.[8] Several reaction conditions can be modified to improve crystallinity including decreasing the reaction temperature or the addition of acid, such as hydrofluoroboric acid (HBF_4), to slow down ligand deprotonation rate. This often difficult trial-and-error process has led to the growth of combinatorial synthetic methods including high-throughput robotic screening.[9]

MOF-5[10] , one of the most important representatives in the field of MOFs, was first reported by Yaghi *et al.* through diffusion of triethylamine into a solution of zinc (II) nitrate and H_2bdc(1,4-benenedicarboxylic acid) in N, N'-dimethylformamide (DMF) and chlorobenzene. However, the yield of MOF-5 through the diffusion synthesis is low. Therefore, the method was further optimized to a high-yield solvothermal reaction of $Zn(NO_3)_2 .4H_2O$ and H_2bdc in N, N'-diethylformamide (DEF) at 120 ^{O}C for 24 hours.[11] The pore size of MOF-5 was further investigated to be controlled and functionalized by applying the isoreticular chemistry in the similar solvothermal conditions. After weak hydrothermal stability was revealed for MOF-5, attention shifted to other porous materials such as HKUST-1[12], MIL-101[13], and UiO-66[14]. In the effort to shorten the synthesis time and produce high-quality crystals, alternative synthesis methods have been developed,

such as microwave-assisted, sonochemical, electrochemical, and mechanochemical methods.[7]

For the aforementioned MOFs synthesis, a multitude of new MOFs have been developed and extended from several key structures that may be important for the future development and applications of MOFs. The hallmark of those MOFs is their permanent porosity. The MOFs are constructed from the metal units or SBUs[15], formed *in situ* from pre-formed organic linkers through coordination bonds. The adjustment of the geometry, length, ratio, and functional group of the linkers will consequently tune the size and shape of the pores. Based on the number and geometry of carboxylates and elements in the linker, the pre-formed organic linkers could be categorized as ditopic, tritopic, tetratopic, hexatopic, octatopic, mixed, desymetrized, metallo, and N-heterocyclic linkers.[16] In this section, the key discussion will focus mainly on metal units or SBUs with ditopic or tritopic linkers. For MOFs composed of other linkers including phosphonate and sulfonate, detailed reviews have been published.[16-18]

In 1999, MOF-5[10] and HKUST-1[12] were synthesized and characterized to demonstrate their high crystallinity and porosity, the first major breakthroughs of MOF chemistry. MOF-5 was constructed from a 6-connected octahedral $Zn_4O(CO_2)_6$ cluster and ditopic acid terephthalate (bdc) giving an extended 3D cubic framework with square opening of 8 Å and 12 Å. One of the unique benefits of MOFs is that the pore size and the internal pore surface functionalities can be tuned by using pre-designed organic linkers of the same symmetry, which, according to the theory of isoreticular chemistry, will not alter the underlying topology.[19-20] MOF structure is predicable on the premise of forming SBUs

with fixed linking geometries. Using MOF-5 as the prototype material, the 3D porous systems can be functionalized with the organic groups of bromo, amino, n-propyl, n-pentoxy, cyclobutyl, and fused benzene rings.[19] Their pore size can be further expanded with a stepwise expansion to biphenyl, tetrahydropyrene, pyrene, and terphenyl. This IRMOF-n series has open pores that ranging from 2.8 to 28.8 Å (Figure 1).

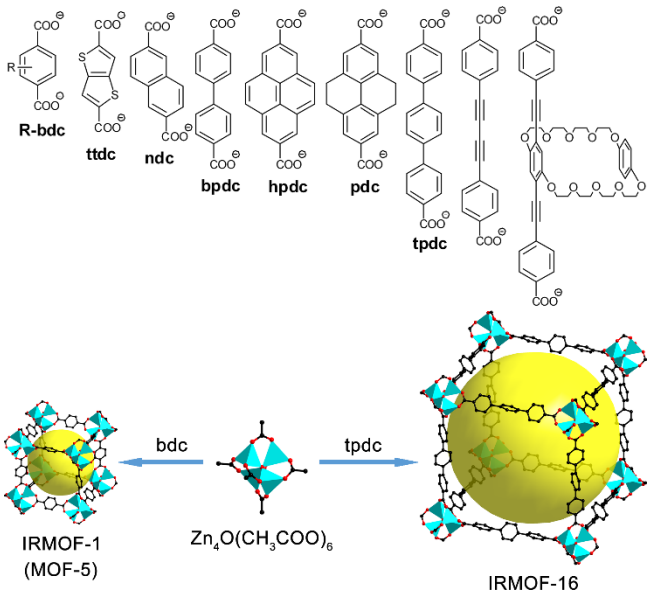

Figure 1 Examples of IRMOF-n series. Color Scheme :Zn (turquoise polyhedral); O (red); C (black). (Reprinted with permission from Lu, W.; Wei, Z.; Gu, Z. Y.; Liu, T. F.; Park, J.; Park, J.; Tian, J.; Zhang, M.; Zhang, Q.; Gentle, T., 3rd; Bosch, M.; Zhou, H. C. *Chemical Society Reviews* **2014,** *43* (16), 5561-93. copyright © 2014 Royal Society of Chemistry)

Another classical MOF, HKUST-1[12] consists of 4-connected square planar dicopper paddle-wheel units as nodes and tritopic 1, 3, 5-benznetricarboxylates (btc) as

linker. Each BTC linker connects to three copper paddle-wheel SBUs forming a T_d – octahedron and occupy the alternating triangular faces of the octahedron. Along with the connection of other units, a cubic framework with tbo topology is formed. However, linking a 4-connected paddle-wheel unit with ditopic acid, such as bdc, result in a two dimensional (2D) sheet rather a three dimensional (3D) MOF material. The various combinations of different carboxylates and metal units would lead to a rich library of MOFs. The marriage of dicopper paddle-wheel units and extended tritopic organic linkers has been investigated to extend the networks and produce a variety of materials with the same network topology.

Combination of elongated tritopic linkers, such as 4,4',4"-s-triazine-1,3,5-triyltri-p-aminobenzoate (tatab), 4,4',4"-(1,3,4,6,7,9,9)-heptaazaphenalene-2,5,8-triyl)tribenzoate (htb), 4,4',4"-s-triazine-2,4,6-triyltribenzoate (tatb), 4,4',4"-(benzene-1,3,5-triyl-tris(benzene-4,1-diyl))tribenzoate (bbc), and paddle-wheel units yield a number of isoreticular MOFs (meso-MOF-1, PCN-htb, PCN-6', and MOF-399, respectively) (PCN stands from Porous Coordination Network) (Figure 2).

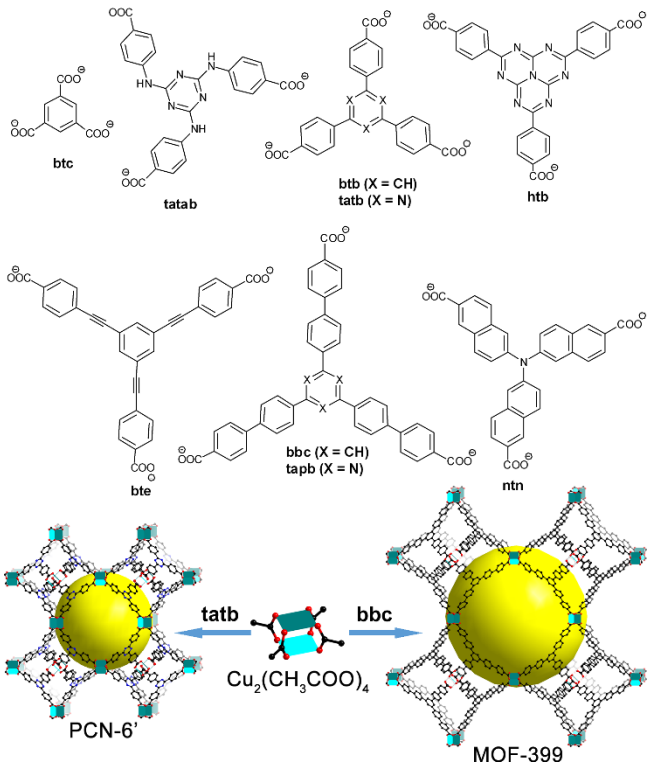

Figure 2 Examples of MOFs constructed from tritopic carboxylate linkers and dicopper paddle-wheel SBUs. Color Scheme: Cu (turquoise); O (red); C (black). (Reprinted with permission from Lu, W.; Wei, Z.; Gu, Z. Y.; Liu, T. F.; Park, J.; Park, J.; Tian, J.; Zhang, M.; Zhang, Q.; Gentle, T., 3rd; Bosch, M.; Zhou, H. C. *Chemical Society Reviews* **2014,** *43* (16), 5561-93. copyright © 2014 Royal Society of Chemistry)

MOF-74[21-22] another well-known example, is the product of the coordination between tetraanionic 2,5-dioxido-1,4-benzene-dicarboxylate (dobdc) and an infinite metal chain, in which both the aryloxide and carboxylate moieties are bonded to the metal units. After applying the isoreticular chemistry of dobdc by the stepwise expansion of long molecular struts with phenylene units, a series of MOF-74 isoreticular materials was synthesized with pore apertures incrementally varied from 14 Å to 98 Å (Figure 3).[23]

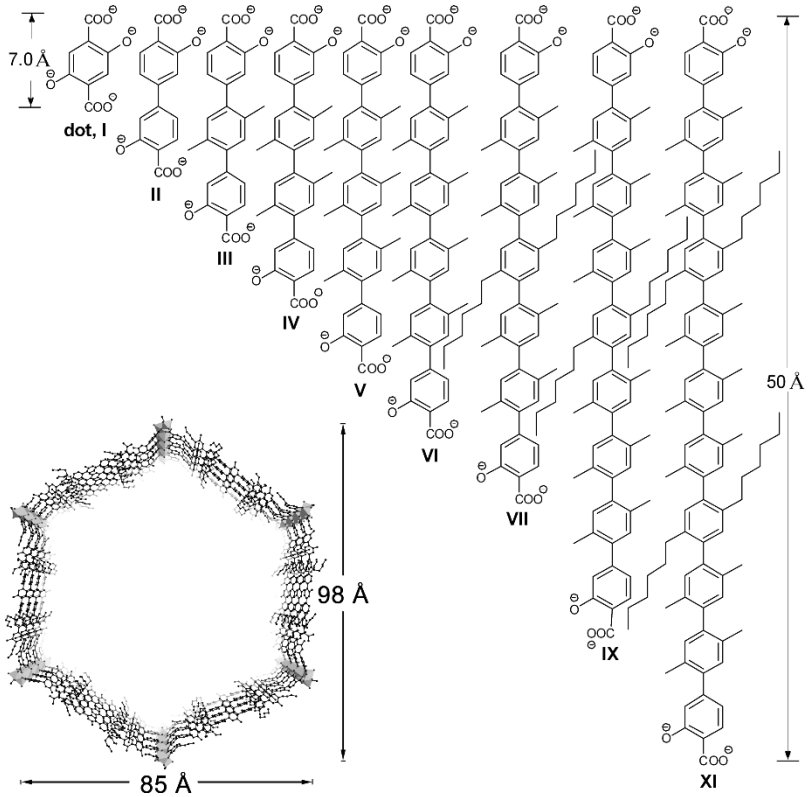

Figure 3 List of organic linkers used in IRMOF-74 series with the one-dimensional channel with 98 Å for IRMOF-74-XI. (Reprinted with permission from Lu, W.; Wei, Z.; Gu, Z. Y.; Liu, T. F.; Park, J.; Park, J.; Tian, J.; Zhang, M.; Zhang, Q.; Gentle, T., 3rd; Bosch, M.; Zhou, H. C. *Chemical Society Reviews* **2014,** *43* (16), 5561-93. copyright © 2014 Royal Society of Chemistry)

To date, IRMOF-74-XI with pore aperture of 98 Å is the record holder for the largest pore among all crystalline materials. Those large pores are capable of allowing natural protein to enter without folding, which demonstrate great potential for MOFs to serve as the matrix for enzyme immobilization.

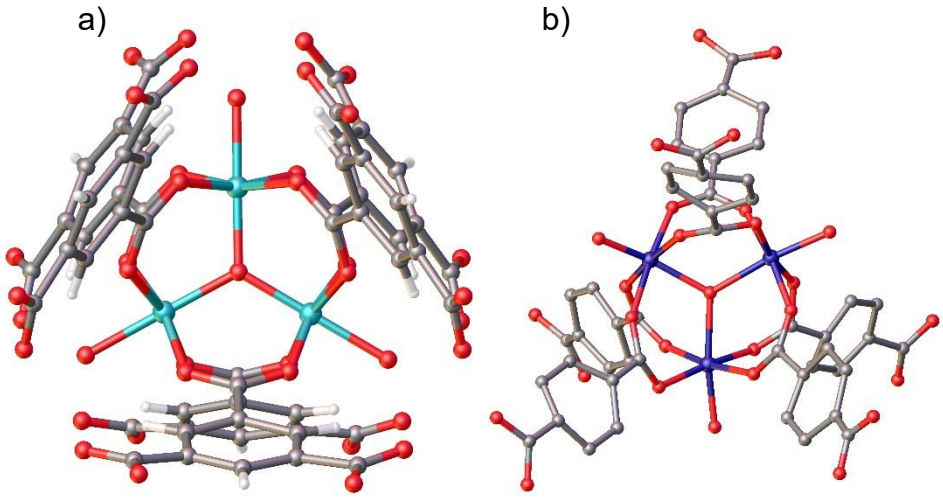

Figure 4 a) MIL-100, Cu SBU with coordinated **btc** linker; b) MIL-101, Cu SBU with coordinated **bdc** linker. Color Scheme: Al (blue, purple); O (red); C (gray).

Besides 6-connected octahedral metal units, another important SBUs is 6-connected trigonal prismatic metal units. MIL-101 (MIL stands for Materials Institute Lavoisier) is a signature MOF, made from the linkage of bdc and metal trimmers, where three trivalent metals each coordinate with four oxygen atoms of bdc, one μ3-O, and one oxygen from terminal water or fluorine group in an octahedral environment.

MIL-101 (Figure 4) is a mesoporous MOF with a hexagonal window of 16 Å and a cage diameter of 34 Å. At the same time, MIL-101 is also acknowledged for enhanced hydrothermal stability through increasing the charge of the metals. Assembling the same trimeric SBUs with tritopic linker btc, MIL-100[24] was successfully synthesized. A so-called “supertetrahedra” is formed with four trimeric metal units as vertices and four btc as the triangular faces. The further connection between these supertetrahedras gives rise to two mesoporous cages with accessible diameters of 25 and 29 Å.

In addition to the aforementioned 4- and 6-conneted SBUs, a 12-connected SBU, $Zr_6O_4(OH)_4$ is identified as a new class of building units to be investigated and explored. In 2008, the first Zr-MOF, UiO-66 (UiO stands for University of Oslo) was synthesized under solvothermal condition using bdc as the organic struts.[14] In the framework of UiO-66, six Zr atoms in the square-antiprismatic coordination environment are linked by eight oxygen atoms from four bdc and four alternatives of μ_3-O and μ_3-OH on the triangle face to form the $Zr_6O_4(OH)_4$ core. In the UIO-66 structure, each $Zr_6O_4(OH)_4$ core is further connected by twelve bdc**,** consequently resulting in a 3D framework with triangular window of 6 Å in diameter. The $Zr_6O_4(OH)_4$ building units have been further applied to achieve desired stable porous materials. Functional groups on bdc[25] and elongated benzene rings[14, 26] have been designed for gas storage and metal sensing. However, MOFs with 12-connected SBUs are still scarce.

In addition to MOFs, Zeolites have long been studied as they currently represent an enormous class of materials widely used in industrial applications and are ubiquitous in nature. Zeolites are crystalline aluminosilicates with tuneable pore size and possess chemical stability under harsh conditions yielding cheap materials that have been commonly used in molecular sieving and gas storage applications.[27] Zeolitic imidazolate frameworks (ZIFs) a class of MOFs with zeolite architectures have recently been developed to mimic the wealth of zeolite structures. ZIFs are primarily composed of tetrahedral metal nodes (M) such as zinc or cobalt bridged with imidazolate (Im) moieties. ZIFs form zeolite structures due to the formation of M-Im-M bonds with a similar angle to the zeolite Si-O-Si bond (145°).[28] A multitude of review articles have thoroughly

explored the synthesis, characterization, and applications of ZIFs[28-32]; however for simplicity, we will focus mainly on a few representative structures and provide insight into key structural features.

ZIFs are increasingly explored due to topological and structural properties that are controlled through synthetic parameters. ZIFs are synthesized under similar reaction conditions as MOFs, usually under hydrothermal or solvothermal reactions. These solvothermal reactions are usually performed with high boiling point solvents, such as dimethylformamide or dimethyl sulfoxide, under varying temperature ranges up to around 200^{o}C over several hours to days. General synthetic conditions for ZIF with structural diversity have been previously reported.[33]

Yaghi *et al.* have provided a comprehensive review of the geometrical design principles of extended solids including ZIFs; some of these principals will be further discussed.[34] ZIFs are evaluated based on the topological net of the structure; these nets are interesting in crystal space in that they represent the space group symmetry. ZIF are categorized by the structural topology, a three-letter code corresponding to zeolite structure or reticular chemistry structure resource (RCSR) code (Figure 5).[28, 32, 35] An example of this naming convention is evident through analysis of common zeolite structures, thus the zeolite framework sodalite has code *sod*; likewise, other common zeolites topologies like diamond and quartz have code *dia* and *qtz*, respectively.[32]

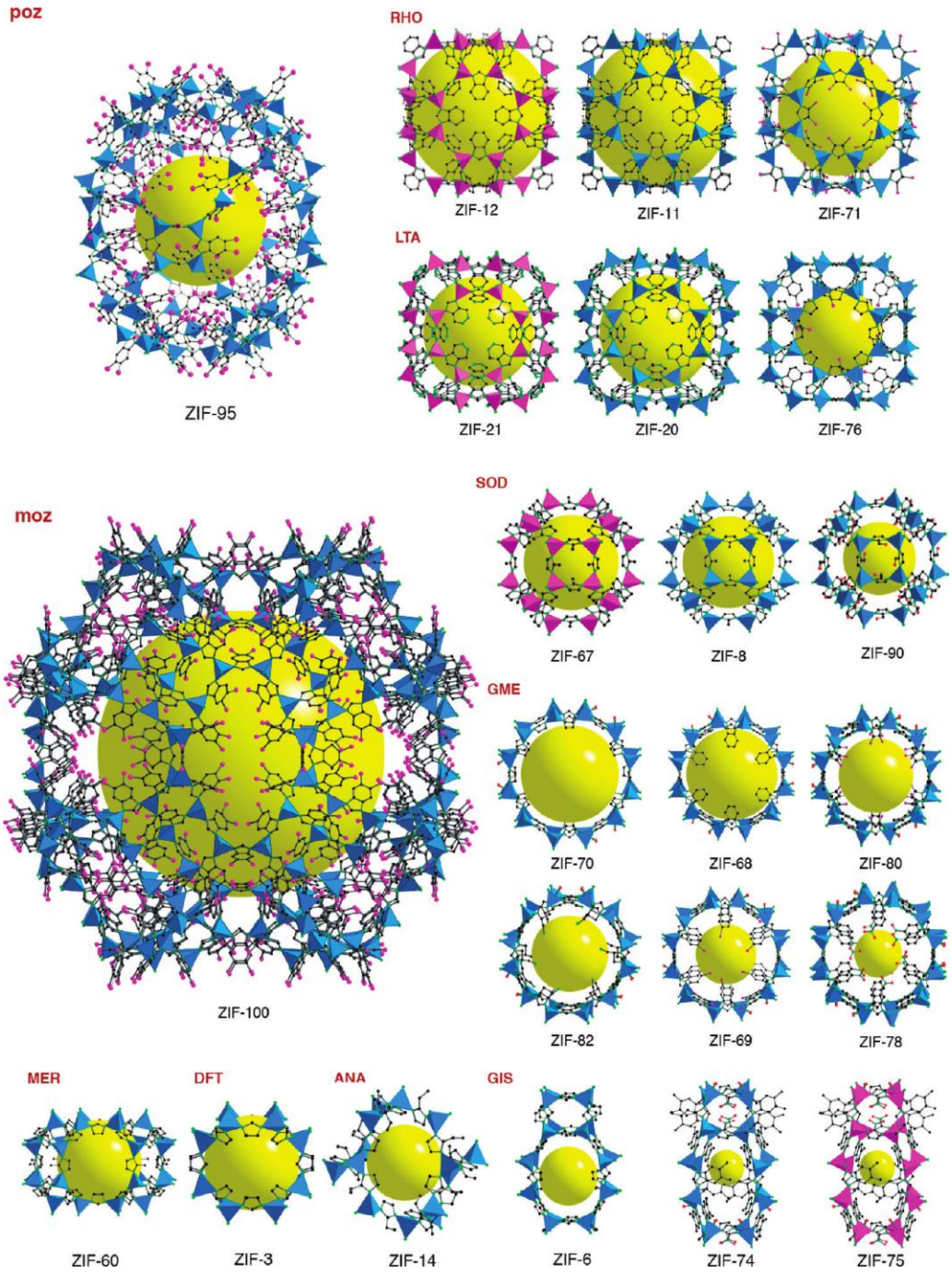

Figure 5 Crystal structures of several representative ZIFs. (Reprinted with permission from Phan, A.; Doonan, C. J.; Uribe-Romo, F. J.; Knobler, C. B.; O'Keeffe, M.; Yaghi, O. M. *Accounts of Chemical Research* **2010,** *43* (1), 58-67, copyright © 2010 American Chemical Society)

The inherent chemical and thermal stability of ZIFs have yielded a robust material that can withstand the harsh condition necessary in some industrial application. Two notable examples that exhibit these properties are ZIF-8 and ZIF-11, which exhibit thermal stability up to 400^{o}C and chemical stability in a variety of solvents including water, toluene, methanol, and aqueous sodium hydroxide.[33] ZIFs with tunable structural properties (Figure 5) were further developed through synthetic approaches including modification of direct synthesis through ligand functionalization, expansion, and augmentation, and post synthetic functionalization.[29]

While the zeolitic structures of ZIFs have contributed to strong stability, the porosity is compromised due to the tetrahedral SBUs. The Zhou group has recently employed the use of soft acid-base interactions to construct materials with enhanced porosity without compromising stability.[36] Using nitrogen based moieties as linkers to form MOFs have led to materials that exhibit improved base stability over traditional soft metal-carboxylate MOFs.[36-37] The research in this dissertation will seek to use previously explored pyrazolate clusters (Figure 6) with imidazolate connecting linkers.

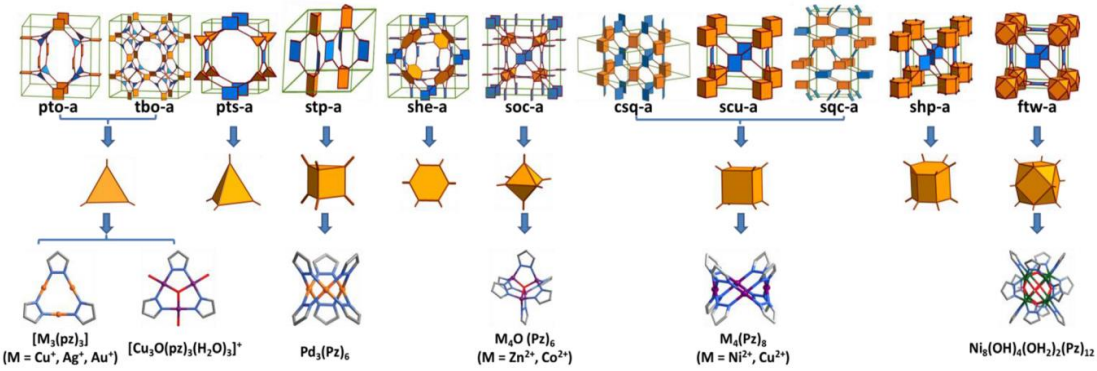

Figure 6 Top-down topological analysis: binodal edge-transitive topologies with planar 4-connected nodes (top line), the nodes assigned to SBUs in corresponding nets (middle line), and reported Pz-based SBUs with the same symmetries and connectivities to corresponding nodes (bottom line).[33, 38-45] (Reprinted with permission from Wang, K.; Lv, X.-L.; Feng, D.; Li, J.; Chen, S.; Sun, J.; Song, L.; Xie, Y.; Li, J.-R.; Zhou, H.-C. *Journal of the American Chemical Society* **2016,** *138* (3), 914-919, copyright © 2010 American Chemical Society)

2. HIGH-THROUGHPUT SYNTHESIS OF METAL-ORGANIC FRAMEWORKS

High-throughput synthesis is a powerful tool for the discovery of novel metal-organic frameworks (MOFs). Since MOFs possess tunable structural features, combinatorial chemistry is often used to develop protocols for the synthesis of new materials. A variety of factors influence the formation of metal-organic frameworks through solvothermal synthesis including solvent, metal-ligand concentration ratios, reaction temperature, co-ligand concentration, co-solvents, and modulating reagent concentration. The use of a high-throughput synthetic protocol allows for the elucidation of the optimal synthetic parameters for metal-organic framework formation. Utilizing a robotic system allows for the screening of a large number of reaction conditions for synthetic trends while minimizing the time of new material development. Herein, applications of high-throughput methods to the synthesis of MOFs will be discussed.

Metal-organic frameworks (MOFs) are a class of inorganic-organic hybrid materials that are highly porous materials with tunable structures. MOFs are usually synthesized under solvothermal reaction conditions, a complex multicomponent system, resulting in multiple variables that contribute to MOF formation. Testing each individual component's contribution to MOF formation by hand would require a time consuming, expensive process with a large number of reactions. This has led to the investigation of high-throughput synthesis with the goal of rapidly studying reaction parameters that contribute to the formation of these new materials. Using combinatorial methods generates a large amount of data and for effective reaction control several key factors must be considered including experimental design, solution preparation, synthesis, product isolation,

characterization, and big data analysis.[46] As new MOF and composite materials are discovered, commercialization becomes increasing more important. Therefore, several unconventional synthetic techniques utilizing high-throughput method have been developed including electrochemical, microwave assisted, mechanochemical, and sonochemical synthesis (Figure 7).[47-49]

Although several robotics companies now offer advanced platforms for high-throughput synthesis, the fully automated synthesis of MOFs is still challenging.[50] Once a new material is synthesized, the resulting powder must be separated from the reaction mixture and then characterized. Powder X-ray diffraction is often used to evaluate the formation of MOFs, lower angle peaks often indicate the present of a large unit cell usually observed with MOF materials. Automated systems for powder x-ray diffraction are often available through instrument manufacturers. This allows for screening of large amounts of reaction conditions.

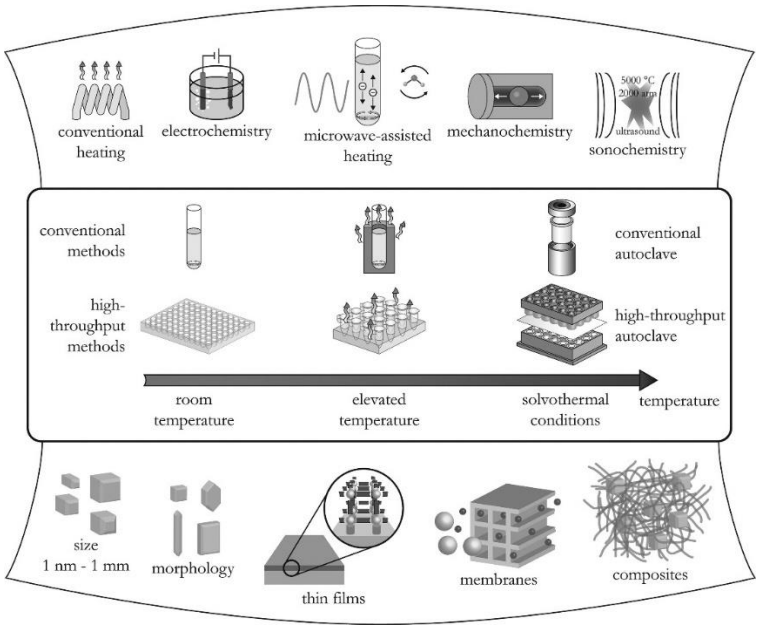

Figure 7 Different synthesis methods of MOFs. (Reprinted with permission from Stock, N.; Biswas, S. *Chemical Reviews* **2012,** *112* (2), 933-969, copyright © 2012 American Chemical Society)

Due to multiple connection modes of transition metals, multiple phases of MOFs or mixed-phase materials might be present. Data analysis then becomes essential to the complete characterization of these materials, which will elucidate key reaction parameters. Currently there is a limited amount of ability to compare experimental diffraction patterns to the expanse collection of reported MOFs. This ultimately requires that the characterization of MOF be completed with single crystal X-ray diffraction. This process can be very time consuming and requires highly crystalline materials for characterization. Thus for the greatest potential for success, the design of the experiment is the most important factor. Therefore a factorial approach is often used, a limited number of

variables are tested in order to reduce the chemical knowledge or intuition needed to rationalize the effects on MOF formation.[46]

Although synthetic platforms may vary in customization and automation, most platforms function with an axis-controlled robotic arm that operates various automated tools. One example of a common system is the Chemspeed® Swing-II robotic synthetic platform (Figure 8); this instrument is highly customizable with over forty synthetic tools, automation software, and a large selection of reaction vessels. For MOF synthesis, common tools include a volumetric transfer unit, gravimetric solid dispensing unit, vortexing racks, cryostat, and capper for pressurized reactions. The setup of the platform is highly dependent on the synthetic goals of a particular experiment, other tools are necessary for complete automated synthesis and characterization. The Swing unit has the capability to interface with peripheral instrumentations such as a gas chromatograph or powder x-ray diffractometer which could aid in the complete characterization of MOFs and ligand. Reaction vessels depend on the scale and desired temperature of the solvothermal reaction.

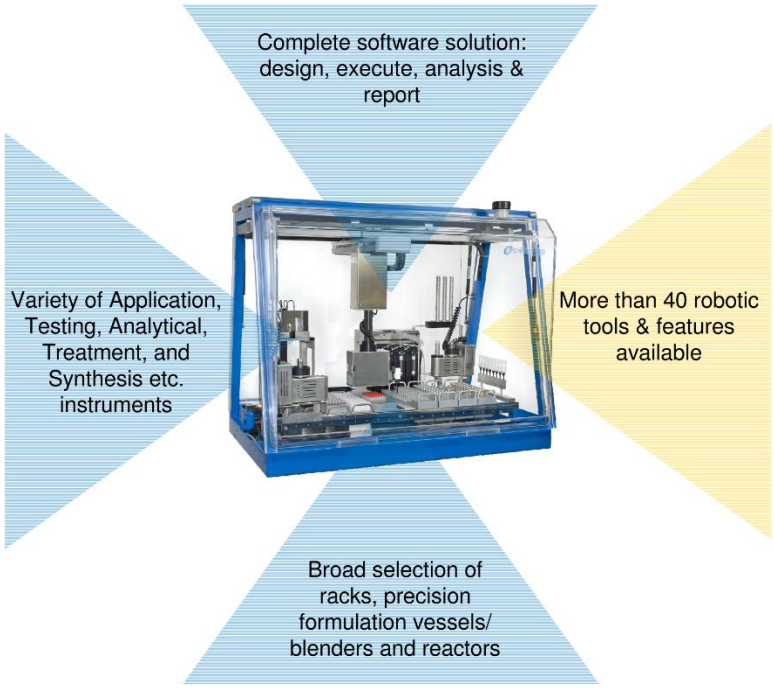

Figure 8 Chemspeed® Swing II robotic synthetic platform. Copyright © Chemspeed® Technologies

Herein, we will discuss a small set of reaction variables that influence the formation of several notable MOFs, mainly MIL-101, MOF-5, and HKUST-1.[10, 12-13] Using a factorial approach, common variables tested in high-throughput methods include reaction solvent, starting material ratios, reaction temperature and time, and the use of modulating reagents. Perhaps one of the most vital components of the solvothermal reaction is the solvent selection. During a solvothermal reaction, the solvent has several chemical roles including directing lattice formation, interacting with the framework as guest molecules, and inducing coordination between metal and ligand ions.[51] Several studies have shown a strong correlation between the reaction solvent and the resulting

MOF structure and properties.[52-54] When evaluating the effects of solvent on MOF formation, two different scenarios should be considered: the effect of using different reaction solvent media, or using mixed solvent reaction media.

Another key factor, reaction temperature, can be used for kinetic and thermodynamic control of the formation of MOFs. Temperature drives the formation of the MOF, providing the activation energy for the cleaving of bonds and the generation of new coordination bonds. Several studies have shown kinetic control through modulation of solvothermal reaction temperature.[55-56] Increasing the reaction temperature is a method to increase the dissociation of the coordination bonds; however, this causes an imbalance in dissociation/substitution rates and has led to the addition of modulating reagents which enhance substitution rate.[57] Lastly, molar ratios of starting materials play a key role in the stoichiometric control of the MOF formation. Stoichiometric changes in metal and linker concentrations can often lead to the formation of coordination clusters, alternate phase MOFs, or mixed phase materials.

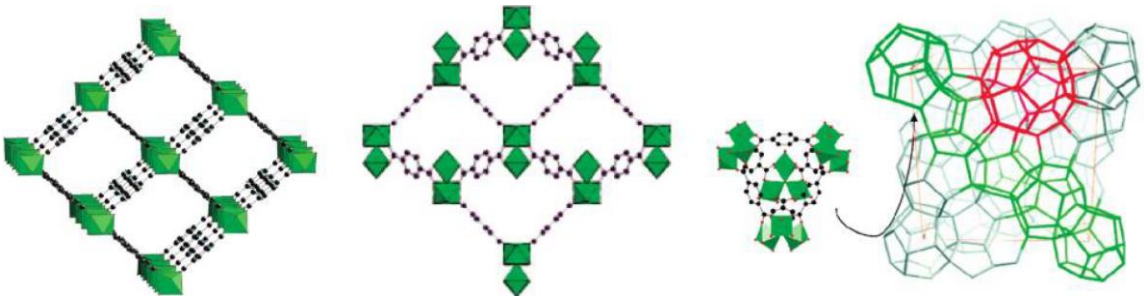

Figure 9 Structures obtained from the reaction of trivalent metals (Cr, Fe, and V) and terephthalic acid: MIL-47 and MIL-53 (left), MIL-88B (center), and MIL-101 (right). (Adapted with permission from Bauer, S.; Serre, C.; Devic, T.; Horcajada, P.; Marrot, J.; Férey, G.; Stock, N. *Inorganic Chemistry* **2008,** *47* (17), 7568-7576. copyright © 2008 American Chemical Society)

Stock *et al.* have studied the formation of MIL-101-NH_2 (MIL stands for Matériaux de l'Institut Lavoisier) using high-throughput methods to investigate the solvent, temperature, and time effects on crystallization.[58] The results have shown the formation of several MOFs in the MIL series under varying reaction conditions. Modulation of the solvothermal reaction conditions using high-throughput synthesis has led to the isolation of MIL53, MIL-88B, and MIL-101 (Figure 9). High-throughput studies have been used to elucidate the effects of various aprotic solvents (Methanol, Acetonitrile, DMF, and water), reaction temperature, molar ratio of starting materials, and molar concentration on the formation of MIL series MOFs.

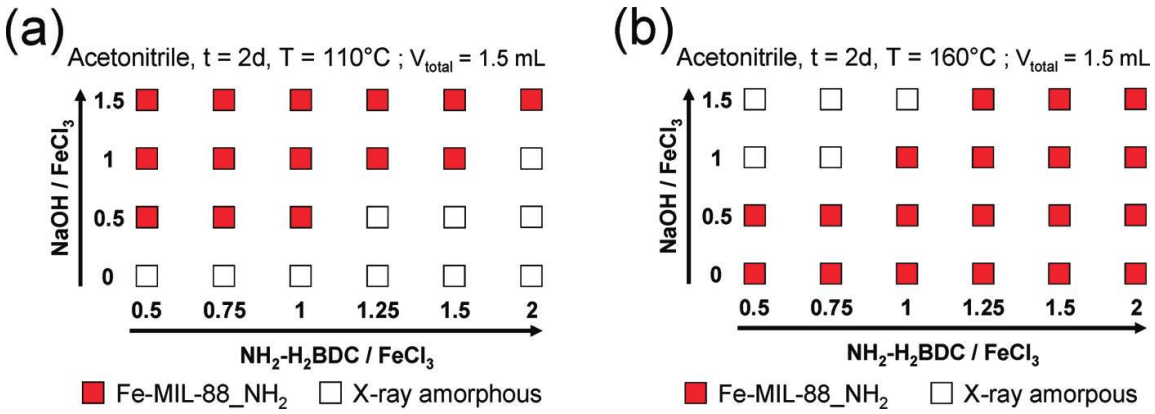

Figure 10 Crystallization diagrams for the high-throughput investigation of the system FeCl 3 /NH 2 - H 2 BDC/NaOH in acetonitrile at 110 ° C (a) and 160 ° C (b) based on powder XRD measurements. (Adapted with permission from Bauer, S.; Serre, C.; Devic, T.; Horcajada, P.; Marrot, J.; Férey, G.; Stock, N. *Inorganic Chemistry* **2008,** *47* (17), 7568-7576. copyright © 2008 American Chemical Society)

The reaction of NH_2-H_2-BDC with $FeCl_3$ under solvothermal conditions using acetonitrile at 100ºC and 160ºC for 2 days was performed varying the molar ratios of starting materials and concentration of NaOH as a modulating reagent with a total volume of 1.5 mL (Figure 10). At lower temperature, increased concentration of sodium hydroxide is necessary to deprotonate the NH_2-H_2-BDC to form the MOFs. Increasing the temperature increases the concentration of aminoterephthalate ions in the solution; the excess sodium hydroxide is not needed to modulate the reaction.

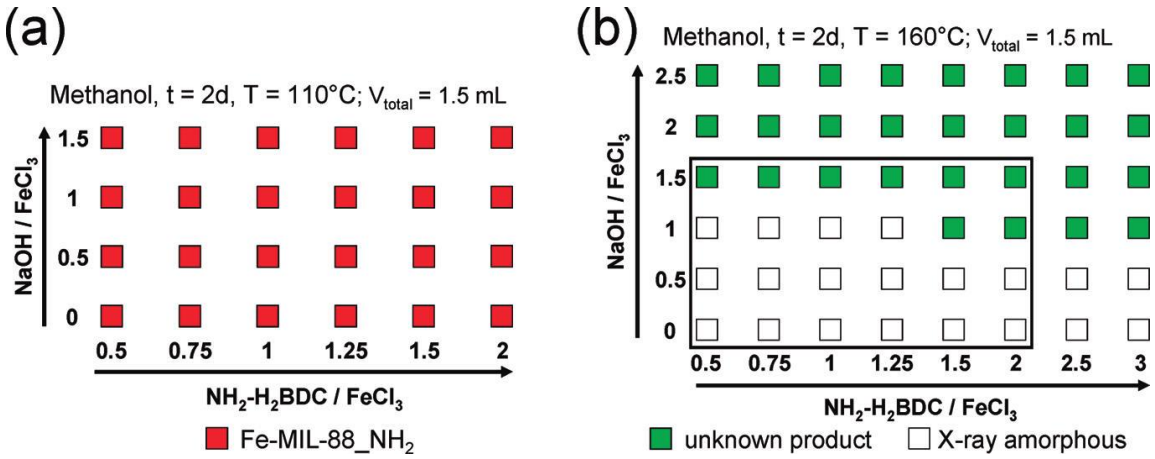

Figure 11 Crystallization diagrams for the high-throughput investigation of the system FeCl 3 /NH 2 - H 2 BDC/NaOH in methanol at 110 ° C (a) and 160 ° C (b) based on powder XRD measurements. The framed area corresponds to the parameter space investigated in the first high-throughput experiment at 160 ° C, and the remaining molar compositions were investigated in an additional experiment. (Adapted with permission from Bauer, S.; Serre, C.; Devic, T.; Horcajada, P.; Marrot, J.; Férey, G.; Stock, N. *Inorganic Chemistry* **2008,** *47* (17), 7568-7576. copyright © 2008 American Chemical Society)

High-throughput experiments were also performed with methanol as the reaction solvent at 110^{o}C and 160^{o}C following the acetonitrile conditions (Figure 11). At 100^{o}C under every experimental condition Fe-MIL-88B-NH_2 was synthesized. It is well established that methanol easily facilitates the deprotonation of the ligand, and thus MIL-88B is easily obtained. At a higher temperature of 160^{o}C, it is hypothesized that there is an increased concentration of methanolate ions that compete with the aminoterephthlate ions limit the formation of Fe-MIL-88-NH_2. The synthetic conditions were expanded to observe more reaction space; however, an unknown product was obtained and failed to be characterized.

Using DMF as the reaction media allows for the isolation of two pure phase MOFs, Fe-MIL-88-NH_2 and Fe-MIL-101-NH_2. High-throughput experiments with DMF were performed at 110^{o}C, 170^{o}C, and 185^{o}C for one day, varying the concentration of metal/ligand ratios and the concentration of NaOH with a total reaction volume of 2mL; scale-up of the MOFs was also performed using the selected reaction conditions (Figure 12). Fe-MIL-101-NH_2 was only observed at 110^{o}C and 170^{o}C when no sodium hydroxide was added to the reaction. At 110^{o}C and 170^{o}C, Fe-MIL-88-NH_2 is observed in every case when sodium hydroxide is added to the system. Ligand/metal ratios do not significantly contribute to MOF formation at lower temperatures. Fe-MIL-101-NH_2 was easily scaled at 110^{o}C whereas Fe-MIL-88-NH_2 forms with increased concentration at a higher temperature. Only Fe-MIL-88-NH_2 is observed at 185^{o}C.

Lastly, water as the reaction solvent resulted in the formation of MIL-53 as the major reaction product; however, many mixed phase materials of MIL-53/MIL-88 and MIL-53/MIL-101 materials were also obtained. Using water as the reaction solvent is the only system in which all three phases (MIL-53, MIL-88, and MIL-101) are observed.[58] Additionally, individual reaction conditions for the pure phase synthesis of each phase is not observed. MIL-88 is only observed in mixed phase products.

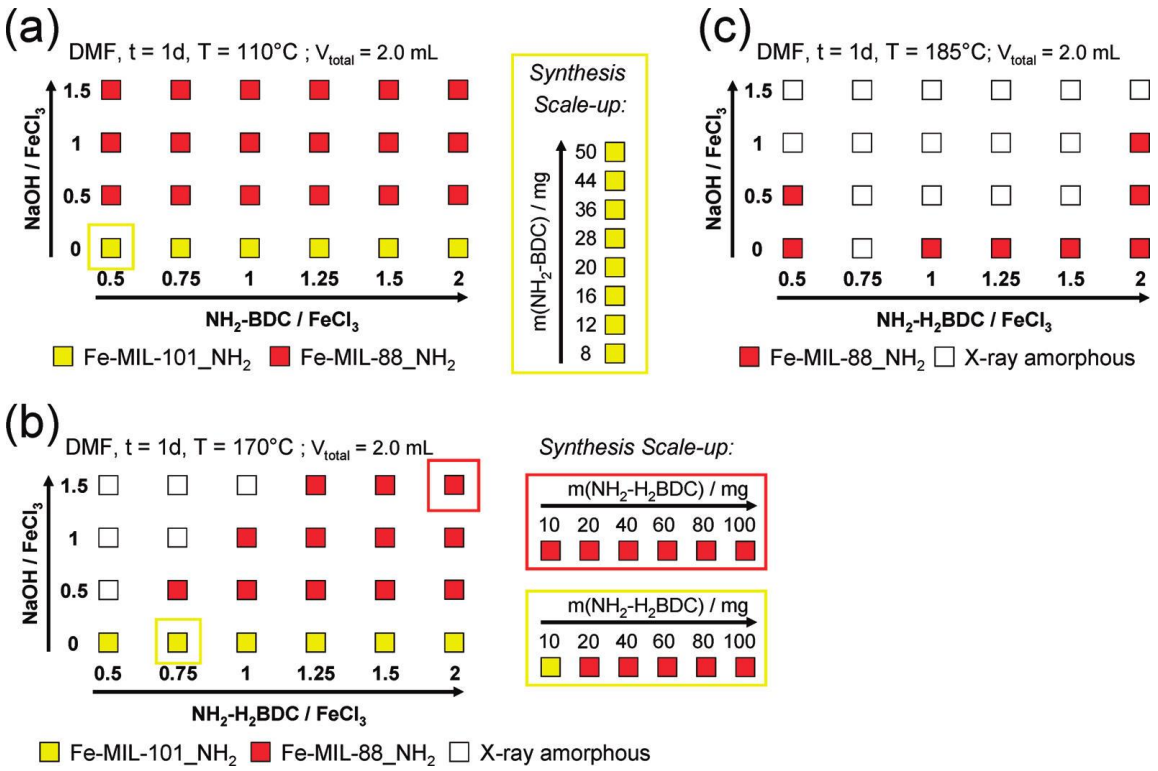

Figure 12 Crystallization diagrams for the high-throughput investigations of the system FeCl 3 /NH 2 - H 2 BDC/NaOH in DMF at 110 ° C (a), 170 ° C (b), and 185 ° C (c) based on powder XRD measurements. The highlighted compositions in the crystallization diagrams refer to the molar ratios realized in the corresponding synthesis scaleup studies. (Adapted with permission from Bauer, S.; Serre, C.; Devic, T.; Horcajada, P.; Marrot, J.; Férey, G.; Stock, N. *Inorganic Chemistry* **2008,** *47* (17), 7568-7576. copyright © 2008 American Chemical Society)

Another study by Bein *et al.* has explored high-throughput method for optimizing the synthetic parameters of HKUST-1 and MOF-5.[9] This study has limited reaction parameters to 1) chemical parameter (metal source, starting material concentrations, and reaction pH) and 2) process parameters (temperature and time).

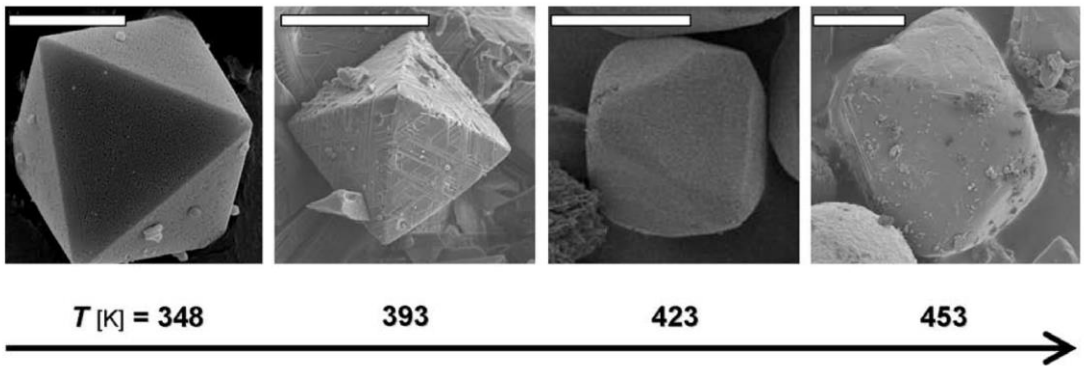

Figure 13 Influence of synthesis temperature on the morphology of HKUST-1. Each scale bar in the different micrographs corresponds to 10 µm. (Adapted with permission from Biemmi, E.; Christian, S.; Stock, N.; Bein, T. *Microporous and Mesoporous Materials* **2009,** *117* (1–2), 111-117.

Temperature and reaction concentration were tested to determine the influence on the crystal formation of HKUST-1. This study has shown that single crystal morphology is diminished with increasing temperature due to the formation of copper (II) oxide (Figure 13). Pure phase HKUST-1 was obtained at 348K following high-throughput temperature screening using previously published synthetic conditions.[12] An additional high-throughput experiment was conducted to explore the effects of concentration on the morphology of HKUST-1; the reaction was conducted at 348K for 24 hours varying starting material concentrations (Figure 14). Tuning of the crystal morphology is possible and octahedral crystals are formed from concentration ratios factor of 0.75-1.3. However, at concentration factor 1.75 the MOF loses the ordered octahedral morphology. This experiment also demonstrates the ability to control crystal size through concentration of starting material.

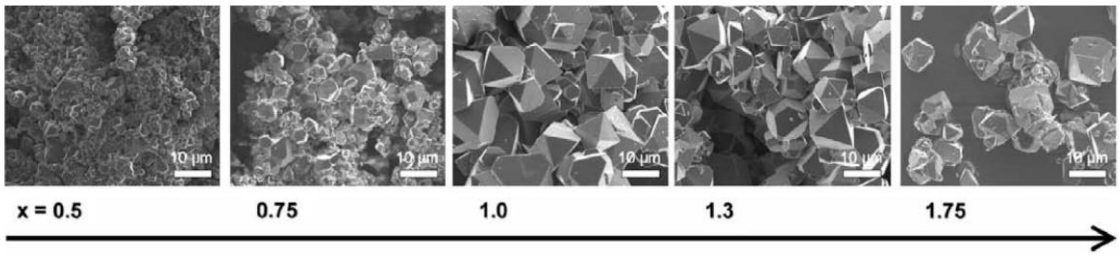

Figure 14 Influence of the concentration on the morphology of HKUST-1. The synthesis was performed under solvothermal conditions at 348 K for 24 h starting from $Cu(NO_3)_2 \cdot 2.5H_2O$. The scale bar of each micrograph corresponds to 10 µm. ''x" denotes the concentration factor with respect to the synthesis recipe.[12] (Adapted with permission from Biemmi, E.; Christian, S.; Stock, N.; Bein, T. *Microporous and Mesoporous Materials* **2009,** *117* (1–2), 111-117. copyright © 2008 Elsevier, Inc.)

Lastly, effects of metal salt, co-solvent media, and pH on the formation of MOF-5 through high-throughput synthesis has been studied.[9] The synthesis of MOF-5 with metal salts, zinc (II) nitrate hexahydrate and zinc (II) oxide, was performed under under mixed solvent conditions at 383K for 48 hours. MOF formation with ZnO was successful and produce MOF-5 with both DMF/mesitylene, DMF/toluene, and DMF/chlorobenzene; however, unreacted ZnO was observed in each condition. Zinc (II) nitrate only yields pure phase MOF-5 in a DMF/mesitylene reaction solution. Therefore, ZnO as the starting metal salt is less sensitive to the effect from the reaction solvent. MOF-5 is highly water sensitive, so the introduction of aqueous solutions result in the inhibition of formation. Thus pH studies were not capable to study MOF-5 formation; however, pH was modulated to identify reactivity trends.

This review of high-throughput methods have shown the strong correlation of MOF synthesis with solvent selection, temperature, and various starting material ratios.

These same design principles have also been applied to other systems, where a factorial approach has led to the synthesis of MOF materials.[59-63] As improvements are made to synthetic protocols and workflows, the rapid development and commercialization of MOFs will increase.

3. TOWARD A METAL-ORGANIC POLYHEDRA BASED MIXED-LINKER METAL-ORGANIC FRAMEWORK THROUGH MIXED LIGAND CO-ASSEMBLY

A mixed ligand co-assembly approach has been explored to develop MOFs with increased structural diversity. Two new MOFs, PCN-351 and PCN-352 have been synthesized exhibiting a triangular Cu_3O secondary building units (SBUs) not readily seen in reported MOFs. In this approach, pyrozolate moieties are used to form the SBU and connected by linear bis(imidazolate) linkers. Topological analysis predicts the potential for the formation of a truncated cubic molecular polyhedral cage that can function as a 12-connected node. PCN-351 forms a condensed structure with 3D channels and limited porosity due to the small imidazolate linker, while PCN-352 exhibits truncated cuboctahedra cages due to flexibility in an elongated linker. While PCN-351 possesses relatively low nitrogen uptake and porosity, the porosity of PCN-352 is improved with a BET surface area of 1453 m^2/g.

3.1 INTRODUCTION

Metal-organic frameworks are an interesting class of materials that have a wide array of application including gas storage, catalysis, drug delivery, and chemical sensing, with many new applications being rapidly discovered.[64-68] Perhaps one of the most important features of the development of these materials is the need to understand the principles of formation. Our group has recently developed new techniques to perform controlled synthesis and functionalization of stable MOFs including kinetically tuned dimensional augmentation synthesis, post-synthetic metathesis and oxidation, and sequential linker installation.[55-57, 69-70] Herein, a mixed-ligand co-assembly process is developed to synthesis novel mixed-linker MOFs.

The inclusion of multiple linkers into the framework structure provide structural diversity and the ability to fine tune material properties through pore functionalization.[71-72] Coupling the use of a mixed-ligand approach with engineering of suprapolyhedral building blocks, new MOF can be rationally designed.[73-74] Perhaps one of the most observed SBU when synthesizing copper (II) MOFs is the dicopper (II) paddlewheel; however, this work will seek to explore the formation of a triangular Cu_3O SBU.[75] This SBU is of particular interest due to the square planar geometry of each copper atom possesses two coordinatively unsaturated metal centers (UMCs). High concentrations of UMCs have been shown to provide favorable host-guest interactions within the framework enhancing gas uptake.[76-78]

Pyrazole was judiciously selected to construct the triangular Cu_3O SBU and it was hypothesized that imidazolate moieties have the appropriate bridging angle to form a

truncated cubic supramolecular building block.[15, 79] The formation of the cubic polyhedral cage is of interest due to the potential to be further utilized as a 12-connected node in the formation of new MOFs.

3.2 EXPERIMENTAL SECTION*

General Information. Copper (II) Nitrate hemipentahydrate, N,N-dimethylacetamide (DMA), Pyrazole, 1,2,3,5-Benzenetetraamine Tetrahydrocloride, 3,3'-diaminobenzidine Formic Acid, Diethyl Ether, and Sodium Hydroxide were all purchased from commercially available sources and were used as received. ^{1}H NMR data were collected on a Mercury 300 MHz NMR spectrometer. FT-IR data were recorded on an IRAffinity-1 instrument. TGA data were obtained on a TGA-50 (SHIMADZU) thermogravimetric analyzer with a heating rate of 3 °C min^{-1} under a N_2 atmosphere.

Instrumentation. ^{1}H NMR data were collected on a Mercury 300 MHz NMR spectrometer. FT-IR data were recorded on an IRAffinity-1 instrument. TGA data were obtained on a TGA-50 (SHIMADZU) thermogravimetric analyzer with a heating rate of 3 °C min^{-1} under a N_2 atmosphere. The powder X-ray diffraction patterns (PXRD) were recorded on a BRUKER D8-Focus Bragg-Brentano X-ray Powder Diffractometer equipped with a Cu sealed tube (λ = 1.54178 Å) at room temperature. Synchrotron-based single crystal diffraction (APS) experiments were performed at the ChemMatCars 15-BM beamline of the Advance Photon Source in Argonne National Laboratory.

* Ligand and MOF synthesis performed with assistance from Madison Haas and Mario Cosio. Structural studies were performed with assistance from Dr. Yusheng Chen and Ying-Pin Chen.

General Synthesis Procedure.[80] A tetraamine starting material was added to a round bottom flask with a magnetic stir bar and formic acid was added to the flask. The flask was fitted with an air-jacked condenser and refluxed at 100°C for 2 h - 4 days. The reaction as then mixed with ice water (equal volume with formic acid) and neutralized with 10% sodium hydroxide. Upon neutralization, a power precipitate was observed and collected by vacuum filtration, rinsed with water and dried in a vacuum oven overnight.

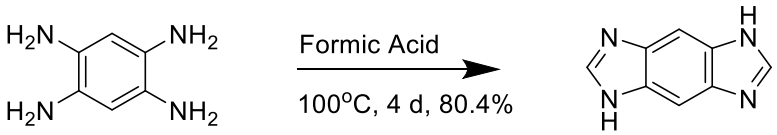

Scheme 1 Synthesis of **H_2BBI**.

Synthesis of Benzo-bis(imidazole) (H_2BBI).[81] 1,2,4,5-Benzenetetraamine tetrahydrochloride (1g, 3.5mmol) was treated with formic acid (50mL) for 4 days at 100°C. The reaction was then mixed with ice water (50ml) and neutralized with 10% sodium hydroxide solution. The precipitate was isolated as a pale brown powder, washed with water, and dried overnight in a vacuum oven. The reaction produced 0.4 g of H2BBI with 80.4% yield. ^{1}H-NMR (300 MHz, DMSO-d_6): 12.1 (4H, bs), 8.18 (2H, bs), 7.70 (2H, bs). Elemental Analysis: $C_8H_6N_4$*$2H_2O$: C 49.2, H 5.64, N 28.7; found: C 50.7, H 3.65, N 27.07.

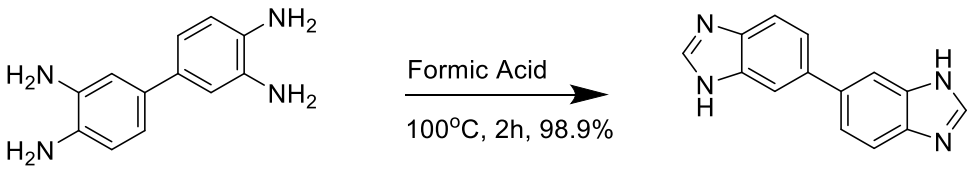

Scheme 2 Synthesis of **H_2DBI**.

Synthesis of 3,3'-Dibenzimidazole (H_2DBI). 3,3'-Diaminobenzidine (10g, 46.7mmol) was treated with formic acid (50mL) for 2 h at 100°C. The reaction was then mixed with ice water (50ml) and neutralized with 10% sodium hydroxide solution. The precipitate was isolated as a cream colored powder, washed with water, and dried overnight in a vacuum oven. The Reaction produced 9.8g of H2BBI with 98.9% yield. ^{1}H-NMR (300 MHz, DMSO-d_6): 8.62 (H, s) (Formic Acid), 8.24 (2H, s), 7.84 (2H, d), 7.65 (2H, d), 7.51 (2H, dd),. ^{13}C NMR (300MHz, DMSO-d_6): δ 164.9 (Formic Acid), 143.0, 138.9, 138.0, 122.1, 116.2, 113.7. Elemental Analysis: $C_{14}H_{11}N_4$*4CHO_2: C 52.05, H 3.61, N 13.50, O 30.84; found: C 48.33, H 3.6, N 12.70.

Synthesis of PCN-351. A mixture of H_2BBI (10 mg, .063mmol) and $Cu(NO_3)_2 \cdot 2.5H_2O$ (50 mg, .21mmol), and Pyrazole (300mg, 4.41mmol) was added to a 1 dram vial containing DMA (3 mL). The solution was then sonicated until all solids were dissolved. The vial was sealed, heated to 100 °C for a 3 day, and black cubic shaped crystals of PCN-352 were collected, washed with DMA, and dried in air to produce.

Elemental analysis (%): calculated for $C_{15}H_{12}Cu_3N_9O$: C, 34.32; H, 2.3; N, 24.01; found: C 37.68, H 4.41, N 21.18.

Synthesis of PCN-352. A mixture of H_2DBI (30 mg, 0.128mmol) and $Cu(NO_3)_2 \cdot 2.5H_2O$ (150 mg, 0.645mmol), and Pyrazole (290mg, 4.25 mmol) was added to a 1 dram vial containing DMA (3 mL). The solution was then sonicated until all solids were dissolved. The vial was sealed, heated to 85 °C for a 4 day, and the blue disk shaped crystals of PCN-351 were collected, washed with DMA, and dried in air to produce. Elemental analysis (%): calculated for $C_{156}H_{120}Cu_{24}N_{72}O_8$: C 40.24, H 2.60, N 12.66 found: C 43.68, H 5.6, N 17.25.

Low-pressure gas adsorption measurements. Gas sorption isotherm measurements were performed on ASAP 2020 and ASAP 2420 Surface Area and Pore Size Analyzers. As-synthesized samples of PCN-351 and PCN-352 were immersed in dry ethyl ether for 24 h and the extract decanted. Fresh dry ethyl ether was subsequently added and the crystals remained in the solvent for an additional 24 h. Each sample was collected by decanting and the procedure repeated once more with dry ethyl ether. After the removal of ethyl ether by decanting, the samples were activated by drying under a dynamic vacuum at room temperature. Before the measurement, PCN-351 and PCN-352 was again further activated using the "degas" function of the surface area analyzer for 2 h at 25 °C. Other activation temperatures were tested, with the reported methods providing the best sorption properties. UHP grade (99.999%) N_2, H_2, and CO_2 were used for all measurements.

X-ray crystallography. Single crystal X-ray diffraction (XRD) measurements were performed on a Bruker SMART APEXii diffractometer equipped with CCD detector,

an Oxford Cryostream low temperature device, and a fine-focus sealed-tube X-ray source (Mo-Kα radiation, λ = 0.71073 Å, graphite monochromated) operating at 50 kV and 30 mA. Raw data collection and refinement were performed using SMART. Absorption corrections were applied using the *SADABS* routine. PCN-351 was solved through direct methods and refined by full-matrix least-squares on F^2 with anisotropic displacement using *SHELXTL*.[82] Non-hydrogen atoms were refined with anisotropic displacement parameters during the final cycles. Hydrogen atoms on carbon were calculated in ideal positions with isotropic displacement parameters set to 1.2 x U_{eq} of the attached atom. Solvent molecules in the structures were highly disordered and attempts to locate and refine solvent peaks were unsuccessful. Therefore, the contribution of solvent electron density was removed by the *SQUEEZE* routine in *PLATON* and refined further using the data generated.[83] The contents of the solvent region are not represented in the unit cell contents in the crystal data. Single crystal X-ray structure determination of PCN-352 were performed at 173(2) K using the Advanced Photon Source on beamline 15ID-B at Argonne National Laboratory. PCN-352 was solved by direct methods and refined by full-matrix least-squares on F^2 using *SHELXTL*.[82] Non-hydrogen atoms were refined with anisotropic displacement parameters during the final cycles. Organic hydrogen atoms were placed in calculated positions with isotropic displacement parameters set to 1.2 × U_{eq} of the attached atom.

Crystal data for PCN-351. $C_{15}H_{12}Cu_3N_9O$, M = 524.96, black cubic, 0.40 × 0.40 × 0.30 mm^3, monoclinic, space group *C*2/*m*, a = 24.72(2) b = 17.839(15) c = 16.557(14) α = 90.00 β = 90.817(11) γ = 90.00, V = 7301(11) Å^3, Z = 8, D_c = 0.955 g/cm^3, F_{000} =

2080, MoK$_\alpha$ radiation, λ = 0.71073 Å, T = 110(2) K, $2\theta_{max}$ = 24.36˚, 23863 reflections collected, 6086 unique (R_{int} = 0.1145). Final *GooF* = 0.856, *R1* = 0.0829, *wR2* = 0.2096, *R* indices based on 6086 reflections with I > 2sigma(I) (refinement on F^2), 271 parameters, 55 restraints. μ = 1.745 mm^{-1}.

Crystal data for PCN-352. $C_{156}H_{120}Cu_{24}N_{72}O_8$, M = 4656.20, Blue sphere, 0.05 × 0.05 × 0.01 mm^3, cubic, space group $P2_13$, a = 34.396(7) b = 34.396(7) c = 34.396(7) α = 90.0 β = 90.0 γ = 90.0, V = 40695(14) Å^3, Z = 4, D_c = 0.760 g/cm^3, F_{000} = 9280, MoK$_\alpha$ radiation, λ = 0.41328 Å, T = 110(2) K, $2\theta_{max}$ = 9.97˚, 257967 reflections collected, 8371 unique (R_{int} = 0.1622). Final *GooF* = 0.971, *R1* = 0.1093, *wR2* = 0.2159, *R* indices based on 8371 reflections with I > 2sigma(I) (refinement on F^2), 435 parameters, 194 restraints. μ = 0.661 mm^{-1}.

3.3 RESULTS AND DISCUSSION

Syntheses and structures. H_2BBI and H_2BDI were synthesized through a one-step condensation reaction of tetraamine with formic acid. H_2BBI was selected as a short rigid linker, while H_2BDI is longer in length and also possesses rotational freedom. PCN-351 was synthesized in a one-pot synthesis by dissolving all starting in DMA and adding excess pyrazole as a modulation reagent. Large excess of pyrazole was necessary to form the MOF in order to adjust the pH of the reaction solution to optimal conditions for solvothermal synthesis. Single crystals of PCN-351 were obtained with black cubic shape and was characterized by single crystal x-ray diffraction. PCN-351 (Figure 15) crystalizes in the monoclinic, C2/*m* space group with united cell edges a = 24.72(2) b = 17.839(15) c = 16.557(14) and angles α = 90.00 β = 90.817(11) γ = 90.00.

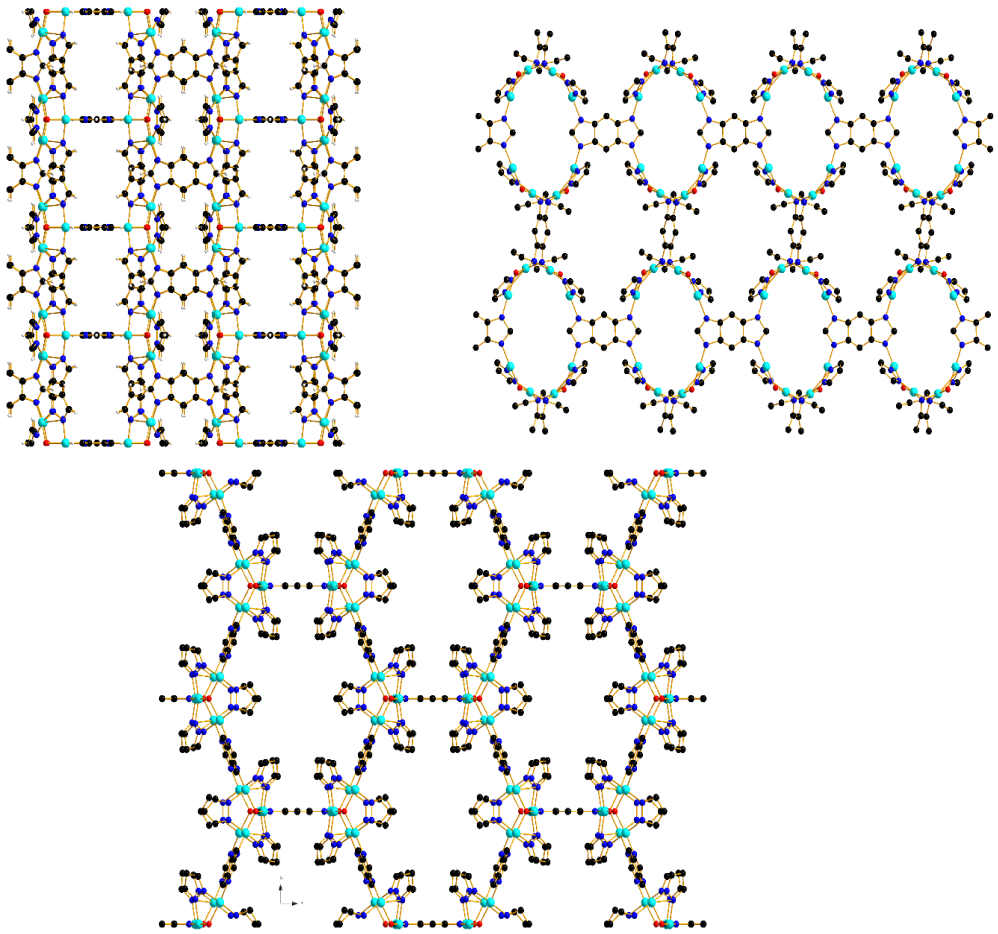

Figure 15 Structure of PCN-351, (top left) view down a axis, (top right) view down b axis, (bottom) view down c axis. Cu = turquoise; C = black; N= dark blue O = red; H and coordinated solvent excluded, for clarity.

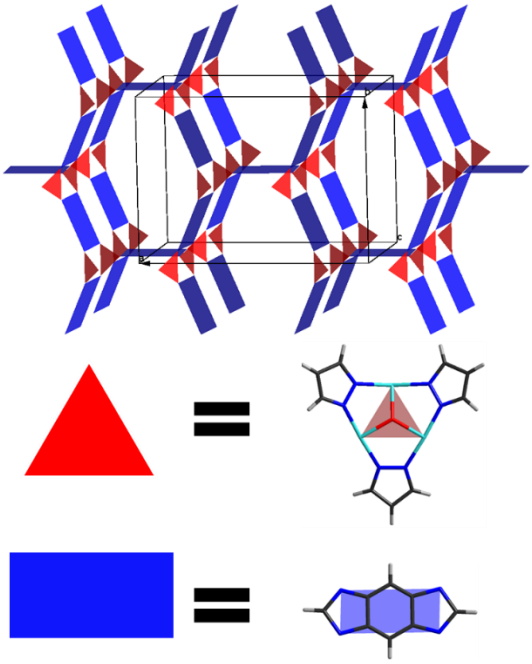

Figure 16 Assembly of PCN-351, connectivity of planar H_2BBI linker with trigonal Pz_3Cu_3O SBUs. Red triangle represents the Copper (II) SBU. Blue rectangle represents H_2BBI linker. View along c axis.

The rigidity of the H_2BBI linker only allows for connectivity in two planes confining the structure to 3D-channels (Figure 16). H_2DBI was selected due the single bond between the benzimidazole groups allowing for extra degrees of rotational freedom. Additionally, the elongated linker also allows for more flexibility than the rigid planar H_2BBI. PCN-352 was synthesized under solvothermal conditions with excess pyrazole as a modulation reagent. PCN-352 was obtained as blue spherical crystals and were characterized using synchrotron radiation at Argonne National Laboratory, BM-17. PCN-

352 (Figure 17) crystalizes in the cubic space group $P2_13$, a = 34.396(7) b = 34.396(7) c = 34.396(7) α = 90.0 β = 90.0 γ = 90.0.

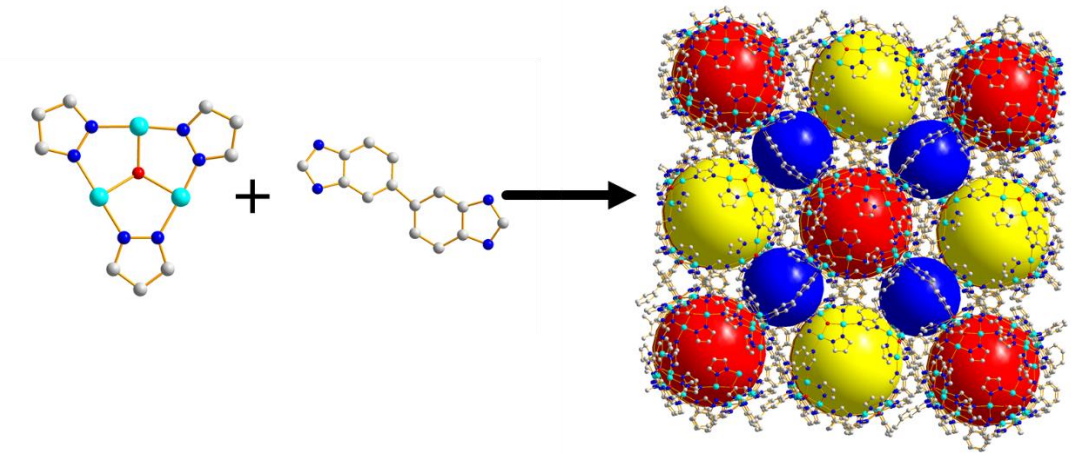

Figure 17 Structure of PCN-352, a triangular Pz_3Cu_3O cluster is connected by the H_2BDI to form a MOF composed of molecular cages. Spheres occupy different size cages present in the structure.

PCN-352 is composed of three molecular cages, as seen in Figure 18, the combination of the SBU and the connecting imidazole linker yields a truncated cubic cage. These cubic cages are then connected through the H_2BDI linker forming tetrahedral cages. Lastly, the cubic cages are located on the vertices of an octahedral cage. Due to the chirality of the imidazolate linker, a slight twist is observed in the symmetry dependent octahedral and tetrahedral cages. The cages also vary in pores size based on geometry

with the cubic cage having a pore size of 15Å, tetrahedral cage of 9Å, and octahedral cage of 16Å.

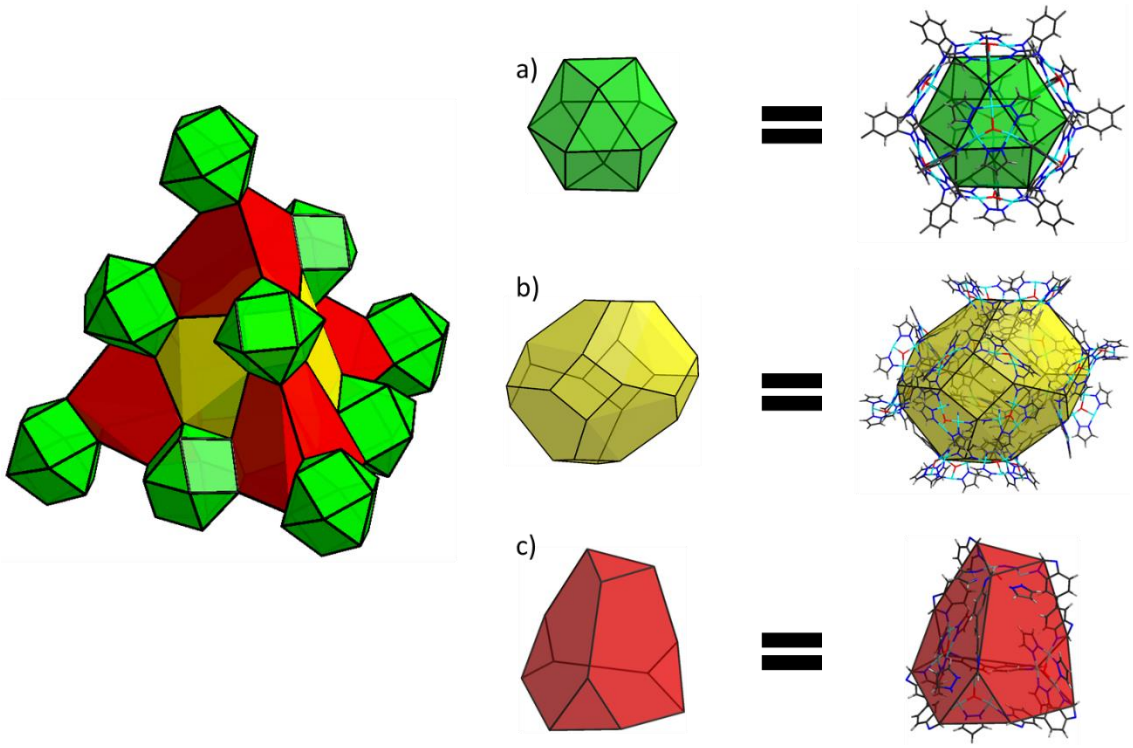

Figure 18 Structural representation of PCN-352 and packing of molecular cages. a) cuboctahedral cage, b) truncated octahedral cage, and c) truncated tetrahedral cage.

Thermogravimetric analysis (Figure 19) demonstrates the poor thermal stability of PCN-351, while PCN-352 is stable to approximately 400^{o}C. PCN-351 shows a gradual weight loss from (25-250^{o}C) representing the loss of coordinated solvent molecules and then the gradual decomposition of the framework from (250-500^{o}C). PCN-352 exhibits much greater chemical stability with no initial weight loss from 25-250^{o}C, followed by

removal of the solvent (250-400°C) and, the gradual degradation of the MOF (above 400°C).

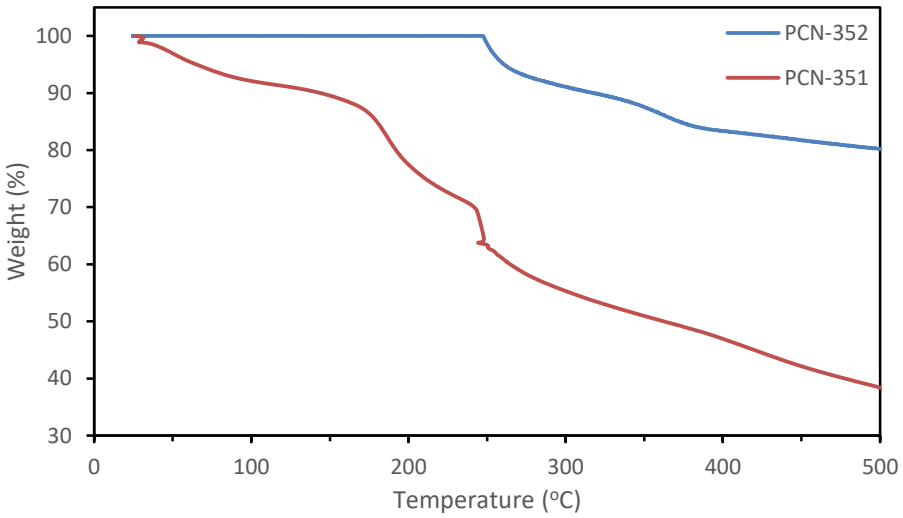

Figure 19 Thermogravimetric analysis of PCN-351 and PCN -352.

Gas Studies. Activation of these MOFs are challenging due to coordinated solvents on the open metal sites during synthesis. In order to fully activate the samples, an extensive solvent exchange process with diethyl ether is necessary. Failure to remove the strongly coordinating DMA solvents cause framework collapse upon degassing on the porosity analyzer. Additionally, in the case of PCN-351, due to poor thermal stability framework collapse is observed under elevated degassing temperatures. Nitrogen uptake at 77K demonstrates typical type I isotherms (microporous materials) with PCN-351

exhibiting low uptake of approximately 50 cm^3/g (1 bar) and BET surface area of $417m^2/g$ and PCN-352 possessing high nitrogen uptake of approximately 400 cm^3/g (1 bar) and BET surface area of $1453m^2/g$.

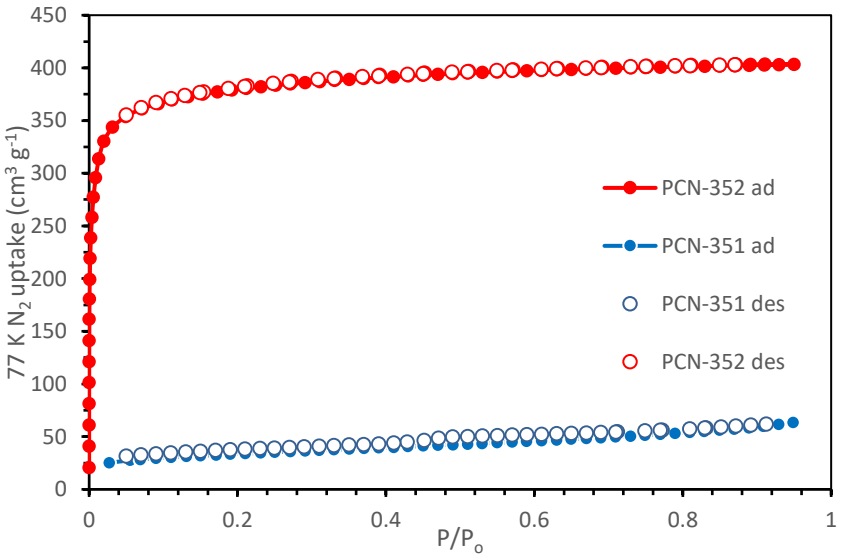

Figure 20 Nitrogen isotherms of PCN-351 and PCN-352 measured at 77K.

Due to the low porosity of PCN-351, further gas studies were not performed on the material. CO_2 and H_2 uptake of PCN-352 were further studied. Moderate H_2 uptake was observed at 273K; however, the MOF demonstrated low uptake of CO_2.

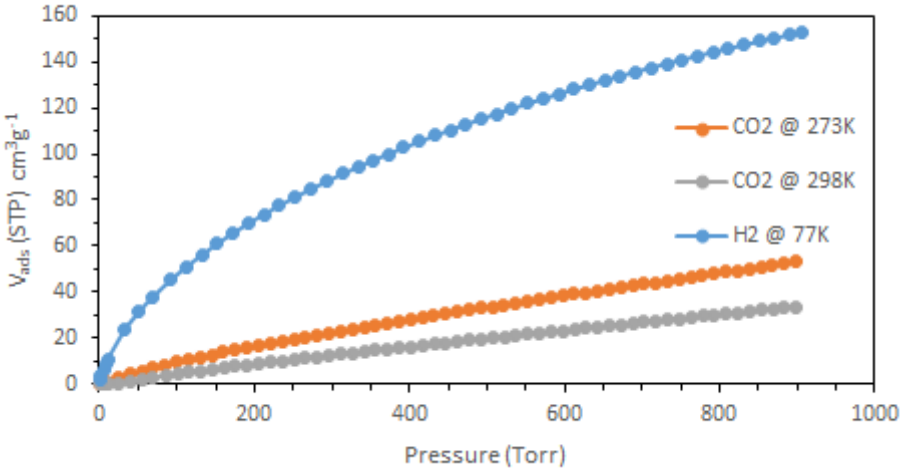

Figure 21 CO_2 and H_2 uptake isotherms of PCN-352 at varying temperature.

3.4 CONCLUSIONS

In conclusion, two new mixed-linker MOFs were formed with a $Pz_3Cu_3O_3$ triangular SBU connected through linear imidazolate linkers. These MOFs were formed in a one-pot solvothermal synthesis with excess pyrazole as a modulating reagent. This mixed-ligand co-assembly is an interesting approach to explore the development of new MOFs with structural diversity and enhanced tuneability. PCN-351 poessess 3-D channels and BET surface area of 417m^2/g, while PCN-352 is composed of three types of molecular cages and exhibits enhanced BET surface area of 1453m^2/g. While chemical stability does is not improved over traditional MOFs, PCN-352 exhibits thermal stability to 400ºC. Moderate gas uptake for H_2 and CO_2 are observed for PCN-352.

4. HIGH-THROUGHPUT SYNTHESIS OF MIXED-LINKER METAL-ORGANIC FRAMEWORKS THROUGH LIGAND CO-ASSEMBLY

High-throughput techniques are a powerful tools to investigate the synthesis of new MOF materials due to the nature of their synthesis. The synthesis of MOFs are optimized through one-pot hydrothermal or solvothermal reactions with small variations in reaction condition influencing their formation. Due to the wide variety of possible reaction conditions, combinatorial methods are beneficial for elucidating the contribution of reaction components on the formation of MOFs. For characterization purposes, x-ray quality single crystals are needed to facilitate structural determination; however, crystal growth is reliant on many factors including solvent, starting material ratios, pH, reaction temperature, modulating reagents, and reaction time. For implementation of a material, a powder might instead be desired requiring entirely different reaction conditions. In this study, high-throughput synthetic techniques have been utilized to synthesis optimize the synthesis of PCN-352 and to develop two new MOF, PCN-353 and PCN-354. These new MOFs were synthesized using a mixed-ligand co-assembly of a given linker and pyrazole.

4.1 INTRODUCTION

Recent advances in robotic and automated synthesis has pushed researchers to study new methods for the rapid synthesis and characterization of materials. A combinatorial approach has recently be utilized as a high-throughput method for the synthesis of MOFs.[84-85] The synthesis of MOFs is a challenge process due to the many variables that contribute to the formation of new materials including: metal-ligand ratios, solvent, temperature, modulation reagent, and pH.[7, 86]

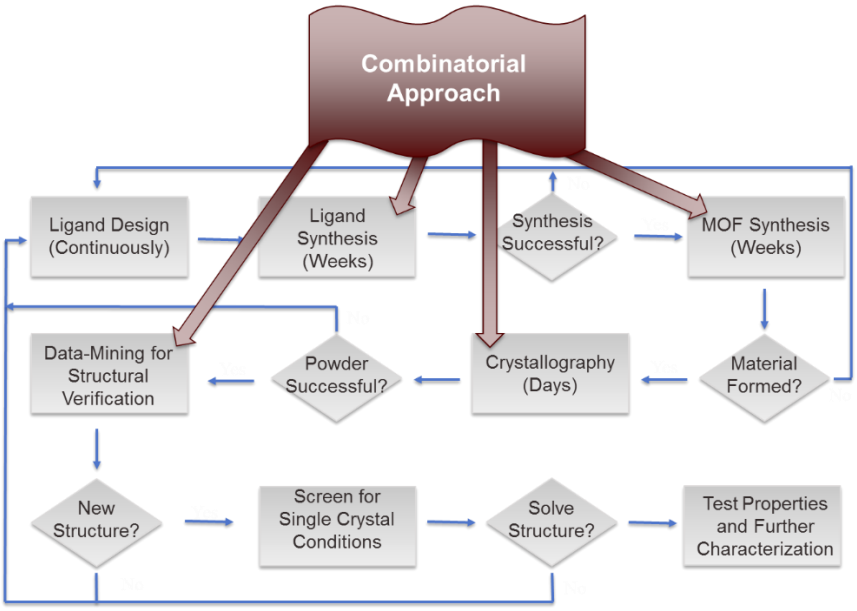

Figure 22 Proposed combinatorial approach to improve efficiency of synthesis and characterization of new MOFs.

The synthesis and characterization of new MOFs is a time consuming process including: continual design and synthesis of new ligands (weeks), solvothermal MOF synthesis (weeks), and structure determination through powder or single crystal X-ray diffraction (days-weeks). Thus, an ideal combinatorial approach (Figure 22) could drastically increase the development of new materials through combining ligand and MOF synthesis using a high-throughput synthetic platform, and coupling automated PXRD characterization with data-mining to enhance structural determination. Perhaps the biggest challenge for these materials is characterization of a large number of samples generated through the high-throughput method (Figure 23).

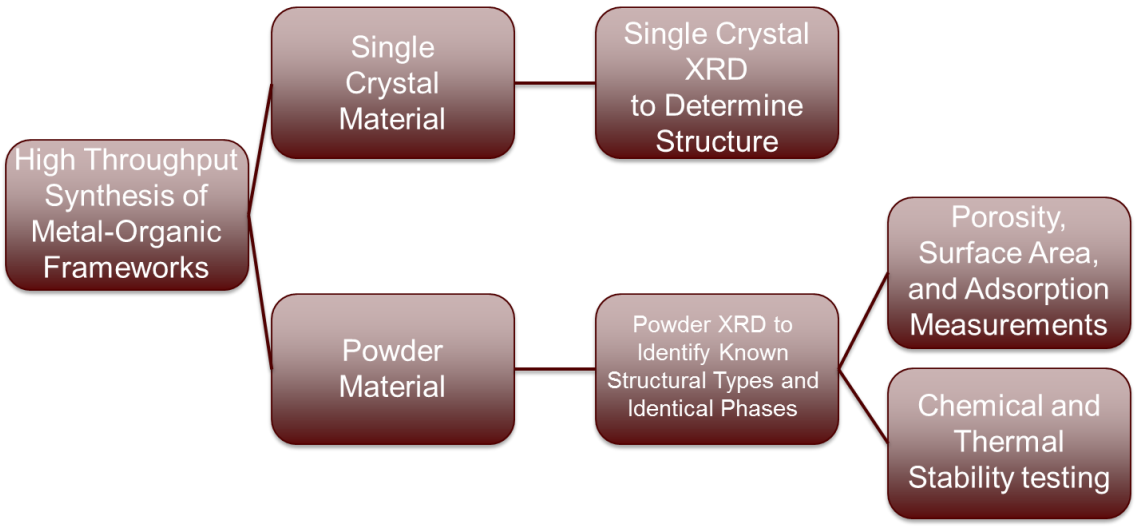

Figure 23 Characterization of MOFs through single crystal and powder X-ray diffraction.

In this study, we have chosen to use reticular synthesis to investigate the formation of new MOFs with structural topology of the previous reported PCN-352. Reticular chemistry is a powerful concept for exploring new MOFs. In this approach, ligands and SBUs are selected such that known topologies are formed upon synthesis based on their connectivity and geometric properties. Linear elongated bis(imidazolate) linkers are selected to enhance porosity of PCN-352 type MOFs by increasing the pore size. The Pz_3Cu_3O SBUs is again used to provide the 12-connected supramolecular node. Based on reticular synthesis, we would expect to observe enlargement of pore size of the truncated octahedral and truncated tetrahedral cages as the linker is elongated.

In this project, a Chemspeed SLT-II synthetic platform was used for high-throughput synthesis. The platform was equipped with a volumetric transfer unit consisting of one milliliter syringes and fluorosilane coated needles (acid-base resistance), and a 50 vial reaction plate (Figure 24). Reaction conditions of PCN-352 were observed at 85^{o}C, 100^{o}C, and 120^{o}C and with varying concentrations of pyrazole as a modulation reagent. The conditions that provide large yield and single crystallinity were selected for synthesis with pyridine as a modulation reagent. The synthetic procedure was then completed to observe the formation of PCN-353 and PCN-354.

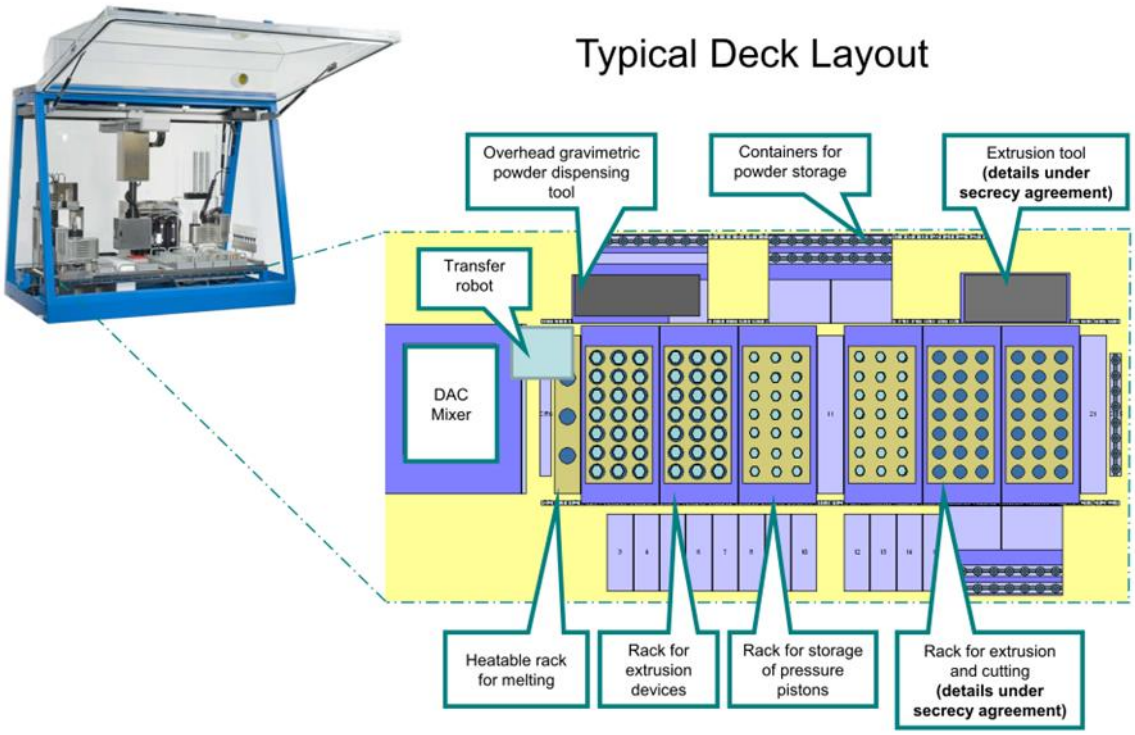

Figure 24 Chemspeed® SLT-Swing high-throughput synthetic platform. The platform is fully configurable with a variety of vial and rack options. The TAMU instrument is equipped with a solid depensing unit, volumetric syringes and coated needles, 4 configured rack for vials (1ml-50ml), vial capper, and vortexing heated plates.

4.2 EXPERIMENTAL SECTION*

General Information. Copper (II) Nitrate hemipentahydrate, N,N-dimethylacetamide, Pyrazole, 1,2,3,5-Benzenetetraamine Tetrahydrocloride, 3,3'-diaminobenzidine Formic Acid, Sodium Hydroxide, Pyridine, p-Phenylenediamine, 3,3',5,5'-tetramethylbenzidine and N,N'-dimethylformamide, were all purchased from

* Ligand and MOF synthesis performed with assistance from Madison Haas, Mitchel Johnson, and Mario Cosio. Structural studies were performed with the assistance of Ying-Pin Chen, Dr. Yusheng Chen, and Dr. Andrey Yakovenko.

commercially available sources and were used as received. ^{1}H NMR data were collected on a Mercury 300 MHz NMR spectrometer. FT-IR data were recorded on an IRAffinity-1 instrument. TGA data were obtained on a TGA-50 (SHIMADZU) thermogravimetric analyzer with a heating rate of 3 °C min^{-1} under a N_2 atmosphere.

Instrumentation. ^{1}H NMR data were collected on a Mercury 300 MHz NMR spectrometer. FT-IR data were recorded on an IRAffinity-1 instrument. TGA data were obtained on a TGA-50 (SHIMADZU) thermogravimetric analyzer with a heating rate of 3 °C min^{-1} under a N_2 atmosphere. Synchrotron-based single crystal diffraction (APS) experiments were performed at the ChemMatCars 15-BM beamline of the Advance Photon Source in Argonne National Laboratory. Synchrotron-based powder diffraction (APS) experiments were performed at the 17-BM beamline of the Advance Photon Source in Argonne National Laboratory.

General Synthesis Procedure H_2PBI and H_2BPBI.[87] A linear diamine starting material was added to a round bottom flask with a magnetic stir bar and DMF was added to the flask. The flask was fitted with an air-jacked condenser and heated at 100^{o}C for overnight. The reaction was then mixed with distilled water and the resulting precipitate was collected by vacuum filtration, rinsed with water and dried in a vacuum oven overnight.

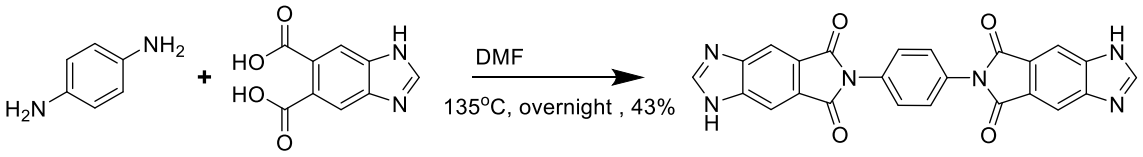

Scheme 3 Synthesis of **H_2PBI**.

Synthesis of 6,6'-(1,4-phenylene)bis(indeno[5,6-d]imidazole-5,7(1H,6H)-dione) (H_2PBI). p-Phenylenediamine (1.5g, 13.9mmol) and 5,6-dicarboxylic acid benzimidazole (5.73g, 27.8mmol) was added to a round bottom flask with DMF (100mL). The flask was fitted with an air-jacketed condenser and heated at 135°C overnight. The reaction was then mixed with distilled water (100mL). The resulting precipitate was isolated as a cream colored powder by vacuum filtration, washed with water, and dried overnight in a vacuum oven. The reaction produced 2.58g of H2PBI with 43.0% yield. ^{1}H-NMR (300 MHz, DMSO-d_6): 13.3 (2H, bs, N-H), 8.61 (2H, s), 8.22 (2H, s), 8.13 (2H, s), 7.64 (4H, s). Elemental Analysis: $C_{26}H_{14}N_4O_4$: C 64.3, H 2.70, N 18.7, O 14.3; found: C 63.4, H 2.84, N 18.6.

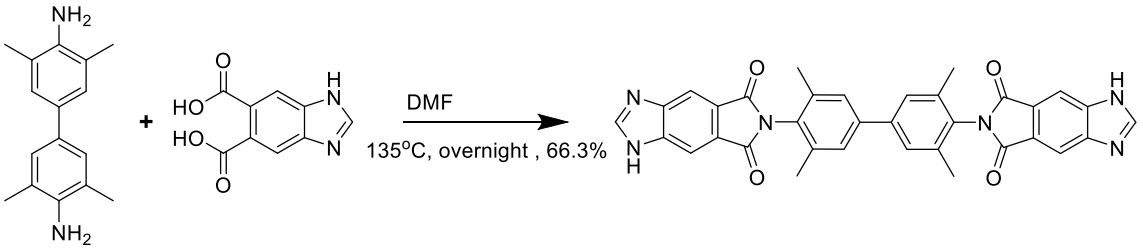

Scheme 4 Synthesis of **H_2BPBI**.

Synthesis of 6,6'-(3,3',5,5'-tetramethyl-[1,1'-bephenyl]-4,4'-diyl)bis(imidazo[4,5-f]isoindole-5,7(1H,6H)-dione (H_2BPBI). 3,3',5,5'-tetramethylbenzidine (3.00g, 12.4mmol) and 5,6-dicarboxylic acid benzimidazole (5.14g, 24.8mmol) and DMF (150mL) was added to a round bottom flask fitted with an air-jacketed condenser and heated at 135^{o}C overnight. The reaction was then treated with water (150mL). The resulting precipitate was isolated by vacuum filtration, washed with water, and dried overnight in a vacuum oven. The reaction produced 4.77g of H2PBI with 66.3% yield. ^{1}H-NMR (300 MHz, DMSO-d_6): 13.3 (4H, bs), 8.60 (2H, bs), 8.16 (2H, bs), 7.6 (2H, s), 2.15 (12H). Elemental Analysis: $C_{34}H_{24}N_6O_4$: C 70.34, H 4.17, N 14.47, O 11.02; found: C 66.88, H 4.96, N 13.45.

Synthesis of 3,3'-Dibenzimidazole (H_2DBI). 3,3'-Diaminobenzidine (10g, 46.7mmol) was treated with formic acid (50mL) for 2 h at 100^{o}C. The reaction was then mixed with ice water (50ml) and neutralized with 10% sodium hydroxide solution. The precipitate was isolated as a cream colored powder, washed with water, and dried overnight in a vacuum oven. The Reaction produced 9.8g of H2BBI with 98.9% yield. ^{1}H-NMR (300 MHz, DMSO-d_6): 8.62 (H, s) (Formic Acid), 8.24 (2H, s), 7.84 (2H, d), 7.65 (2H, dd), 7.51 (2H, dd),. ^{13}C NMR (300MHz, DMSO-d_6): δ 164.9 (Formic Acid), 143.0, 138.9, 138.0, 122.1, 116.2, 113.7. Elemental Analysis: $C_{14}H_{11}N_4$*4CHO_2: C 52.05, H 3.61, N 13.50, O 30.84; found: C 48.33, H 3.6, N 12.70.

High-throughput Synthesis. A Chemspeed SLT-II Swing synthetic platform was used for MOF synthesis. Chemspeed Autosuite was used for all programming and for workflow. Volumetric transfer was performed using Chemspeed syringes with accuracy

± 10μL. All starting materials were dissolved into stock solutions with fixed concentrations in DMA. The solutions were then mixed based on reaction parameters into borosilicate vials and heated for 2-4 days (Table 1). Multiple experiments were performed with optimal runs reported.

Synthesis of PCN-353. A mixture of H_2PBI (4 mg, .009mmol) and $Cu(NO_3)_2 \cdot 2.5H_2O$ (14 mg, .06mmol), and Pyrazole (24.5mg, .36mmol) each in DMA were volumetric transferred, using a robotic platform, to a 1 dram vial and the solution was brought to 3mL. The vial was sealed, heated to 100 °C for a 3 day, and blue cubic shaped crystals of PCN-353 were collected, washed with DMA. Elemental analysis (%):found: C 48.25, H 6.47, N 11.07.

Synthesis of PCN-354. A mixture of H_2BPBI (2.75 mg, .0048mmol) and $Cu(NO_3)_2 \cdot 2.5H_2O$ (14 mg, .06mmol), and Pyrazole (24.5mg, .36mmol) were each added to a 1 dram vial for a total reaction volume of 3mL DMA using a robotic platform. The vial was sealed, heated to 100 °C for 3 days, and black octahedral shaped crystals of PCN-354 were collected, washed with DMA. Elemental analysis (%): found: C 48.25, H 6.63, N 16.08.

Table 1 Sample high-throughput synthesis conditions of PCN-352.

	Metal			Linker			Pyrazole			Solvent
ID	eq	mmol	mL	eq	mmol	mL	eq	mmol	mL	mL
1	1	0.06	1	0.1	0.006	0.4	2	0.12	0.2	1.4
2	1	0.06	1	0.15	0.009	0.6	2	0.12	0.2	1.2
3	1	0.06	1	0.2	0.012	0.8	2	0.12	0.2	1
4	1	0.06	1	0.25	0.015	1	2	0.12	0.2	0.8
5	1	0.06	1	0.1	0.006	0.4	4	0.24	0.4	1.2
6	1	0.06	1	0.15	0.009	0.6	4	0.24	0.4	1
7	1	0.06	1	0.2	0.012	0.8	4	0.24	0.4	0.8
8	1	0.06	1	0.25	0.015	1	4	0.24	0.4	0.6
9	1	0.06	1	0.1	0.006	0.4	6	0.36	0.6	1
10	1	0.06	1	0.15	0.009	0.6	6	0.36	0.6	0.8
11	1	0.06	1	0.2	0.012	0.8	6	0.36	0.6	0.6
12	1	0.06	1	0.25	0.015	1	6	0.36	0.6	0.4
13	1	0.06	1	0.1	0.006	0.4	8	0.48	0.8	0.8
14	1	0.06	1	0.15	0.009	0.6	8	0.48	0.8	0.6
15	1	0.06	1	0.2	0.012	0.8	8	0.48	0.8	0.4
16	1	0.06	1	0.25	0.015	1	8	0.48	0.8	0.2
17	1	0.06	1	0.1	0.006	0.4	10	0.6	1	0.6
18	1	0.06	1	0.15	0.009	0.6	10	0.6	1	0.4
19	1	0.06	1	0.2	0.012	0.8	10	0.6	1	0.2
20	1	0.06	1	0.25	0.015	1	10	0.6	1	0

Low-pressure gas adsorption measurements. Gas sorption isotherm measurements were performed on ASAP 2020 and ASAP 2420 Surface Area and Pore Size Analyzers. Due to the extension of the linker, framework collapse is likely under normal degassing activation on the analyzer. As such, these MOFs were activated by solvent exchange followed by supercritical CO_2 drying. As-synthesized samples of PCN-353 and PCN-354 were immersed in dry DMA for 24 h and the supernatant decanted.

Fresh dry DMA was subsequently added and the crystals remained in the solvent for an additional 24 h. Each sample was collected by decanting and the procedure repeated once more with dry DMA. PCN-353 and PCN-354 were then removed from the solvent and activated using a Tousimis Samdri PVT-3D supercritical point dryer.[88] N_2 isotherms were then measured at 77K to determine porosity and N_2 uptake.

X-ray crystallography. Single crystal X-ray diffraction (XRD) measurements were performed on a Bruker SMART APEXii diffractometer equipped with CCD detector, an Oxford Cryostream low temperature device, and a fine-focus sealed-tube X-ray source (Mo-Kα radiation, λ = 0.71073 Å, graphite monochromated) operating at 50 kV and 30 mA. Raw data collection and refinement were performed using SMART. The powder X-ray diffraction patterns (PXRD) were recorded on a BRUKER D8-Focus Bragg-Brentano X-ray Powder Diffractometer equipped with a Cu sealed tube (λ = 1.54178 Å) at room temperature. Synchrotron-based powder diffraction (APS) experiments were performed at the 17-BM beamline of the Advance Photon Source in Argonne National Laboratory. The simulated PXRD spectra were obtained by the diffraction-crystal module of the Mercury program based on the single-crystal data. The program is available free of charge via internet at http:/www.iucr.org.

Crystal data for PCN-353. Blue cubes, cubic, space group $Pa\ \bar{3}$, a = 47.9128 b = 47.9128 c = 47.9128 α = 90.00 β = 90.00 γ = 90.00. R_{exp}= 0.24%, R_{wp}= 2.66%, R_p=1.48%, G_{oof}= 11.31

Crystal data for PCN-354. Black octahedral, cubic, space group $Pa\ \bar{3}$, a = 52.497(15) b = 52.497(15) c = 52.497(15) α = 90.00 β = 90.00 γ = 90.00.

4.3 RESULTS AND DISCUSSION

Syntheses. In Section 3, PCN-352 was synthesized using a mixed ligand approach; however, large excesses of pyrazole was needed and the morphology was not well defined. Using a high-throughput synthetic platform, the synthesis of PCN-351 was investigated to determine the effect of ligand concentration, temperature, and modulating reagent on the formation of the MOF. First, PCN-351 was investigated at 85°C, 100°C, and 120°C for 3-4 days. The ratio of ligand to metal was modulated from 0.1 molar equivalents to 0.25 molar equivalents. Pyrazole was also used as a modulating reagent varying concentrations from 0 molar equivalents to 8 molar equivalents with respect to metal concentration.

The results of the robotic synthesis of PCN-352 have been graphically summarized in Figure 25 and Figure 26. In the case of each temperature, an unidentifiable green amorphous power was observed at low or zero equivalents of pyrazole, which is expected due to the absence of pyrazole which forms the Pz_3Cu_3O SBU. The experiments with zero molar equivalence were screened due to the possibility of forming a MOF solely with the bis(imidazolate) linkers. It is also important to note that no reaction was observed for PCN-352 at 85°C for 3 day, the reaction needed an extra day of time for the formation of material. For reactions at 85°C and 100°C, no reaction was observed at low concentration of ligand (0.1 eq and 0.15eq) and low concentration of pyrazole (2 eq). Also, higher concentration of pyrazole (6 eq and 8 eq) and low concentration of ligand resulted in the formation of a small molecule $Cu(pyrazole)_4$ complex. At 85°C for 4 days, PCN-352 was only observed at ligand concentration of 0.25 molar equivalents. Additionally, only small amounts and crystal size was observed at 4 equivalents pyrazole.

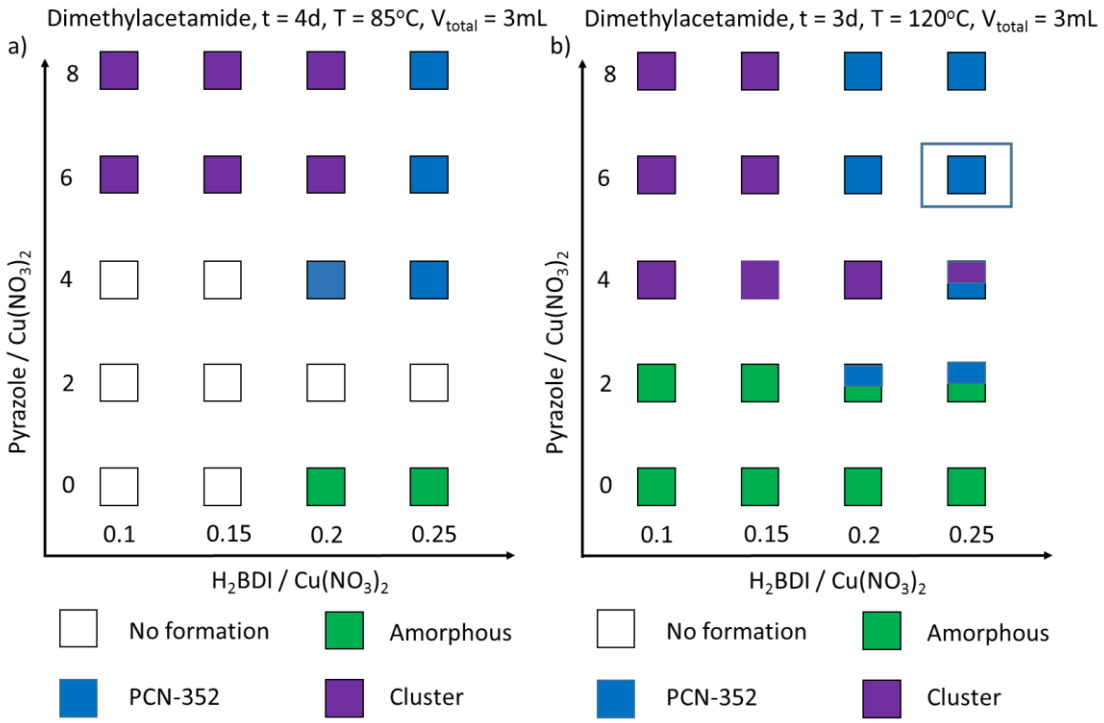

Figure 25 Crystallization diagrams for the high-throughput investigation of the system Pyrazole /$Cu(NO_3)_2$ and $H_2BDI/Cu(NO_3)_2$ in DMA at 85 ° C for 4 days (a) and 120 ° C for 3 days (b) based on powder XRD measurements.

At the elevated temperature of 120°C for 3 days, a product was observed at every reaction condition. For low concentration of pyrazole (0 eq and 2 eq), amorphous material was observed at every concentration of H_2BDI. However, in at 0.2 and 0.25 molar equivalents of H_2BDI, small amounts of PCN-352 were observed. The formation of PCN-352 is segmented into the top right quadrant of the crystallization diagram signify the need for excess pyrazole for MOF formation as observed in Section 3. At low concentration of

linker, the excess pyrazole tends to favor the formation of the copper cluster. At both 85°C and 120°C the transition point seems to be 4 equivalence of pyrazole.

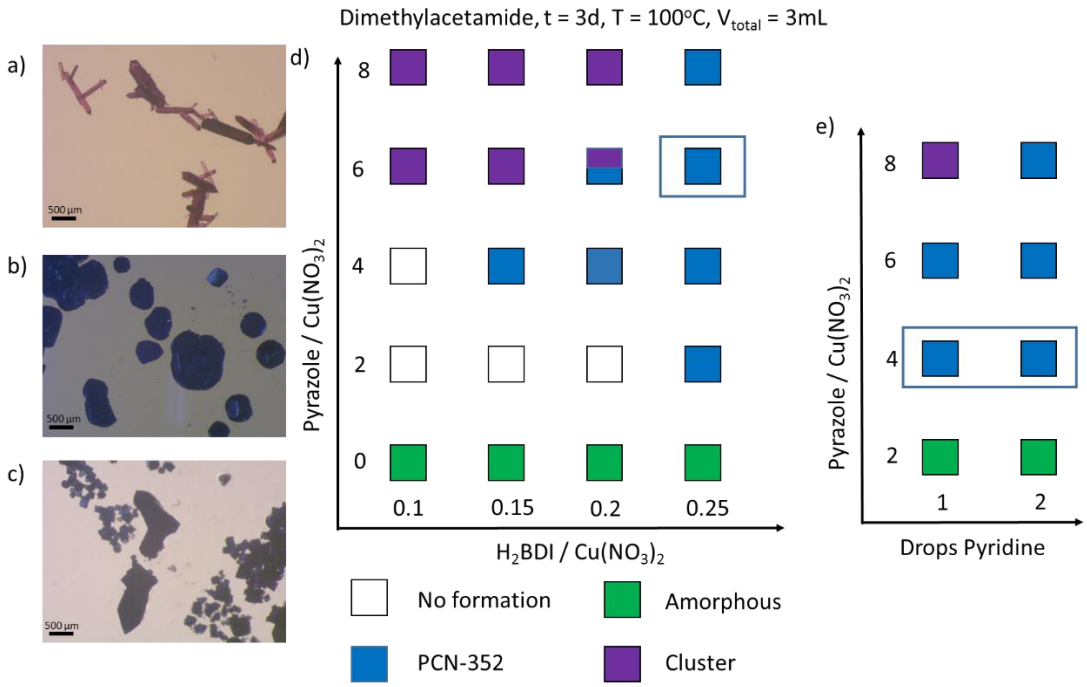

Figure 26 Single crystal material and crystallization diagrams for the high-throughput investigation of the system Pyrazole /$Cu(NO_3)_2$ and $H_2BDI/Cu(NO_3)_2$ in DMA at 100 ° C for 3 days based on powder XRD measurements. a) small molecule copper pyrazolate cluster, b) blue spherical crystals of PCN-352 obtained under excess pyrazole conditions, c) cubic blue crystals of PCN-352 obtained with 2 drops pyridine, d) crystallization diagram for reaction with excess pyrazole, and e) crystallization diagram for reaction with pyridine.

Lastly, at 100°C the transition for MOF formation again appears to be 4 equivalents of pyrazole with respect to copper (II) nitrate with small crystals formed at these concentrations. Large blue spherical crystals are observed at the condition of 0.25 eq

Pyrazole /$Cu(NO_3)_2$ and 6 eq $H_2BDI/Cu(NO_3)_2$. These optimized conditions were further used to test synthesis with pyridine as a modulating reagent. Under the reaction contions, 4 eq Pyrazole /$Cu(NO_3)_2$, 0.25 eq $H_2BDI/Cu(NO_3)_2$, and 2 drops pyridine, blue cubic single crystal were observed. These results point to better control of crystal morphology and growth using pyridine rather than excess pyrazole.

As the optimal reaction conditions for PCN-352 were observed at 100^{o}C, similar reaction conditions were evaluated for the synthesis of new MOFs with H_2PBI and H_2BPBI. Screening at 100^{o}C for 3 days with DMA resulted in the formation of the new MOF, PCN-353 (Figure 27). At low pyrazole concentration, only amorphous powder is observed except for the mixed product at 2 eq pyrazole and .25 eq H_2PBI. Above 4 equivalents of pyrazole, solely PCN-352 is synthesized. The optimal condition based on excess pyrazole were 6 eq Pyrazole/$Cu(NO_3)_2$ and .15 $H_2PDI/Cu(NO_3)_2$ forming crystals with undefined morphology. These conditions were further tested with pyridine yielding PCN-353 at conditions above 4 eq of pyrazole. The use of pyridine allowed for the formation of blue cubic crystals at lower pyrazole concentration. These crystals were later characterized by X-ray diffraction.

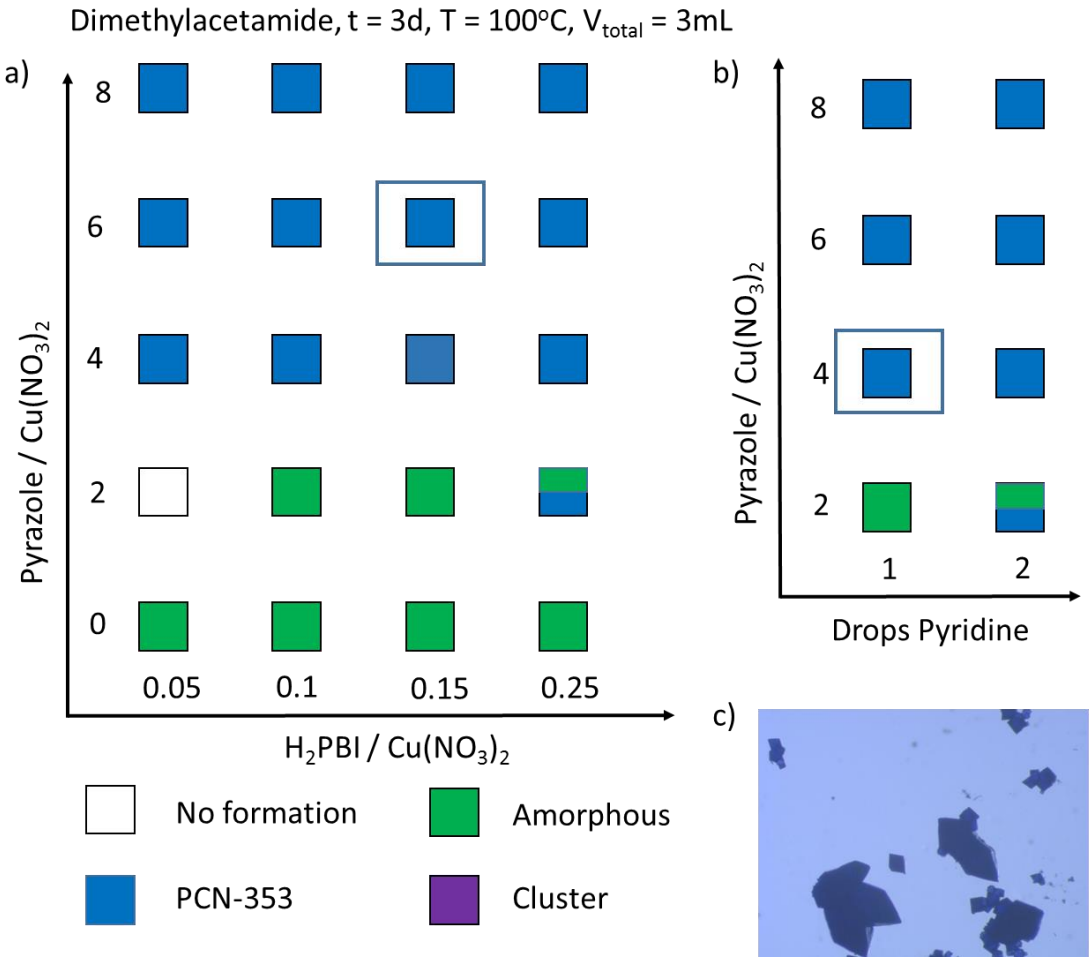

Figure 27 Single crystal material and crystallization diagrams for the high-throughput investigation of the system Pyrazole /$Cu(NO_3)_2$ and $H_2PBI/Cu(NO_3)_2$ in DMA at 100 ° C for 3 days based on powder XRD measurements. a) crystallization diagram for reaction with excess pyrazole, b) crystallization diagram for reaction with pyridine, and c) blue cubic crystals of PCN-353 obtained with 1 drops pyridine.

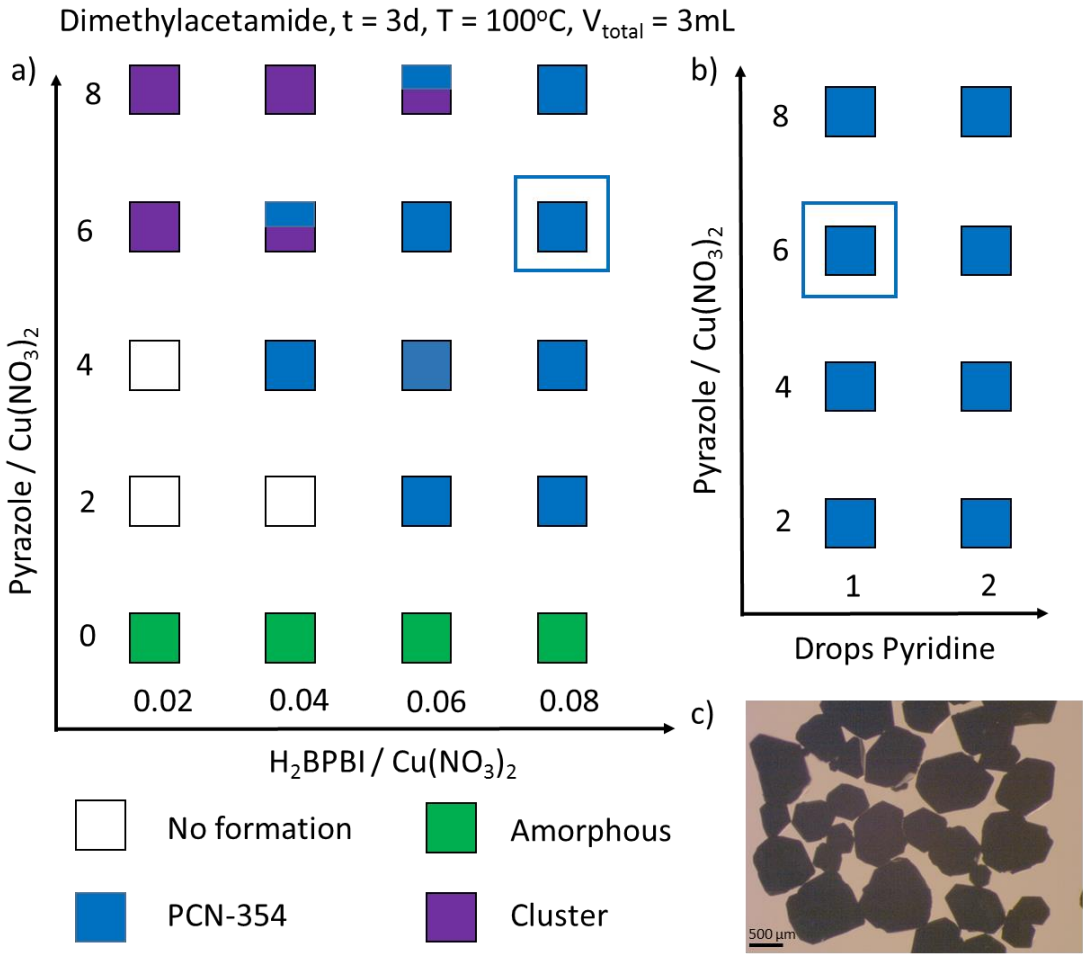

Figure 28 Single crystal material and crystallization diagrams for the high-throughput investigation of the system Pyrazole /$Cu(NO_3)_2$ and H2BPBI/$Cu(NO_3)_2$ in DMA at 100 ° C for 3 days based on powder XRD measurements. a) crystallization diagram for reaction with excess pyrazole, b) crystallization diagram for reaction with pyridine, and c) black octahedral crystals of PCN-354 obtained with 1 drops pyridine.

Lastly, the crystallization conditions were tested with the H_2BPBI linker (Figure 26) yielding similar results to PCN-352 and PCN-353; however, MOF growth seems independent of modulating reagent concentration at higher ligand concentration (0.08 eq H_2BPBI). Cluster formation is observed at low H_2BPBI concentration and high pyrazole

concentration. PCN-354 was obtained as octahedral black crystals at the following reaction conditions: 6 eq Pyrazole/$Cu(NO_3)_2$ and .08 $H_2BPBI/Cu(NO_3)_2$ with or without pyridine modulating reagent.

Structural Studies. Due to the large porosity of these MOFs, solving the crystal structure through single crystal X-ray diffraction is challenging due to void space within the molecule. For this reason, powder X-ray samples were measured at both Argonne National Laboratory at beamline 17-BM and Lawerence Berkeley National Laboratory at Beamline 11.3.1. This data was paired with single crystal measurements performed at Argonne National Laboratory beamline 15-BM. PCN-353 and PCN-354 both exhibit cubic symmetry and crystallize in the $Pa\ \bar{3}$ space group.

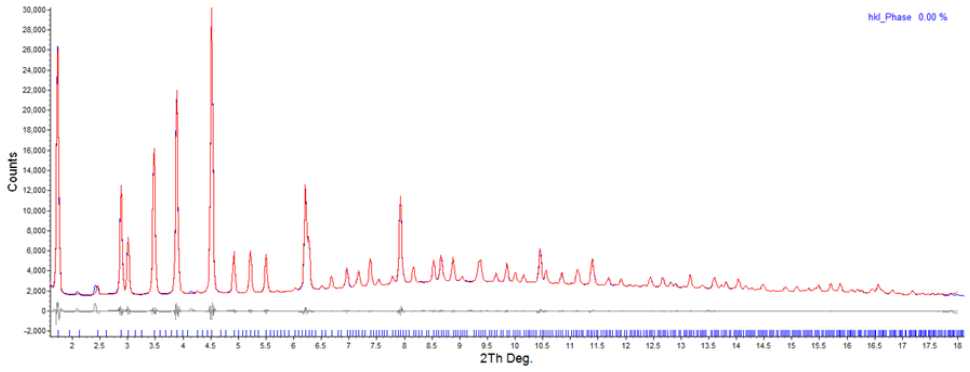

Figure 29 Pawley whole powder pattern decomposition for PCN-353. Red line is the calculated pattern, blue line is experimental pattern, and gray line is difference in patterns.

Pawley powder pattern decomposition was used to match the experimental pattern with the simulated structure and the fit is well matched (Figure 29). The structure of PCN-

353 and 354 is composed of three molecular cages, 12-connected cuboctahedral cages, truncated octahedral cages, and truncated tetrahedral cages (Figure 30 and Figure 31). The twist of the ligand from PCN-352 is not observed in these structures due to the absence of chirality in the linkers. With the elongation of the linker, the cages are enlarged and stretch into the mesoporous domain.

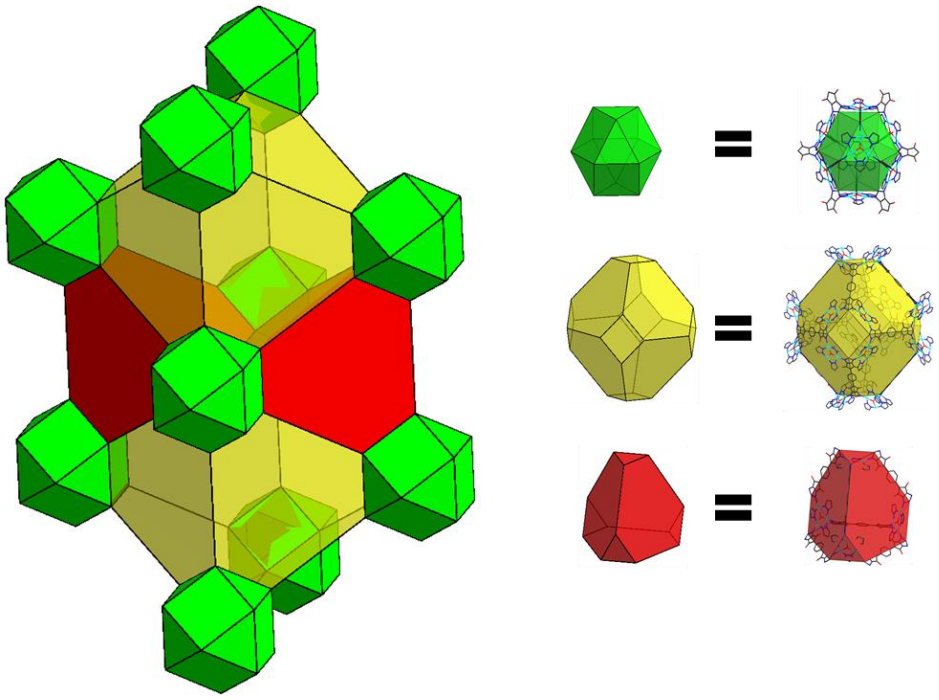

Figure 30 Structural representation of PCN-353 and PCN-354 and packing of molecular cages. a) cuboctahedral cage, b) truncated octahedral cage, and c) truncated tetrahedral cage.

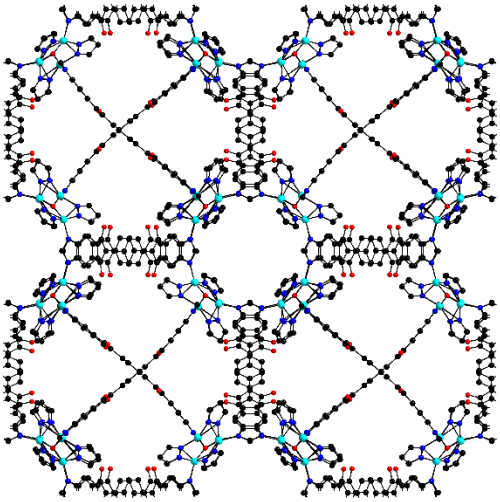

Figure 31 Structure of PCN-353. cubic, space group $Pa\bar{3}$, a = 47.9128 b = 47.9128 c = 47.9128 α = 90.00 β = 90.00 γ = 90.00. Cu = turquoise; C = black; N= dark blue O = red; H and coordinated solvent excluded, for clarity.

Porosity and Nitrogen Uptake. Nitrogen isotherms at 77K were measured to determine surface area once activated by supercritical point CO_2 drying. PCN-353 exhibits a high uptake of N_2 (~1000 cm^3/g at 1 bar) and surface area (3085 m^2/g) with characteristic mesoporous adsorption isotherm. PCN-354 exhibits lower N_2 uptake (~500 cm^3/g) and BET surface area (1845 m^2/g) most likely due to framework collapse as no signs of mesoporosity are observable in the isotherm.

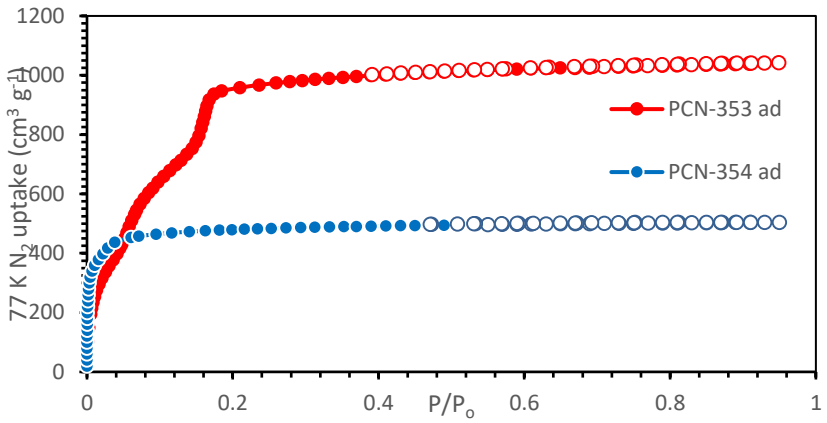

Figure 32 Nitrogen isotherms of PCN-353 and PCN-354 measured at 77K.

4.4 CONCLUSIONS

In this section, the optimized synthesis of PCN-352 is reported and these results were utilized to perform the reticular synthesis of PCN-353 and PCN-354. These MOF have been isolated using high-throughput synthesis and the effects of temperature, ligand-to-metal ratios, and modulation reagents have been observed. The use of pyridine instead of pyrazole as a modulating reagent increases the uniformity of crystal morphology for the PCN-35x series. Indicating that the use of non-bridging or topologically different modulating reagents may need to be explored in other areas of MOF synthesis. These MOFs were characterized by synchrotron single crystal X-ray diffraction to determine unit cells and refined using synchrotron powder X-ray diffraction. The MOFs exhibit enhanced porosity and high N_2 uptakes and high BET surface area (3085 m^2/g and 1845 m^2/g, respectively).

5. TOPOLOGY GUIDED DESIGN AND SYNTHESES OF HIGHLY STABLE MESOPOROUS PORPHYRINIC ZIRCONIUM MOFS WITH HIGH SURFACE AREA*

Through a topology guided strategy, a series of Zr_6 containing isoreticular porphyrinic MOFs, PCN-228, PCN-229 and PCN-230, with *ftw-a* topology were synthesized using the elongated porphyrinic linkers. The highly conjugated porphyrin ring effectively prevents the network interpenetration which often appears in MOFs with increased linker length. The pore aperture of the structures range from 2.5 nm to 3.8 nm and among them PCN-229 demonstrates the highest porosity and BET surface area among the previously reported Zr-MOFs. Additionally, by changing the relative direction of the terminal phenyl rings, this series replaces a Zr_8 cluster with a smaller Zr_6 cluster in a topologically identical framework. The high connectivity of the Zr_6 cluster yields frameworks with enhanced stability despite high porosity and ultra-large linker. As a representative example, PCN-230, constructed with the largest porphyrinic linker, shows excellent stability in aqueous solutions with pH values ranging from 0 to 12 and demonstrates one of the highest pH tolerances among all porphyrinic MOFs. This work not only presents a successful example of rational design of MOFs with desired topology, but also provides a strategy for construction of stable mesoporous MOFs.

5.1 INTRODUCTION

Mesoporous metal-organic frameworks (MOFs) have attracted great interest as heterogeneous platforms to immobilize or encapsulate functional moieties, such as organometallic catalysts, nanoparticles and enzymes.[23, 89-92] However, compared with the well-explored microporous MOFs, mesoporous MOFs are relatively under-developed. This is ascribed to the difficulty in organic linker extension, challenges in activation of MOFs with ultra-large pores, as well as the common appearance of undesired interpenetration.[23, 93] Moreover, the stability of the framework becomes difficult to maintain after extension of the organic linker, especially for mesoporous materials whose applications are usually conducted under aqueous or harsh chemical environments. The majority of reported carboxylate containing MOFs are constructed with relatively soft Lewis acidic metal species, such as Cu^{2+} and Zn^{2+}. The weak coordination bond between the soft Lewis acid and hard Lewis base causes their low stability and severely hampers further exploration of their potential.[94] To improve the chemical stability of MOFs, hard Lewis acidic species such as Al^{3+}, Fe^{3+}, Cr^{3+} and Zr^{4+}, which can form much stronger bonds with carboxylates, are often incorporated.[3, 14, 26, 69, 95-103] Despite thus adjustment, as isoreticular chemistry is applied to augment the internal cavity of known MOF structures, the pore size and stability are usually inversely correlated.

One strategy to compensate for the low stability of MOFs constructed with large linkers is to increase the connectivity of either organic linkers or inorganic clusters.[104-105] The Zr_6 cluster ($Zr_6O_4OH_4(COO)_{12}$), which has the highest connectivity among reported zero dimensional (0-D) inorganic nodes in MOFs, is an outstanding example which

endows the framework with excellent stability.[14, 95, 100, 102, 106] In particular, when the linker also exhibits high connectivity, the obtained MOFs are manifested to be robust even with very large pore size.[107] Hence, further increasing the overall connectivity of Zr-MOFs could be an effective strategy allowing construction of highly stable mesoporous MOFs with ultra-large linkers.

Porphyrinic derivatives as organic linkers have been extensively explored in MOFs due to their versatile functionality, such as catalysis, light harvesting and sensing.[108-115] Moreover, porphyrinic linkers usually have very large size (~2 nm), which assists in generating large pores inside the frameworks, resulting in mesoporous MOFs. In order to achieve the high connectivity, we used elongated tetratopic carboxylate porphyrin ligand H_4TCPP (tetrakis (4-carboxyphenyl) porphyrin) and the twelve connected Zr6 cluster to construct mesoporous MOFs. The fully occupied Zr_6 is twelve-connected with Oh symmetric and the free H_4TCPP is four-connected with D_{4h} symmetry (Figure 1). Topological connection of these two nodes to each other could ideally give rise to a high connected ftw-a network. However, not only the connectivity and symmetry of nodes, but also the direction and relative position between each node are crucial for topological design and the latter is often neglected when modulating the building units to obtain the desired structure. In other words, even if both connectivity and symmetry are perfectly matched, it is still not possible to form the expected framework if the relative directions of nodes are not correctly arranged.[116-120]

Herein, guided by topology and symmetry, porphyrinic linkers (named as H_4TCP-1, H_4TCP-2 and H_4TCP-3) were elongated with desired conformation by arranging the

vicinal phenyl ring and carboxylate group. Through combination of the organic linkers and twelve connected Zr_6 cluster, a series of mesoporous MOFs with ftw-a topology, namely PCN-228, PCN-229, and PCN-230 (PCN stands for the porous coordination network) were synthesized. The pore size of these MOFs ranges from 2.5 nm to 3.8 nm and PCN-229 shows both the highest porosity as well as BET surface area among all the previously reported Zr-MOFs. Moreover, the ligand extension does not impair the stability of the material. PCN-230, as a representative, which is constructed with the largest linker, shows excellent stability in aqueous solutions with pH ranging from 0 to 12, demonstrating the highest pH tolerance among all previously reported porphyrinic MOFs.

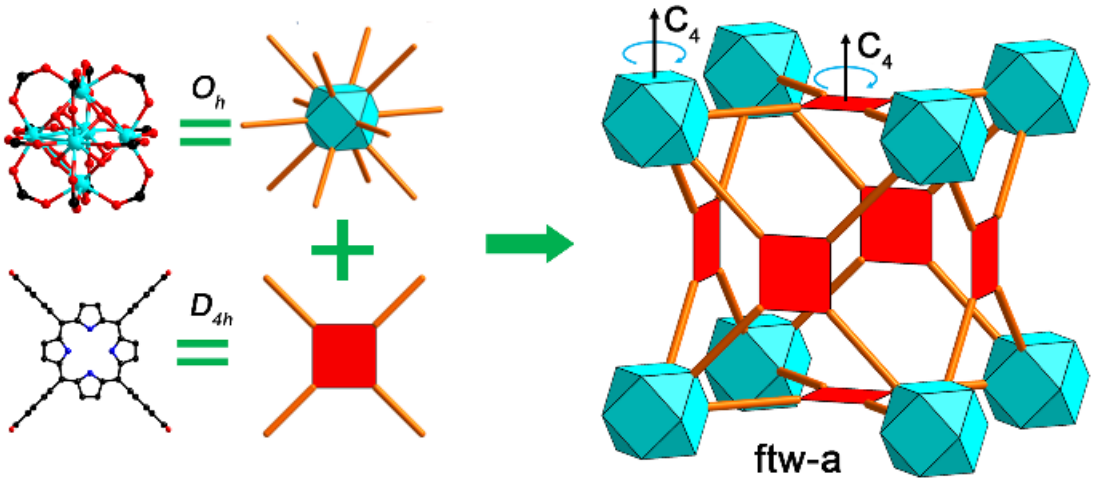

Figure 33 Assembly of Oh and D4h nodes into *ftw-a* network.

5.2 EXPERIMENTAL SECTION*

General Information. Zirconium(IV) chloride, N,N-dimethylformamide (DMF), Hexanes, Ethyl acetate, Methanol (MeOH), Ethanol (EtOH), Tetrahydrofuran (THF), Triethylamine (Et_3N), Dichloromethane (CH_2Cl_2), Acetone, Hydrochloride acid (HCl), 1, 2-Dimethoxyethane (DME), Tetra-n butylammonium fluoride 1M soln in THF (TBAF), Boron triflouride (BF_3OEt_2), Sodium Hydroxide (NaOH), Copper (I) iodide (CuI), 3, 4-dicholoro-5, 6-dicyano-1, 4-benzoquinone (DDQ), Ethyl - 4 - iodobenzoate, 4-Bromobenzaldehyde were all purchased from Alfa Aesar. 1.4 Diiodo-2, 5-dimethyl benzene, 1, 4-Diethyloxybenzene were purchased from TCI. Bis (triphenylphosphine) palladium (II) Dichloride ($Pd(PPh_3)_2Cl_2$) was purchase from Matrix Scientific. Trimethylsilyl acetylene was purchased from Oakwood. 3, 4-Diethyl pyrrole was purchased from Frontier. 4-Methoxy carbonylphenylboronic acid was purchased from AK Scientific Inc.

Instrumentation. The powder X-ray diffraction patterns (PXRD) were recorded on a BRUKER D8-Focus Bragg-Brentano X-ray Powder Diffractometer equipped with a Cu sealed tube (λ = 1.54178 Å) at room temperature. Synchrotron-based powder diffraction (APS) experiments were performed at the 17-BM beamline of the Advance Photon Source in Argonne National Laboratory. The simulated PXRD spectra were obtained by the diffraction-crystal module of the Mercury program based on the single-

* Ligand and MOF synthesis performed with assistance of Tian-fu Liu, Dawei Feng, Lanfang Zou. Structural studies were performed with assistance from Ying-pin Chen, Mathieu Bosch, and Zhangwen Wei.

crystal data. The program is available free of charge via internet at http:/www.iucr.org. Thermogravimetric analysis (TGA) was conducted on a TGA-50 (SHIMADZU) thermogravimetric analyzer in the air atmosphere. Nuclear magnetic resonance (NMR) data were collected on a Mercury 300 spectrometer. Gas sorption measurements were conducted using a Micrometritics ASAP 2020 system at different temperatures. PCN-229 or PCN-230 were activated by supercritical carbon dioxide using MADRIDE prior to gas adsorption.

Synthesis of 1. 4-Bromobenzaldehyde (1.8 g, 10 mmol), 4-Methoxy carbonylphenylboronic acid (1.79 g 10 mmol) $Pd(PPh_3)_2Cl_2$ (288 mg, 0.4 mmol) and CuI (57 mg, 0.3 mmol) were charged in a three-necked round bottom flask. The flask was connected to the Schlenk line then vacuum and refilled nitrogen alternately for three time. 150 mL dimethyoxyethane (DME) was bubbled with nitrogen for 30 min at room temperature (RT) to degas, then was added through a cannula. The mixture was stirred and heated to reflux for 48h under the nitrogen atmosphere. After cooling it to RT, The solvent was removed and the residual powder was dissolved in CH_2Cl_2 (100 mL) and H_2O (100 mL). The aqueous phase was extracted with CH_2Cl_2 (50 mL) four times. The mixed organic phase was dried with $MgSO_4$. After the solvent was removed, the crude product was recrystallized by acetone/methanol to give the white product 1.5 g. (yield. 62%).^{1}H NMR (300 MHz, $CDCl_3$) δ 10.11 (s, 1H) 8.02 (d, J = 7.99 Hz, 2H), 8.18 (d, J = 7.99 Hz, 2H), 7.82 (d, J = 8.22 Hz, 2H), 7.74 (d, J = 7.99 Hz, 2H), 3.99 (s, 3H).

Synthesis of 2 and H_4TCP-1. A solution of **1** (1.5 g, 6.25 mmol) in dry CH_2Cl_2 450 mL was charged in a two-necked round bottom flask under nitrogen atmosphere

followed by the addition of 0.85 mL (6.25 mmol) 3, 4-Diethyl pyrrole. After stirring 15 min, BF_3OEt_2 0.15 mL was add and the mixture was stirred for more 2 h at RT. DDQ (3, 4-dicholoro-5, 6-dicyano-1, 4-benzoquinone, 1 g, 4.4 mmol) were added and reflux another 2 h to complete the reaction. The solvent was evaporated followed by recrystallization in CH_2Cl_2 / Methanol (0.5% NaOH) 150 mL. **2** was obtained as green powder after filtration. The obtained ester was stirred in a 90 mL mixture of THF : MeOH : H_2O = 1 : 1 : 1, to which 1.4 g NaOH was added and heated to reflux overnight. After cooling to RT, the mixture was filtered to obtain green solid. The solid was then stirred in 50 mL water and acidified with 20% HCl. After heating and stirring the mixture for 2 h, green solid was collected by filtration, washed with water and dried in vacuum to give 1.1g (0.83mmol) pure compound H_4TCP-1 (yield. 53%).^{1}H NMR (300 MHz, $CDCl_3$) δ 8.72 (d, 8H), 8.18 (d, 8H), 8.03 (d, 8H), 7.82(d, 8H), 2.11 (b, 16H), 0.71 (b, 24H). Refluxed $NiCl_2$ (500 mg) and H_4TCP-1 (300 mg) in DMF solution for 12 hours to get the H_4TCP-1-Ni complex for Mass spectroscopy (for better solubility).

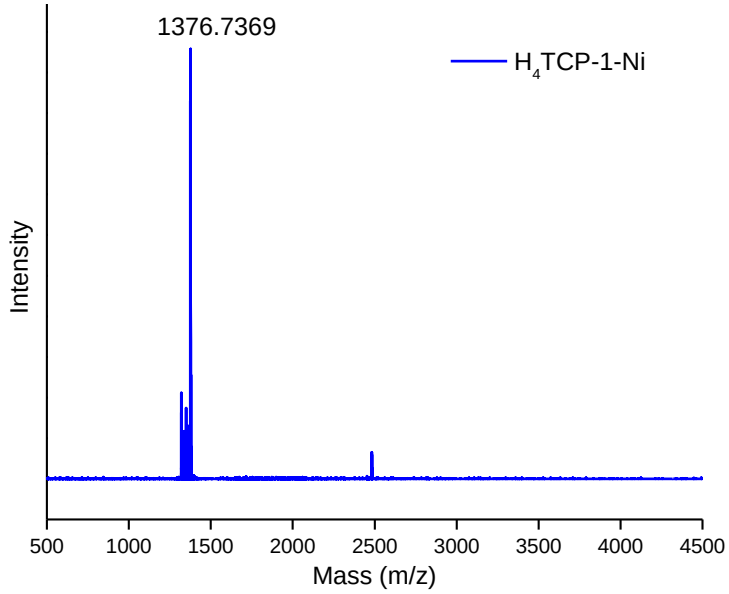

Figure 34 MALDI MS (positive ion mode) of H_4TCP-1-Ni (theoretical mass 1376.2604).

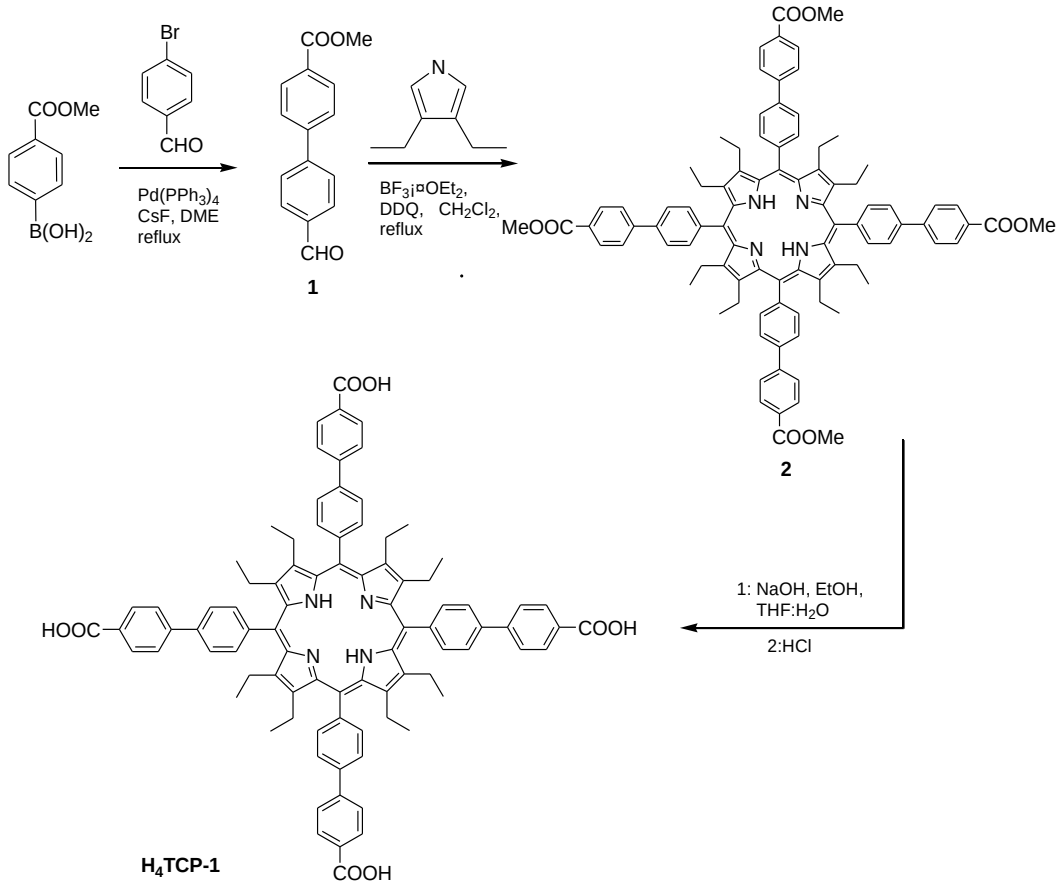

Scheme 5 Synthesis of **H_4TCP-1.**

Synthesis of 3. Ethyl-4-iodobenzoate (2.7 g, 10 mmol), $Pd(PPh_3)_2Cl_2$ (288 mg, 0.4 mmol) and CuI (57 mg, 0.3 mmol) were charged in a three-necked round bottom flask followed by three evacuation and refill cycles with nitrogen on a schlenk line. A 200 mL mixture of Et_3N: THF = 1:1 was bubbled with nitrogen for 30 min at RT to degas, and added to the reaction flask through a cannula. Trimethylsilyl acetylene (1.7 mL, 12 mmol) was added by syringe. The mixture was stirred at RT for 5 h under nitrogen atmosphere. The solvent was removed and the crude product was purified by a short column (EtOAc /

n-hexane = 1/6) to yield yellow oil 2.1 g. (yield. 85%). ^{1}H NMR (300 MHz, $CDCl_3$) δ 7.98 (d, 2H), 7.52(d, 2H), 4.38 (q, 2H), 1.38 (t, 3H), 0.25 (s, 9H).

Synthesis of 4. 3 (2.95 g, 12 mmol), 4-Bromobenzaldehyde (2.6g 14mmol), $Pd(PPh_3)_2Cl_2$ (316 mg, 0.45 mmol) and CuI (57 mg, 0.3 mmol) were charged in a three-necked round bottom flask followed by three evacuation and refill cycles with nitrogen on a schlenk line. A 200 mL mixture of Et_3N: THF = 1:1 was bubbled with nitrogen for 30 min at RT to degas, then was added to the reaction flask through a cannula. TBAF (Tetra-n butylammonium fluoride 1M soln in THF) 12mL was added dropwise and the resulting mixture was stirred at RT for 4 h under nitrogen atmosphere. The solvent was removed and the residual powder was recrystallized by acetone / Methanol (150 mL) to give a white product 1.52 g. (yield. 45%). ^{1}H NMR (300 MHz, $CDCl_3$) δ 10.07 (s, 1H), 8.09 (d, J = 8.14 Hz, 2H), 7.92 (d, J = 8.06 Hz, 2H), 7.73 (d, J = 8.37 Hz, 2H), 7.65 (d, J = 8.16 Hz, 2H), 4.43 (q, J = 7.12 Hz, 2H) 1.44 (t, J = 7.14 Hz, 3H).

Synthesis of 5 and H_4TCP-2. A solution of **4** (2.55 g 9.1 mmol) in dry CH_2Cl_2 550 mL was charged in a two-necked round bottom flask under nitrogen atmosphere followed by the addition of 1.22 mL (9.1 mmol) 3,4-Diethyl pyrrole. After stirring 15 min, BF_3OEt_2 0.17 mL was added and the mixture was stirred for 2 h at RT. DDQ (1.6 g, 7 mmol) was added and reflux another 2 h to complete the reaction. The solvent was evaporated followed by recrystallization in CH_2Cl_2 / Methanol (0.5% NaOH) 150 mL. **5** was obtained as green powder after filtration. The obtained ester was stirred in a 120 mL mixture of THF : MeOH : H_2O = 1 : 1 : 1, to which 2 g NaOH was added and heated to reflux overnight. After cooling to RT, the mixture was filtered to obtain green solid. The

solid was stirred in 50 mL water and acidified with 20% HCl. After heating and stirring the mixture for 2h, green solid **5** was collected by filtration, washed with water and dried in vacuum to give 1.4 g (0.99 mmol) pure product H_2TCP-2 (yield. 44%). ^{1}H NMR (300 MHz, $CDCl_3$) δ 8.73 (d, 8H), 8.22 (d, 8H), 8.09 (d, 8H), 7.87(d, 8H), 2.15 (b, 16H), 1.36 (b, 24H).

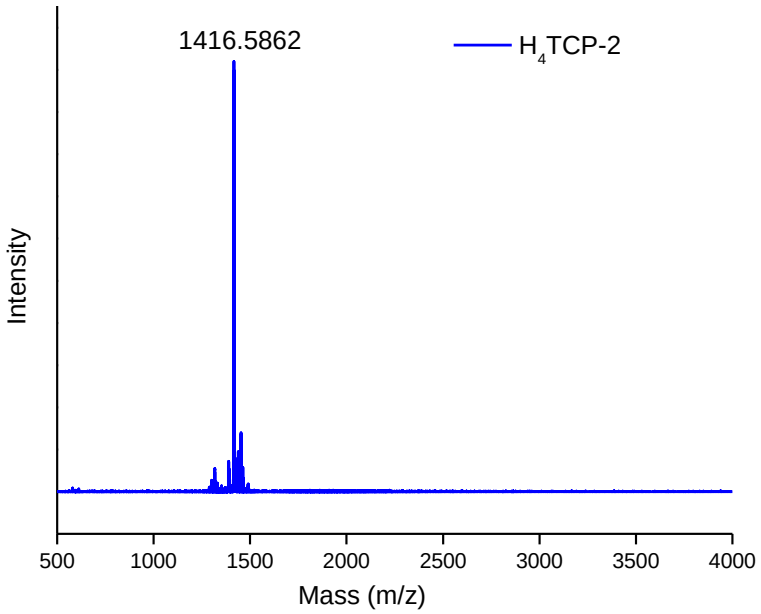

Figure 35 MALDI MS (positive ion mode) of H_4TCP-2 (theoretical mass 1416.5925).

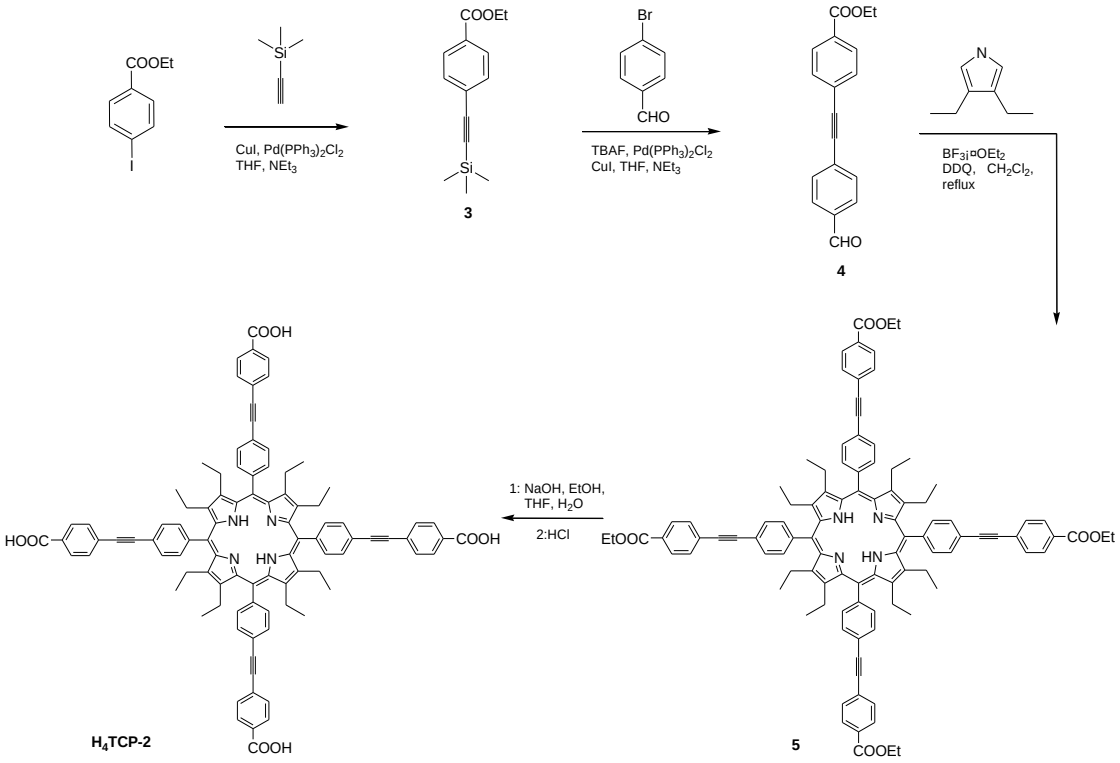

Scheme 6 Synthesis of **H_4TCP-2.**

Synthesis of 6. 3 (2.46 g, 10mmol) was dissolved in 60 mL THF and stirred at RT. TBAF 10mL was added and the mixture was allowed to react for 15min. The solvent was then removed and the crude product was purified by a short column (EtOAc / n-hexane = 1/7) to give the yellow oil **6** 1.6 g. (yield. 92%). ^{1}H NMR (300 MHz, $CDCl_3$): δ 7.99 (d, 2H), 7.51 (d, 6H), 4.39 (q, 2H), 3.22 (s, 1H) 1.37 (t, 3H).

Synthesis of 7. A mixture of Xylene (1.78 g, 16.8 mmol), I_2 (6.86 g, 27 mmol), HIO_4•$2H_2O$ (3.1 g, 13 mmol) was placed into a 100 ml flask, and H_2SO_4 (1 ml), CH_3COOH (24mL), H_2O (5 ml) was added into flask, and the mixture was stirred at 90°C

for 10h. The reaction mixture was diluted with 250 ml water to remove acid and the resulted precipitate was filtered, and washed with Methanol to yield the white solid **7** 5.4 g. Yield: 80 %. 1H NMR (300 MHz, $CDCl_3$): δ 7.68 (s, 2H), 2.37 (s, 6H)

Synthesis of 8. **7** (3.5 g, 10 mmol), $Pd(PPh_3)_2Cl_2$ (288 mg, 0.4 mmol) and CuI (57 mg, 0.3 mmol) were charged in a three-necked round bottom flask followed by three evacuation and refill cycles with nitrogen on a schlenk line. A 200 mL mixture of Et_3N: THF = 1:1 was bubbled with nitrogen for 30 min at RT to degas, then was added to the reaction flask through a cannula. Trimethylsilyl acetylene (1.1 mL, 8 mmol) was added by syringe. The mixture was stirred at RT for 5h under nitrogen atmosphere. The solvent was removed and the crude product was purified by column (hexane) to give **8** as yellow oil 1.6g (yield. 63% based on Trimethylsilyl acetylene).1H NMR (300 MHz, $CDCl_3$) δ 7.68 (s, 1H), 7.30 (s, 1H), 2.37 (s, 6H), 0.28 (s, 9H).

Synthesis of 9. **6** (1.74 g 10 mmol), **8** (3.27 10mmol) $Pd(PPh_3)_2Cl_2$ (316 mg, 0.45 mmol) and CuI (57 mg, 0.3 mmol) were charged in a three-necked round bottom flask followed by three evacuation and refill cycles with nitrogen on a schlenk line. A 200 mL mixture of Et_3N: THF = 1:1 was bubbled with nitrogen for 30 min at RT to degas, then was added to the reaction flask through a cannula. The resulting mixture was stirred at RT for 4 h under nitrogen atmosphere. The solvent was removed and the residual powder was purified by column (EtOAc / n-hexane = 1/7) to give the white product 1.91 g. (yield. 51%). ^{1}H NMR (300 MHz, $CDCl_3$) δ 8.05 (d, J = 8.65 Hz, 2H), 7.60 (d, J = 8.65 Hz, 2H), 7.36 (d, J = 7.85 Hz, 2H), 4.42 (q, J = 7.13 Hz, 2H), 2.44 (d, J = 14.87 Hz, 6H), 1.43 (t, J = 7.13 Hz, 3H), 0.29 (s, 9H)

Synthesis of 10. 9 (1.87 g, 5 mmol), 4-Bromobenzaldehyde (0.91g 5 mmol), $Pd(PPh_3)_2Cl_2$ (288 mg, 0.4 mmol) and CuI (57 mg, 0.3 mmol) were charged in a three-necked round bottom flask. The flask was connected to the Schlenk line then vacuum and refilled nitrogen alternately for three time. A 200 mL mixture of Et_3N: THF = 1:1 was bubbled with nitrogen for 30 min at RT to degas, then was added to flask through a cannula. TBAF 5mL was added dropwise and the resulting mixture was stirred at RT for 4 h under the nitrogen atmosphere. The solvent was removed and the residual powder was recrystallized by acetone / CH_2Cl_2 (150 mL) to give the white product 1.72 g. (yield. 84%). ^{1}H NMR (300 MHz, $CDCl_3$) δ 10.06 (s, 1H), 8.07 (d, J = 8.64 Hz, 2H), 7.91 (d, J = 8.51 Hz, 2H), 7.71 (d, J = 8.17 Hz, 2H), 7.62 (d, J = 8.66 Hz, 2H), 7.44 (s, 2H), 4.43 (q, J = 7.13 Hz, 2H), 2.52 (s, 6H), 1.44 (t, J = 7.13 Hz, 3H).

Synthesis of 11 and H_4TCP-3. A solution of **10** (2.03 g 5 mmol) in dry CH_2Cl_2 600 mL was charged in a two-necked round bottom flask under nitrogen atmosphere followed by the addition of 0.67 mL (5 mmol) 3,4-Diethyl pyrrole. After stirring 15 min, BF_3OEt_2 0.17 mL was added and the mixture was stirred for 2 h at RT. DDQ (1.6 g, 7 mmol) was added and reflux another 2 h to complete the reaction. The solvent was evaporated followed by recrystallization in CH_2Cl_2 / Methanol (0.5% NaOH) 150 mL. **11** was obtained as green powder after filtration. The obtained ester was stirred in a 120 mL mixture of THF : MeOH : H_2O = 1 : 1 : 1, to which 2.5 g NaOH was added and heated to reflux overnight. After cooling to RT, the mixture was filter to obtain green solid. The obtained solid was stirred in 60 mL water and acidified with 20% HCl. After heating and stirring the mixture for 2 h, green solid was collected by filtration, washed with water and

dried in vacuum to give 0.99 g (0.51 mmol) pure product H_4TCP-3 (yield. 41%) ^{1}H NMR (300 MHz, $CDCl_3$) δ 8.76 (d, 8H), 8.21(d, 8H), 8.04 (d, 8H), 7.74(d, 8H), 7.63 (s, 8H), 2.54~2.51 (m, 24H), 2.17 (b, 16H), 1.06 (b, 24H).

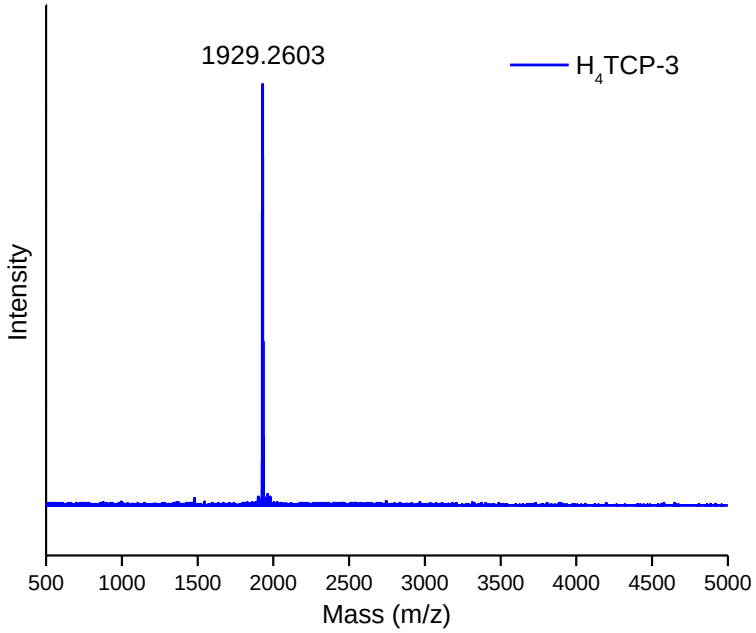

Figure 36 MALDI MS (positive ion mode) of H_4TCP-3 (theoretical mass 1928.8429).

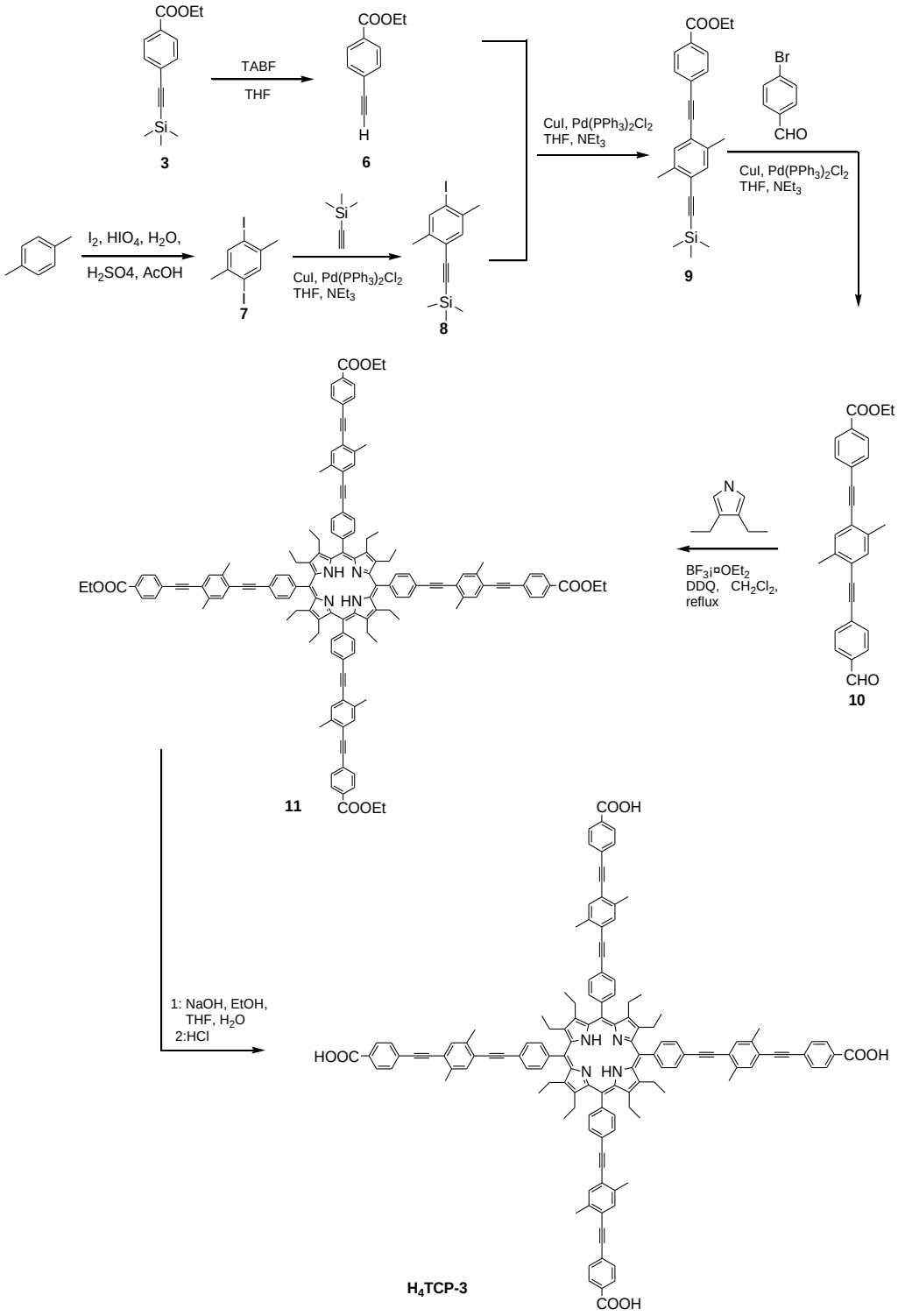

Scheme 7 Synthesis of **H4TCP-3.**

Synthesis of PCN-228 ($Zr_6(OH)_4O_4(TCP\text{-}1)_3$•10DMF•$2H_2O$). ZrCl4 (15 mg), H_4TCP-1 (15 mg) and benzoic acid (350mg) in 2 mL of DMF were ultrasonically dissolved in a 4 mL Pyrex vial. The mixture was heated to 120 ºC in an oven for 12 h. After cooling down to room temperature, dark green crystals 16 mg were harvested by filtration (Yield. 85%). Found. C, 67.51; H, 5.63; N, 4.56%.

Synthesis of PCN-229 ($Zr_6(OH)_4O_4(TCP\text{-}2)_3$•45DMF •$25H_2O$). ZrCl4 (15 mg), H_4TCP-2 1415 (15 mg) and benzoic acid (350mg) in 2 mL of DMF were ultrasonically dissolved in a 4 mL Pyrex vial. The mixture was heated to 120 ºC in an oven for 12 h. After cooling down to room temperature, dark green crystals 14 mg were harvested by filtration (Yield. 82%). Found. C, 56.98; H, 5.95; N, 7.20 %.

Synthesis of PCN-228'. Although we can obtain the single crystal of PCN-228, it's failed to get the single crystal X-ray diffraction data because of the small crystal size. However, using the similar ligands H_4TCP-1' (Scheme 1), we can obtained very large single crystal PCN-228' whose structure can be successfully determined by single crystal X-ray diffraction. The PXRD of PCN-228 is identical with the simulated PXRD of PCN-228' indicating the isostructure of these two MOFs. The structure and phase purity of PCN-228 thereby were determined. C_{216} H_{120} N_{12} Ni_3 O_{32} Zr_6

Synthesis of PCN-228'. $ZrCl_4$ (15 mg), H_4TCP-1' (15 mg) and acetic acid (0.4mL) in 2 mL of DMF were ultrasonically dissolved in a 4 mL Pyrex vial. The mixture was heated in 120 ºC oven for 12 h. After cooling down to room temperature, dark red crystals were harvested by filtration. Although we can obtain the single crystal of PCN-228, it's failed to get the single crystal X-ray diffraction data because of the small crystal

size. However, using the similar ligands H_4TCP-1' (Scheme 1), we can obtained very large single crystal PCN-228' whose structure can be successfully determined by single crystal X-ray diffraction. The PXRD of PCN-228 is identical with the simulated PXRD of PCN-228' indicating the isostructure of these two MOFs. The structure and phase purity of PCN-228 thereby were determined.

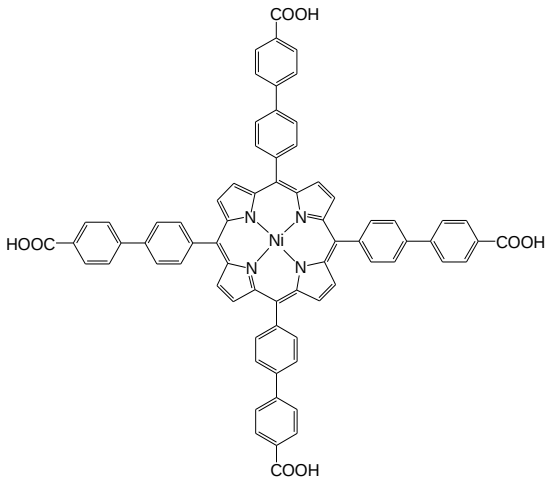

Figure 37 The structure of H_4TCP-1'.

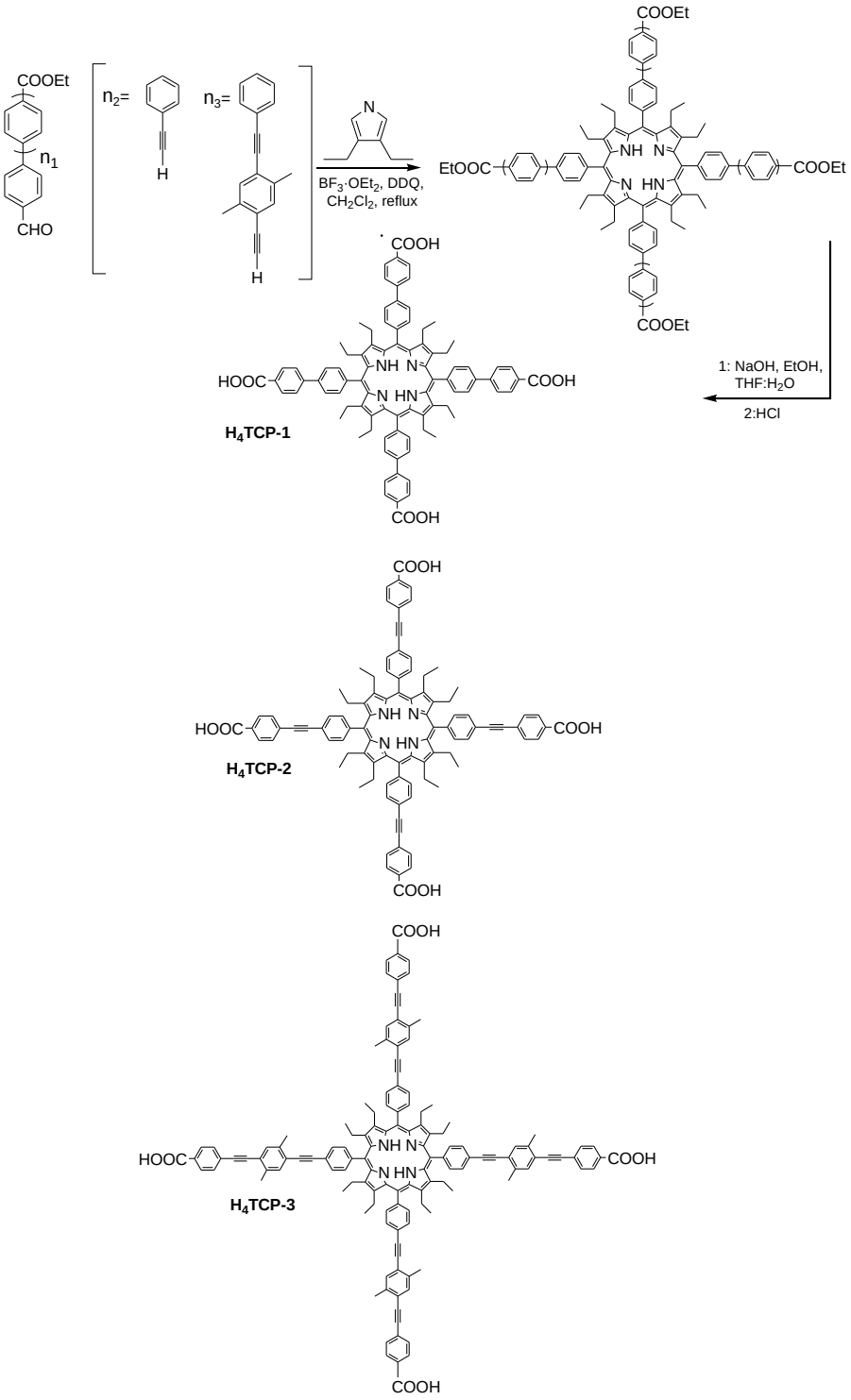

Scheme 8 Syntheses of **H_4TCP-1, 2 and 3** using the precursor of n_1, n_2, and n_3.

Synthesis of PCN-229 ($Zr_6(OH)_4O_4(TCP\text{-}2)_3$•45DMF •25$H_2O$). $ZrCl_4$ (15 mg), H_4TCP-2 (15 mg) and benzoic acid (350mg) in 2 mL of DMF were ultrasonically dissolved in a 4 mL Pyrex vial. The mixture was heated to 120 ºC in an oven for 12 h. After cooling down to room temperature, dark green crystals 14 mg were harvested by filtration (Yield. 82%). Found. C, 56.98; H, 5.95; N, 7.20 %.

Single X-ray Crystallography. Single crystal X-ray crystallographic data of PCN-228' and PCN-230 were collected on a Bruker single crystal APEXII CCD Diffractometer with Mo K_α (λ = 0.71073 Å) at 110 K. All structures were solved by direct methods and refined by full-matrix least-squares on F^2 using *SHELXTL*.[121] Non-hydrogen atoms were refined with anisotropic displacement parameters during the final cycles. Organic hydrogen atoms were placed in calculated positions with isotropic displacement parameters set to 1.2 × U_{eq} of the attached atom. The solvent molecules are highly disordered, and attempts to locate and refine the solvent peaks were unsuccessful. Contributions to scattering due to these solvent molecules were removed using the *SQUEEZE* routine of *PLATON*;[83] structures were then refined again using the data generated. Crystal data were summarized in Table 1. The CIF file can be obtained free of charge from the Cambridge Crystallographic Data Centre via www.ccdc.cam.ac.uk/data_request/cif (CCDC 1038049 for PCN-228', 1038050 for PCN-230). After the initial structural solution was found based on the single crystal X-ray diffraction data of PCN-228', the structures of PCN-228 and 229 were refined by a self-consistent iterative procedure in which successive geometry optimization calculations were performed using the Forcite module of Materials Studio 6.0.[62]

Gas Adsorption of PCN-228, PCN-229 and PCN-230. Before the gas sorption experiment, as-synthesized PCN-228(~100 mg) was washed twice with DMF and acetone, respectively. Fresh acetone was subsequently added, and the sample was allowed to soak for 24 h to exchange and remove the nonvolatile solvates (DMF). After the removal of acetone by decanting, the samples were activated by drying under vacuum, then dried again by using the 'outgas' function of the adsorption instrument for 5 h at 100 °C prior to gas adsorption/desorption measurement. For PCN-229 and PCN-230, the as-synthesized samples (~100 mg) were washed with DMF three times and then soaked in fresh DMF overnight. Afterwards, the samples were activated by supercritical CO_2 and then dried again by using the 'outgas' function of the adsorption instrument for 5 h at 100 °C prior to gas adsorption/desorption measurement.

Stability test of PCN-228, 229 and 230. About 200 mg of as-synthesized samples were separated into several portions and transferred to vials containing aqueous solutions with different pH values. After 24h, the samples were washed with fresh DMF twice for PXRD measurement or activated by supercritical CO_2 for N_2 adsorption.

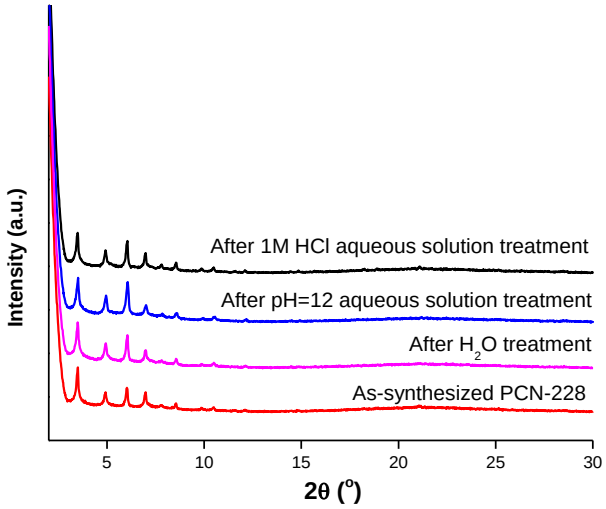

Figure 38 The PXRD of PCN-228 after treated with different aqueous solution.

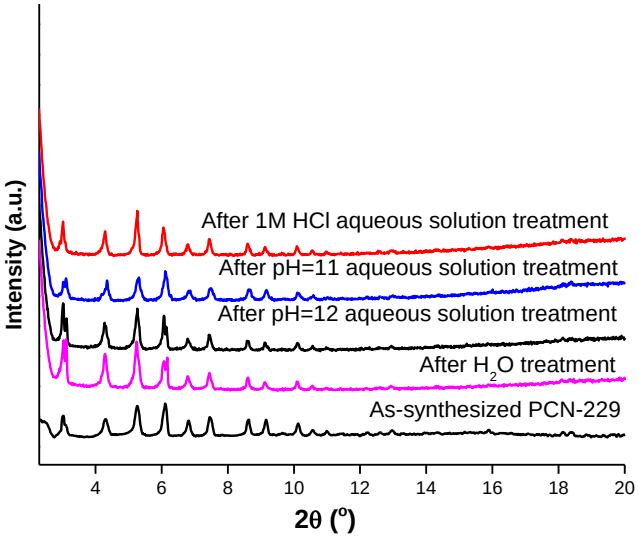

Figure 39 The PXRD of PCN-229 after treated with different aqueous solution.

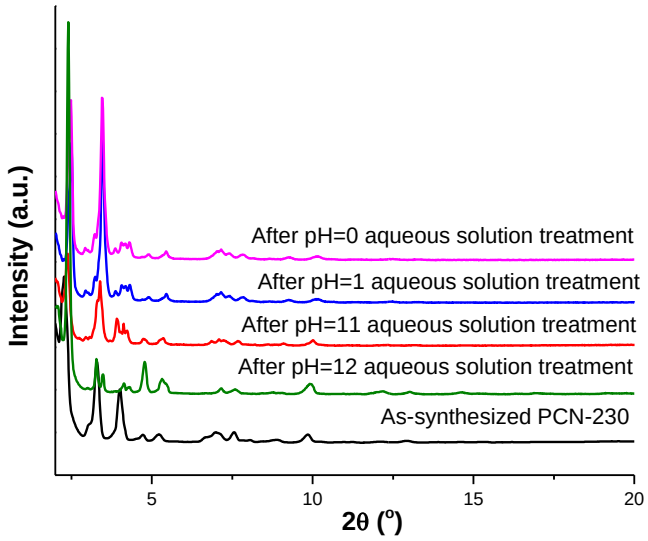

Figure 40 The PXRD of PCN-230 after treated with different aqueous solution.

5.3 RESULTS AND DISCUSSION

Porphyrinic ligands were chosen for reticular chemistry in this work for several reasons. The porphyrin ligand is synthesized from a condensation reaction; elongation of the precursor provides a facile method for the effective enlargement of the target ligands. The elongated porphyrin is relatively easier to synthesize compared with other organic linkers with comparable size. Additionally, the center of a porphyrin is a highly conjugated bulky solid ring, which usually inherently prevents interpenetration. Therefore, using a porphyrinic organic linker could be an effective approach to obtain extra-large pores in MOFs. Moreover, the porphyrin center endows the obtained mesoporous MOFs with versatile functionality which has potential for a wide array of applications. Owing to their

large size and the use of relatively soft Lewis acidic metal species as nodes, most reported porphyrinic MOFs suffer from weak stability, which severely hampers their application. Utilizing hard Lewis acidic species as inorganic nodes in porphyrinic MOFs has remarkably improved the chemical stability and extended their use under harsh chemical environments.[107, 116-120]

As shown in Figure 41, the ftw-a network is composed of the twelve connected O_h nodes and four connected D_{4h} nodes. However, when substituting the corresponding nodes with the twelve connected Zr_6 clusters and TCPP ligands to construct ftw-a topology, the peripheral phenyl rings have to rotate into the same plane with the porphyrin. The rotation on position I (Figure 41a) is forbidden because of the steric effect between the porphyrin ring and the phenyl ring. The rotation on position II would destroy the conjugated system between carboxylates and benzene rings, which is also highly energetically non-preferred. Therefore, these two building units are unable to form the ftw-a network because of their incompatible direction (Figure 41b). The previously reported Zr_6 cluster usually adopts reduced connectivity and symmetry to form other networks with TCPP;[107, 119-120] is fully occupied by TCPP with an energetically disfavored conformation;[120] or alternatively, the Zr_8 cluster needs to be incorporated with TCPP to construct the highly connected ftw-a network as represented in PCN-221 (Figure 41d). However, this framework is not stable in aqueous environments because of the charge unbalanced Zr_8 cluster.[118]

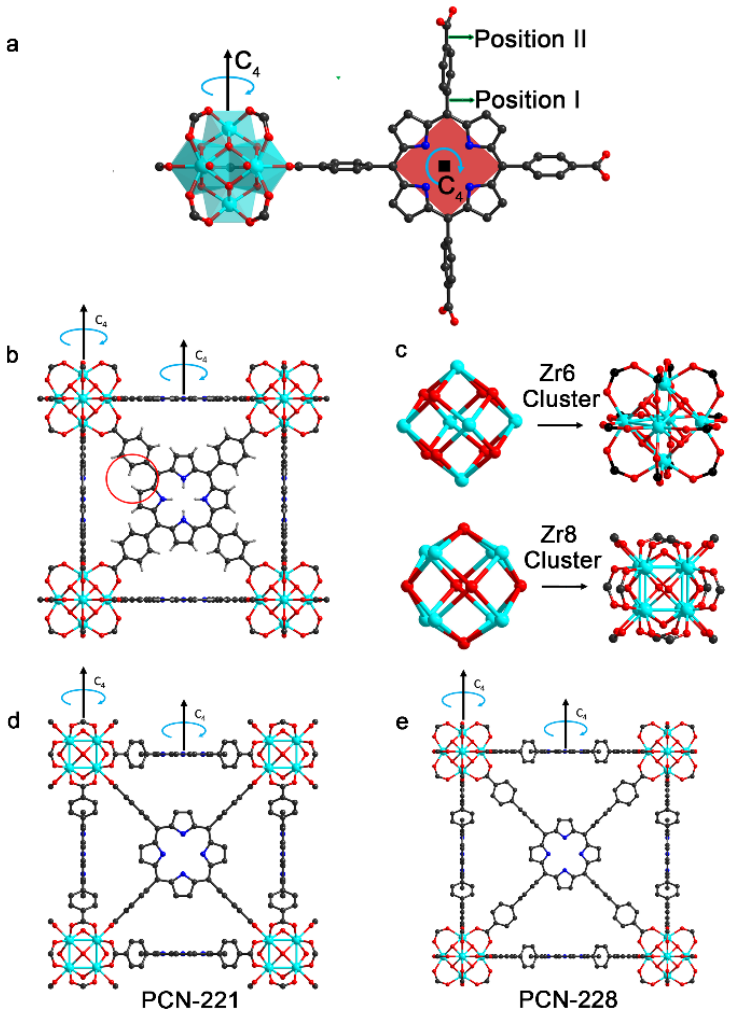

Figure 41 a) Representation of the connections between the O_h node and D_{4h} node when combining Zr_6 and H_4TCPP, and the sterically controlled phenyl and carboxylate angle. b) Substitution of the Zr_6 cluster and H_4TCPP in ftw-a topology and the chemically forbidden conformation of ligand (highlighted with red circle). c) Representation of the Zr_6 and Zr_8 cluster, and the 90° rotation of the carboxylate groups between these two clusters. d) Structure of PCN-221 constructed with Zr_8 cluster and H_4TCPP. e) Structure of PCN-228 constructed with Zr_6 cluster and H_4TCP-1 (ethyl groups were omitted for clarity).

To overcome such conflicts and construct stable mesoporous porphyrinic Zr-MOFs with ftw-a topology, the elongated porphyrinic ligand H_4TCP-1, H_4TCP-2 and H_4TCP-3 were designed with desired conformation by well-arranging the vicinal phenyl rings and carboxylate groups. By taking advantage of the steric effect between porphyrin center and connected phenyl rings as well as the adjacent two phenyl rings, the four carboxylate groups in H_4TCP-1 are likely to stay in the same plane with the porphyrin center which is necessary to form the ftw-a network with Zr_6. In contrast, we try to alleviate the steric effect as much as possible for H_4TCP-2 and H_4TCP-3. The ethynyl group is known to promote low or no barrier torsional motion for the vicinal phenyl rings.[122] In H_4TCP-2 and H_4TCP-3, ethynyl moieties were used for ligand elongation, which allow the peripheral benzoates to rotate freely to stay in the same plane as the porphyrin center without significantly increasing the inherent energy. Therefore, the ligands can adopt a compatible direction with the Zr_6 cluster to construct fta-w network. Meanwhile, eight ethyl substituents were introduced in the porphyrin rings aiming to increase the solubility of ligands (Scheme 8). Solvothermal reaction of H_4TCP-1 (H_4TCP-2 and H_4TCP-3), $ZrCl_4$ and acetic acid in DMF give rise to large dark green cubic crystals, namely PCN-228, PCN-229 and PCN-230 respectively (Figure 42a, 42b and 42c). Single crystal x-ray diffraction reveals a space group of $Pm\bar{3}m$ for PCN-228' and. The overall frameworks are based on uniform cubes, each of which has faces consisting of the porphyrinic linker.

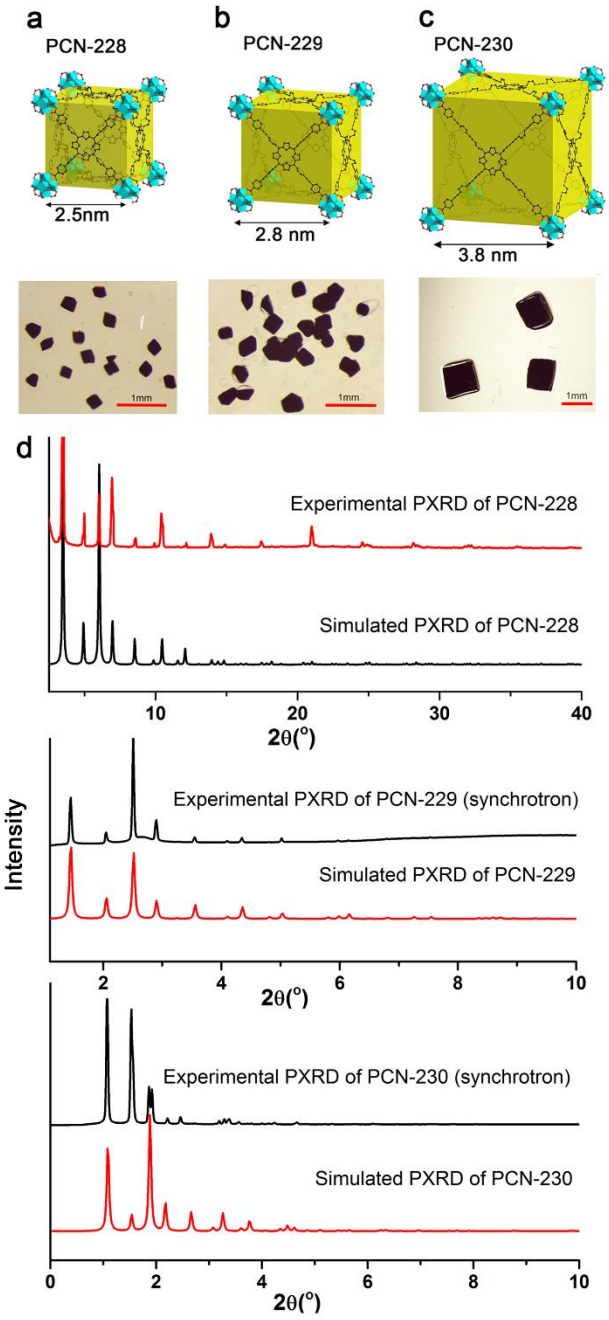

Figure 42 Structures and crystals of a) PCN-228, b) PCN-229, c) PCN-230, d) Experimental and simulated PXRD of PCN-228, 229 and 230. (Simulated PXRD of PCN-228 and PCN-229 were calculated from the simulated structure)

Although single crystals are also obtained for PCN-229, the diffraction is too weak to solve the structure due to their relatively small size. Hence, an isoreticular structure model of PCN-229 was constructed using Material Studio 6.0,15 and further confirmed by synchrotron powder X-ray diffraction (PXRD) collected at 17-BM beamline at Advanced Photon Source, Argonne National Laboratory. PCN-228 and PCN-230 are also confirmed by the PXRD patterns (Figure 42d). Due to the extra-large size of these porphyrinic linkers, all three MOFs are mesoporous with pore size ranging from 2.5 nm to 3.8 nm (Figure 42a, 42b and 42c). As we expected, all the peripheral benzoates stay in plane with the porphyrin center, which allows the formation of the ftw-a network with the twelve-connected Zr_6 cluster. Although these MOFs are constructed from Zr_6 clusters, they share the same space group and topology with PCN-221 wherein the peripheral benzoates in TCPP are perpendicular to the central porphyrin ring. Structural analysis of PCN-221 has shown the carboxylate groups of the Zr_8 cluster have a 90^o rotation compared with that of the Zr_6 cluster (Figure 41). With this orientation, these two nodes are compatible to form the ftw-a topology. However, even with theoretically qualified nodes, some reported zirconium porphyrin MOFs possess reduced connectivity and symmetry due to the incompatible directionality of the metal nodes and linker, resulting in the obtained frameworks with diminished pH stability compared with the 12-connected PCN-228 series.[98, 117, 119-120]These examples demonstrate that not only the symmetry, but also the relative direction of each node, must be considered in topological MOFs design.

To the best of our knowledge, PCN-230 exhibits the largest pore among all Zr-MOFs. If we consider Zr-MOF growth as a ligand substitution process taking place with

Zr clusters, it is a more entropically favored process when the connecting number on the cluster is higher.[57] Supposing that bond energy of the Zr-carboxylate bond is similar for different connectivity arrangements, the twelve-connected porphyrinic Zr-MOFs could be energetically more favored compared to other porphyrinic Zr-MOFs with lower connectivity (it should have a lower Gibbs free energy due to the entropy effect).

In order to assess the porosity of PCN-228, 229 and 230, we performed N_2 sorption measurement at 77 K. PCN-228, PCN-229 and PCN-230 show N_2 uptake of 1245 cm^3/g, 1455 cm^3/g and 1085 cm^3/g respectively (Figure 42a). The experimental Brunauer-Emmett-Teller (BET) surface area is 4510 m^2/g for PCN-228, 4619 m^2/g for PCN-229 and 4455 m^2/g for PCN-230. PCN-229 shows both the highest porosity and BET surface area among all the previously reported Zr-MOFs as well as among porphyrinic MOFs.[123-129] The BET surface areas were calculated to be 4178 m^2/g for PCN-228, 4935 m^2/g for PCN-229 and 7154 m^2/g for PCN-230 by Materials Studio 6.0 using the "atom volumes and surfaces" function. The inconsistency of experimental and calculated surface area comes from the difficulty in activation of ultra-high porosity material. The extremely large cavity can easily trap unreacted ligands and metal clusters which are difficult to remove during the activation process. From TGA curves, we can see that the weight loss of PCN-230 is smaller than that of PCN-229 after solvent removal at 100°C. Moreover, PCN-230 left more residue than PCN-229 after complete decomposition. This unusual phenomenon supports the idea that PCN-230 may contain bulky trapped species that could not be removed. Moreover, PCN-230 has the lowest stability among these MOFs, which also accounts for the unexpectedly low N_2 uptake compared with PCN-228 and PCN-229.

The MOFs reported in this work show high gravimetric surface area. Especially when the volumetric surface area is considered, PCN-228 is very outstanding among those well-known MOFs. Typically, the MOFs with large pore size possess relative low gravimetric and volumetric surface area. However, PCN-228 and PCN-229 possess much higher gravimetric and volumetric surface area compared with PCN-221 bearing much smaller pore size. The great improvement of both the volumetric and gravimetric surface areas can be ascribed to the replacement of the Zr_8 clusters with the smaller Zr_6 clusters. The low volumetric surface area of PCN-230 can be ascribed to its extremely low crystal density (0.189 g/cm^3). However, it is still comparable with PCN-221 which has higher density (0.48 g/cm^3) but much lower gravimetric surface area. Overall, this series of mesoporous MOFs possesses high and permanent porosity after removal of solvent molecules, demonstrating its excellent physical stability.

The Zr_6 cluster is fully occupied by twelve carboxylates from the porphyrinic linkers and gives rise to the highest connectivity among Zr-MOFs, hence this series of MOFs were expected to possess excellent chemical stability. We tested the chemical stability of PCN-230 as a representative, with consideration that MOF stability decreases along with the increase of the linker length for isoreticular structures. After being soaked in aqueous solutions with pH values ranging from 0 to 12 (prepared by HCl and NaOH solution respectively) for 24 hours, the PXRD patterns of PCN-230 are almost unaltered, which suggests maintenance of the crystallinity. To further confirm that the frameworks were intact, we performed N_2 adsorption measurement for samples after different treatments. N_2 uptake measurements of PCN-230 after treatment have minimal deviation

from the pristine sample, which indicates the robustness of the framework under harsh chemical conditions (Figure 42b). To our knowledge, PCN-230 shows the highest stability in the widest pH range among previously reported porphyrinic MOFs despite its extremely large linker. Stability tests of PCN-228 and PCN-229 treated with different aqueous solutions were also conducted (Figure 38 and Figure 39). The well maintained PXRD patterns of the samples after different treatments demonstrate that PCN-228 and PCN-229 are stable even in 1M HCl for 24 hours, displaying higher stability than PCN-230. This series of Zr-MOFs with elongated linkers successfully realize the combination of meso-porosity with high stability, and would be of great potential for application in nano-scale chemistry.

5.4 CONCLUSIONS

In conclusion, through topological and symmetry analysis, we developed a series of twelve-connected Zr_6 containing porphyrinic MOFs with ftw-a topology using elongated porphyrinic linkers. Among them, PCN-230 exhibits the largest cage (3.8nm) and PCN-229 shows both the highest porosity and BET surface area among previously reported Zr-MOFs. PCN-230, constructed with the largest linker, shows excellent stability in aqueous solutions with pH ranging from 0 to 12, which is the widest range among all porphyrinic MOFs.

6. SYNTHESIS OF A COPPER-BASED PORPHYRINIC MOF FROM MIXED LIGAND CO-ASSEMBLEY

Topological analysis suggests that the connectivity of an imidazolate porphyrinic linker would possess the necessary geometry to form a mesoporous MOF isostructural to the previous reported 12-connected Zr_6 series. In this study, an elongated porphyrin linker was readily synthesized through amine-dicarboxylic acid coupling. High-throughput synthesis was then used to construct PCN-355 through the previously discussed mixed-linker co-assembly approach. The structure was further evaluated through synchrotron powder and single crystal X-ray diffraction. PCN-355 also exhibits high N_2 uptake (~850 cm^3/g) at 77K and BET surface area (2264 m^2/g). No interpenetration is observed and the pore size of the MOF reaches 3.2 nm. Lastly, CO_2 and H_2 gas studies were performed to evaluate potential for gas storage applications.

6.1 INTRODUCTION

Porphyrinic MOFs are an interesting class of porous materials due to the potential to form MOFs with large surface areas and high porosity without the potential for interpenetrated structures.[107, 109-110, 130-131] Several porphyrinic MOFs are composed of mesopores, allowing potential use in a variety of applications including biomimetic catalysis, gas storage, enzyme immobilization, and sensing applications.[115, 132-135] Porphyrinic linkers in MOFs have recently been targeted due to the ability to incorporate functionality that closely mimics metalloproteins such as heme.[136] The porphyrin architectures can be further metalated to perform a wide array of catalytic functions with increased accessibility due to the porous nature of MOFs.[107, 112, 116]

In Section 5, a series of porphyrin MOFs with increased porosity was studied through the elongation of the porphyrin linker.[131] These MOFs demonstrate our ability to control pore size in the *ftw-a* topology; however, the synthesis of these elongated porphyrins is complex and requires multiple step reactions, expensive catalysts, and extensive purification procedures. Our approach is to use easily synthesized amine functionalized porphyrin that can easily be coupled to a benzimidazole moiety through an amine-dicarboxylic acid coupling reaction.[87] The elongated porphyrin used in this work is synthesized without the need of expensive catalyst and is easily collected through precipitation in water due to high conjugation. The addition of the benzimizaole group in this work through the green coupling reaction is a more efficient way of porphyrin elongation rather than the extension through palladium coupling.

6.2 EXPERIMENTAL SECTION[*]

General Information. Copper (II) Nitrate hemipentahydrate, N,N-dimethylacetamide (DMA), Pyrazole, 4-Nitrobenaldehyde, Pyrrole, Acetic Anhydride, Propionic Acid, Pyridine, Tin (II) Chloride, Chloroform, Hydrochloric Acid, Ammonium Hydroxide, Sodium Hydroxide, DMF, and Benzimidazole-5,6-dicarboxylic Acid were all purchased from commercially available sources and were used as received

Instrumentation. ^{1}H NMR data were collected on a Mercury 300 MHz NMR spectrometer. FT-IR data were recorded on an IRAffinity-1 instrument. TGA data were obtained on a TGA-50 (SHIMADZU) thermogravimetric analyzer with a heating rate of 3 °C min^{-1} under a N_2 atmosphere. The powder X-ray diffraction patterns (PXRD) were recorded on a BRUKER D8-Focus Bragg-Brentano X-ray Powder Diffractometer equipped with a Cu sealed tube (λ = 1.54178 Å) at room temperature. Synchrotron-based powder diffraction (APS) experiments were performed at the 17-BM beamline of the Advance Photon Source in Argonne National Laboratory.

[*] Ligand and MOF synthesis performed with assistance from Madison Haas and Mario Cosio. Structural studies were performed with assistance of Ying-Pin Chen, Dr. Yusheng Chen, Dr. Andrey Yakovenko, and Dr. Simon Teat.

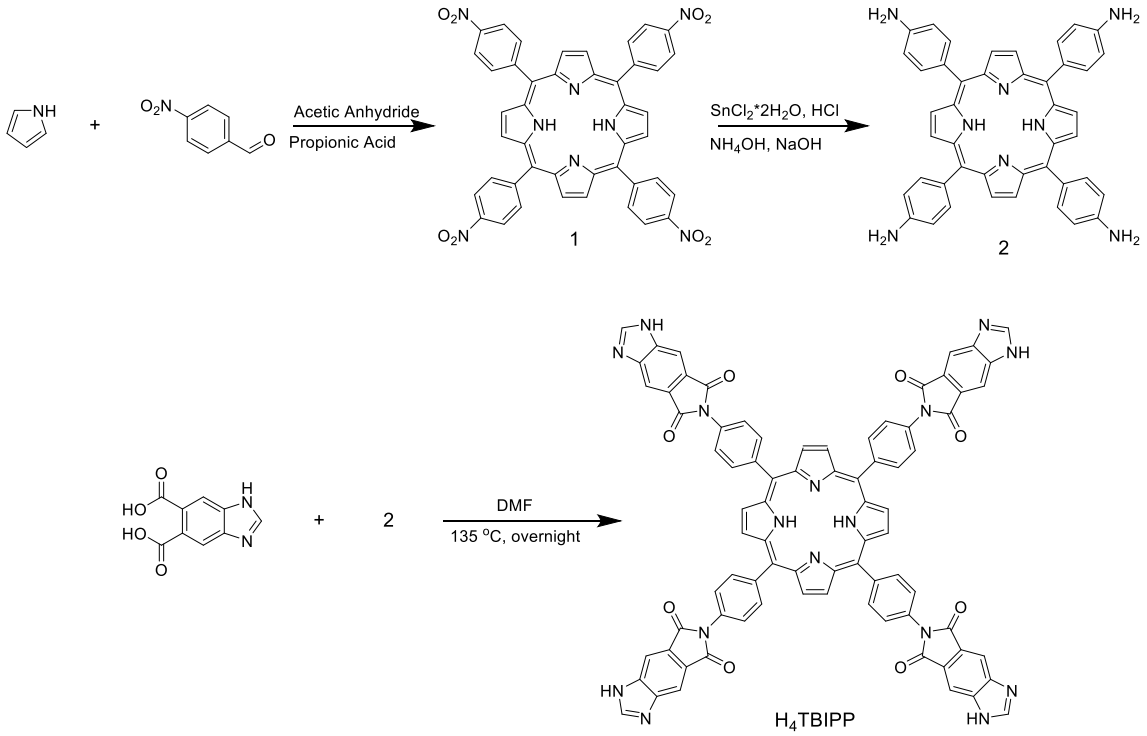

Scheme 9 Synthesis of **H_4TBIPP**.

Synthesis of 1, tetrakis(4-nitrophenyl)porphyrin (TNPP).[137]To a solution of acetic anhydride (12mL) and propionic acid (300mL) was added 4-nitrobenzaldehyde (11g, 73mmol). The solution was brought to reflux and pyrrole (5ml, 73mmol) was added to the reaction and further refluxed for 30 mins. The resulting reaction was filtered and cooled overnight. The solution was then filtered and washed with water (600mL) and dried under vacuum. The resulting powder was dissolved in pyridine (80mL) and refluxed for 1h and then placed in the freezer overnight. Upon filtering, a deep purple powder was recovered (2.1g, 15.4%) Mass Spec: Theoretical 794.19 m/z, Positive ion MALDI-MS Found: 795.20 m/z.

Synthesis of 2 tetrakis(4-aminophenyl)porphyrin (TAPP).[137] A solution of **1** (2.0 g, 2.5 mmol) in concentrated HCl (100mL) was bubbled under anhydrous nitrogen gas for 1h. Another solution of $SnCl_2*2H_2O$ (9g, 40mmol) in concentrated HCl (140mL) was also bubbled under anhydrous nitrogen gas for 1 h. The tin (II) chloride solution was then cannulated into the porphyrin solution and the refluxed for 30mins under nitrogen atmosphere. The resulting solution was cooled to room temperature in a water bath then cooled further in an ice bath. The reaction solution was brought into air and centrifuged. The resulting dark powder was treated with sodium hydroxide (5%, 200mL) and centrifuged. The powder was again washed with water and dried under vacuum. The dark powder was then Soxhlet extracted with chloroform (400mL) for 2 days, then concentrated to 150mL and ethanol (100mL) was added to the solution and evaporated to dryness. A dark purple powder was collected (1.6g, 94%). ^{1}H NMR (300 MHz, C_5D_5N) δ 5.26 (N-H, bs), 7.36 (8H, d), 8.20 (8H,d), 9.24 (8H, s), 14.0 (N-H, s). Mass Spec: Theoretical 674.29 m/z, Positive ion MALDI-MS found 675.47 m/z.

Synthesis of H_4TBIPP, tertrakis((4-imidazo[4,5]isoindole-5,7dione)phenyl)porphyrin (TBIPP).[87] **2** (1g, 1.48 mmol) was mixed with benzimidazole-5,6-dicarboxylic acid (1.22g, 5.93mmol) in DMF (75mL) and heated at 135^{o}C overnight. The solution was then washed with water and dried under vacuum to yield a metallic purple product (1.27g, 68%). ^{1}H NMR (300 MHz, DMSO-d5) δ 5.7 (N-H, bs), 8.28 (8H, d), 8.40 (8H,d), 9.01 (8H, s), 10.8 (N-H, s). Mass Spec: Theoretical 1355.29 m/z, Positive ion MALDI-MS 1355.27 m/z.

Low-pressure gas adsorption measurements. Gas sorption isotherm measurements were performed on ASAP 2020 and ASAP 2420 Surface Area and Pore Size Analyzers. As-synthesized samples of PCN-354 were immersed in dry ethyl ether for 24 h and the extract decanted. Fresh dry ethyl ether was subsequently added and the crystals remained in the solvent for an additional 24 h. Each sample was collected by decanting and the procedure repeated once more with dry ethyl ether. After the removal of ethyl ether by decanting, the samples were activated by drying under a dynamic vacuum at room temperature. Before the measurement, PCN-351 and PCN-352 was again further activated using the "degas" function of the surface area analyzer for 4 h at 25 °C. Other activation temperatures were tested, with the reported methods providing the best sorption properties.

High-throughput Synthesis. A Chemspeed SLT-II Swing synthetic platform was used for MOF synthesis. Chemspeed Autosuite was used for all programming and for workflow. Volumetric transfer was performed using Chemspeed syringes with accuracy ± 10μL. All starting materials were dissolved into stock solutions with fixed concentrations in DMA. The solutions were then mixed based on reaction parameters into borosilicate vials and heated for 3 days (Table 2). Multiple experiments were performed with optimal runs reported.

Synthesis of PCN-355. A mixture of H_4TBIPP (4.34 mg, .0032mmol) and $Cu(NO_3)_2 \cdot 2.5H_2O$ (37.2 mg, .16mmol), and Pyrazole (80mg, 1.28mmol) each in DMA were added to a 1 dram vial and the total was brought to 3mL using a robotic platform. The vial was sealed, heated to 100 °C for 3 days, and black cubic shaped crystals of PCN-

355 were collected, washed with DMA. Elemental analysis (%): found: C 37.68, H 4.41, N 21.18.

Table 2 Sample high-throughput synthesis conditions of PCN-355

	Metal			Linker			Pyrazole			Solvent
ID	eq	mmol	mL	eq	mmol	mL	eq	mmol	mL	mL
1	1	0.16	1	0.01	0.0016	0.4	2	0.32	0.2	1.4
2	1	0.16	1	0.02	0.0032	0.6	2	0.32	0.2	1.2
3	1	0.16	1	0.03	0.0048	0.8	2	0.32	0.2	1
4	1	0.16	1	0.04	0.0064	1	2	0.32	0.2	0.8
5	1	0.16	1	0.01	0.0016	0.4	4	0.64	0.4	1.2
6	1	0.16	1	0.02	0.0032	0.6	4	0.64	0.4	1
7	1	0.16	1	0.03	0.0048	0.8	4	0.64	0.4	0.8
8	1	0.16	1	0.04	0.0064	1	4	0.64	0.4	0.6
9	1	0.16	1	0.01	0.0016	0.4	6	0.96	0.6	1
10	1	0.16	1	0.02	0.0032	0.6	6	0.96	0.6	0.8
11	1	0.16	1	0.03	0.0048	0.8	6	0.96	0.6	0.6
12	1	0.16	1	0.04	0.0064	1	6	0.96	0.6	0.4
13	1	0.16	1	0.01	0.0016	0.4	8	1.28	0.8	0.8
14	1	0.16	1	0.02	0.0032	0.6	8	1.28	0.8	0.6
15	1	0.16	1	0.03	0.0048	0.8	8	1.28	0.8	0.4
16	1	0.16	1	0.04	0.0064	1	8	1.28	0.8	0.2
17	1	0.16	1	0.01	0.0016	0.4	10	1.6	1	0.6
18	1	0.16	1	0.02	0.0032	0.6	10	1.6	1	0.4
19	1	0.16	1	0.03	0.0048	0.8	10	1.6	1	0.2
20	1	0.16	1	0.04	0.0064	1	10	1.6	1	0

X-ray Crystallography. Single crystal X-ray structure determination of PCN-355 were performed at 173(2) K using the Advanced Photon Source on beamline 15ID-B at Argonne National Laboratory to obtain unit cell of the MOF. Synchrotron-based powder

diffraction (APS) experiments were performed at the 17-BM beamline of the Advance Photon Source in Argonne National Laboratory. The simulated PXRD spectra were obtained by the diffraction-crystal module of the Mercury program based on the simulated single-crystal data. The program is available free of charge via internet at http:/www.iucr.org.

Crystal data for PCN-355: dark black cubic, cubic, space group $Pm\bar{3}m$, a = 32.8353 b = 32.8353 c = 32.8353 α = 90 β =90 γ = 90

6.3 RESULTS AND DISCUSSION

High-throughput synthesis. In this study, a high-throughput synthetic protocol was used to synthesize a mesoporous porphyrinic MOF. Due to the high molecular weight of the H_2TIBPP linker, the concentration was decreased for these screening studies in order to maintain ligand-metal ratios and to avoid solubility issues. PCN-351 was synthesized at 100^{o}C in DMA. From the crystallization diagram, it was observed that at low molar concentrations of pyrazole and H_2TBIPP yield unidentifiable amorphous powder and mixed phase materials. Higher concentration of pyrazole (6 eq, 8 eq, and 10 eq) and low concentration of H_2TBIPP yield pure phase PCN-355 as verified by powder x-ray diffraction.

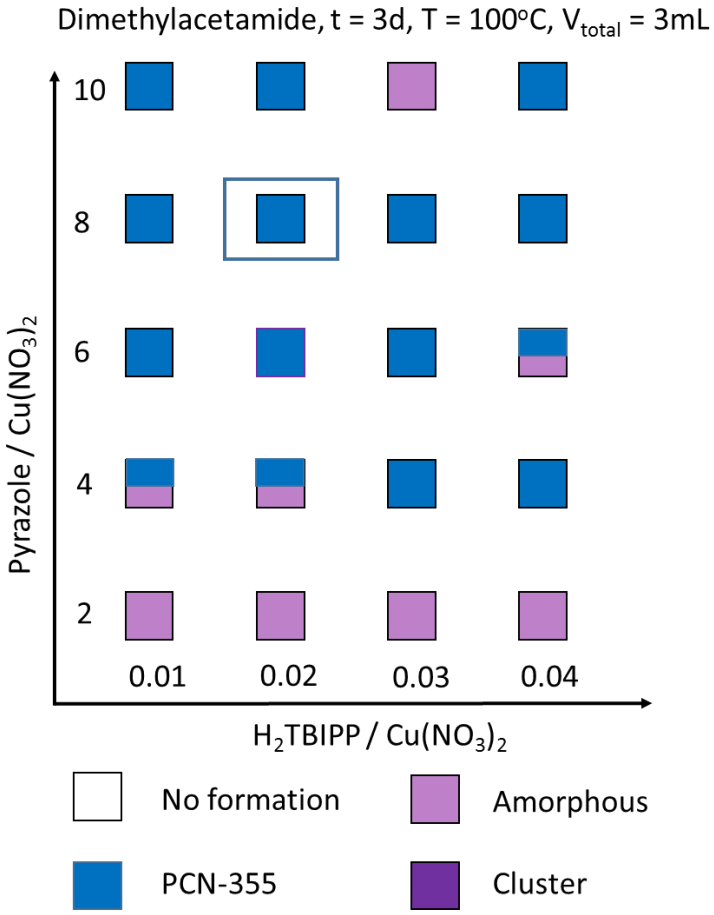

Figure 43 Crystallization diagrams for the high-throughput investigation of the system Pyrazole /$Cu(NO_3)_2$ and H_2TBIPP/$Cu(NO_3)_2$ in DMA at 100 ° C for 3 days based on powder XRD measurements.

Structural Studies. PCN-355 were performed using synchrotron X-ray diffraction due to the low electron density due to the large unit cell of the framework. PCN-355 was found to crystalize in the cubic unit cell $Pm\bar{3}m$, a = 32.8353 b = 32.8353 c = 32.8353 α = 90 β =90 γ = 90. PCN-355 is composed of the 12-connected cuboctahedron cages at the corners of the unit cell connected by bridging H_2TBIPP molecules (Figure 44). PCN-355

was further refined using GSASII (Figure 45) based on the topology of PCN-228.[131, 138] Refinement of the powder pattern with respect to the calculated patterns shows that the unit cell is well matched.

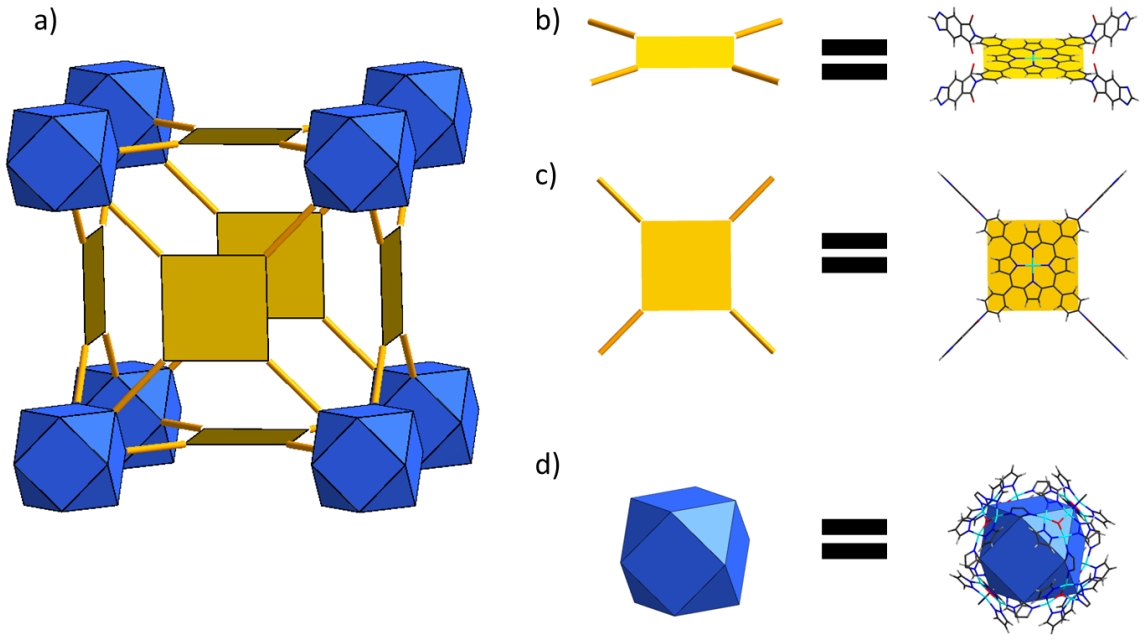

Figure 44 Structural representation of PCN-355 and packing of molecular cages. b) edge view of H2TBIPP linker, c) top view of H2TBIPP linker, d) 12-connected cuboctahedral node.

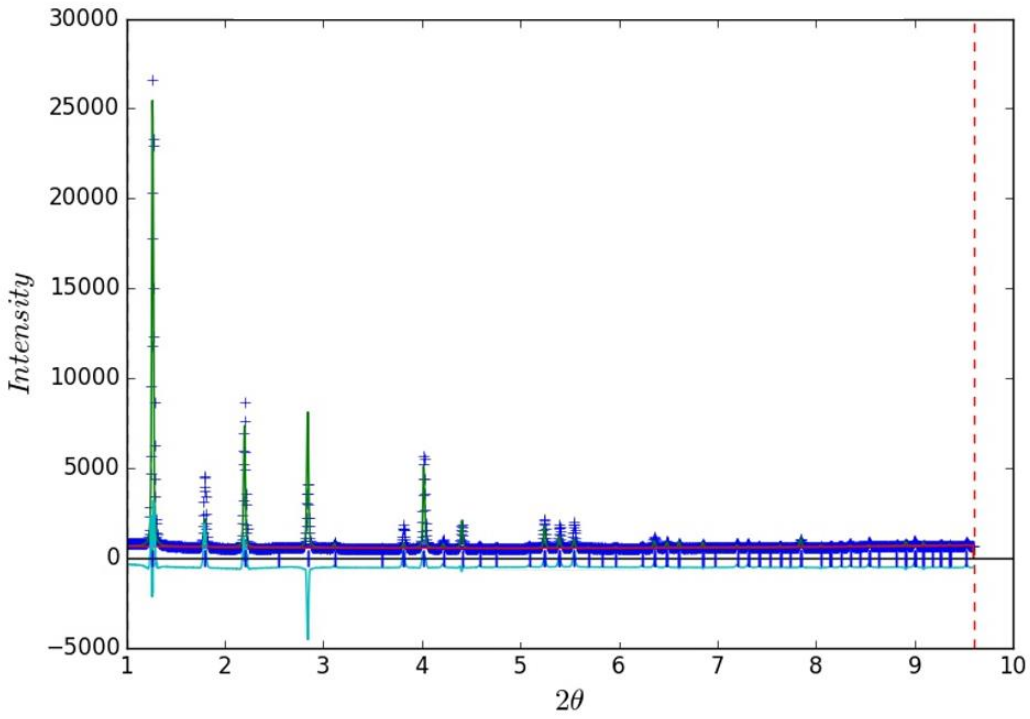

Figure 45 Pawley whole powder pattern decomposition for PCN-355. green line is the calculated pattern, dark blue line is experimental pattern, and turquoise line is difference in patterns.

Gas Studies. Due to the large mesopores within the structure, activation of the material for gas uptake can be challenging. Nitrogen isotherm at 77K was measured to determine surface area once activated by supercritical point CO_2 drying. PCN-353 exhibits a high uptake of N_2 (~850 cm^3/g at 1 bar) and surface area (2264 m^2/g). Moderate uptake of CO_2 and H_2 are observed with characteristic hysteresis due to capillary condensation of gases within the mesopores of the framework.

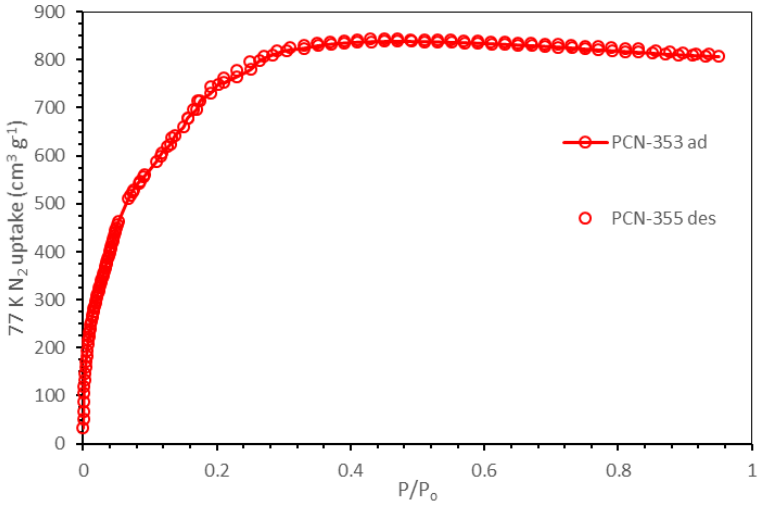

Figure 46 Nitrogen isotherms of PCN-355 measured at 77K.

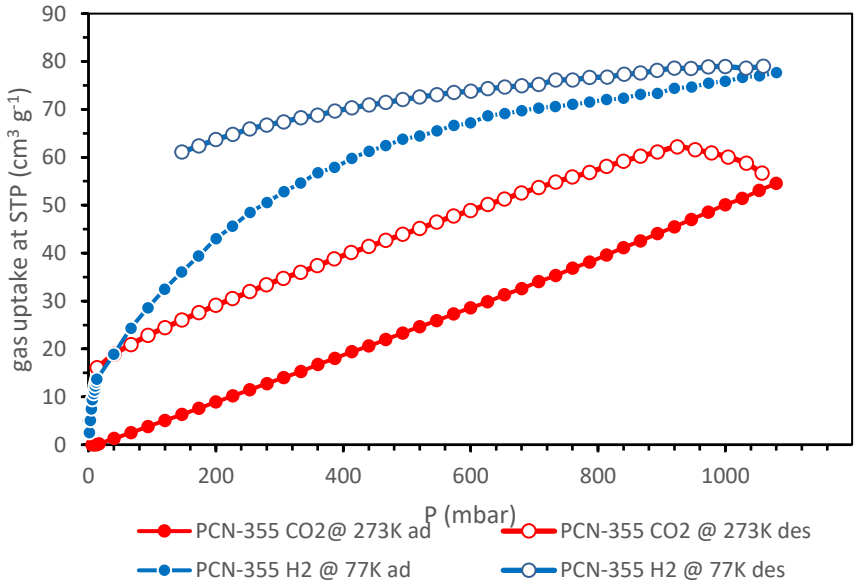

Figure 47 CO_2 and H_2 uptake isotherms of PCN-352 at 273K and 77K, respectively.

6.4 CONCLUSIONS

A new mesoporous porphyrinic MOF has been synthesized from a high-throughput screening protocol with mixed linker co-assembly. PCN-355 was characterized by combining synchrotron powder X-ray diffraction and single crystal X-ray. This MOF exhibits the expected 12-connected supramolecular building block connected through square planar porphyrin tetraimidazolate moieties. PCN-355 is isostructural to the previously reported Zr_6 MOF from Section 5 as expected. Gas studies were performed with PCN-355 possessing high N_2 uptake (~850 cm^3/g) and BET surface area (2264 m^2/g), and moderate H_2 and CO_2 uptake.

7. SUMMARY

In this dissertation, the synthesis of new metal-organic frameworks through rational topological design and high-throughput techniques have been studied. Utilizing a mixed-ligand co-assembly process, several new MOFs have been synthesized with a triangular copper (II) SBU not often readily observed in the MOF literature. The formation of new MOFs through combinatorial synthetic techniques has also been investigated with a Chemspeed® synthetic platform. In Section 2, an evaluation of combinatorial approaches to MOF synthesis was discussed.

In the following four sections, the synthesis of several new MOFs were investigated. Section 3 examines an approach to synthesize novel mixed-ligand MOF composed of cubic metal-organic polyhedral cages through topological design. PCN-351 was obtained with small channels and low porosity due to size and geometry of the H_2BBI linker. The extension of the linker to an elongated bis(imidazolate) provides some flexibility in the structure and PCN-352 was synthesized composed of molecular cages. In Section 4, high-throughput synthesis was used to investigate the synthesis of new MOFs through a mixed-linker approach with modulation reagents. Two new MOFs, PCN-353 and PCN-354, were synthesized using a high-throughput robotic platform. PCN-352 was used as starting point to optimize synthetic parameters with a pyridine modulating reagent. These new MOFs exhibit enhanced porosity and structural tuneability.

In Section 5, topological design was used to synthesize a new series of Zr_6 porphyrinic MOFs with enhanced porosity and stability. Lastly, in Section 6, a new

porphyrinic MOF composed from twelve connected molecular cage was synthesized and isostructural to the reported Zr_6 MOFs.

From these studies, topological design and high-throughput synthesis have been shown to be a powerful tools for the development of new materials. The mixed-ligand co-assembly process is an interesting new approach to synthesize MOFs where the SBU is formed with one ligand and then an additional linker connects the SBUs to form the framework. Nitrogen donor ligand are used to build upon the porosity of traditional carboxylate MOF, unfortunately in this system enhanced chemical stability is not observed. The synthesis of copper porphyrinic MOFs are rare and a new MOF has been synthesis with structural similarity to Zr_6 series.

Future work will explore the continued development of high-throughput synthetic protocols. A wealth of new MOF structures may exist using this mixed-linker approach. Judicious selection of the metal-nodes and linkers could yield futher interesting SBUs not readily observed in the literature. Examination of existing clusters in the literature combined with topological design and high-throughput synthesis will lead to the rapid development of materials with tuneable structural feature for a wide array of applications.

REFERENCES

(1) Batten, S. R.; Champness, N. R.; Chen, X.-M.; Garcia-Martinez, J.; Kitagawa, S.; Öhrström, L.; O'Keeffe, M.; Paik Suh, M.; Reedijk, J. Terminology of metal–organic frameworks and coordination polymers (IUPAC Recommendations 2013). In *Pure and Applied Chemistry*, 2013; Vol. 85, pp 1715-1724.

(2) Kitagawa, S.; Kitaura, R.; Noro, S.-i. *Angewandte Chemie International Edition* **2004,** *43* (18), 2334-2375.

(3) Zhang, M.; Chen, Y.-P.; Bosch, M.; Gentle, T.; Wang, K.; Feng, D.; Wang, Z. U.; Zhou, H.-C. *Angewandte Chemie International Edition* **2014,** *53* (3), 815-818.

(4) Lee, J.; Farha, O. K.; Roberts, J.; Scheidt, K. A.; Nguyen, S. T.; Hupp, J. T. *Chemical Society Reviews* **2009,** *38* (5), 1450-1459.

(5) Murray, L. J.; Dinca, M.; Long, J. R. *Chemical Society Reviews* **2009,** *38* (5), 1294-1314.

(6) Zhou, H.-C.; Long, J. R.; Yaghi, O. M. *Chemical Reviews* **2012,** *112* (2), 673-674.

(7) Lee, Y.-R.; Kim, J.; Ahn, W.-S. *Korean J. Chem. Eng.* **2013,** *30* (9), 1667-1680.

(8) Makal, T. A.; Yuan, D.; Zhao, D.; Zhou, H. C. Metal-Organic Frameworks. In *The Chemistry of Nanostructured Materials*, Yang, P., Ed. World Scientific: Singapore, 2011; Vol. II, pp 37-64.

(9) Biemmi, E.; Christian, S.; Stock, N.; Bein, T. *Microporous and Mesoporous Materials* **2009,** *117* (1–2), 111-117.

(10) Li, H.; Eddaoudi, M.; O'Keeffe, M.; Yaghi, O. M. *Nature* **1999,** *402* (6759), 276-279.

(11) Eddaoudi, M.; Kim, J.; Rosi, N.; Vodak, D.; Wachter, J.; O'Keeffe, M.; Yaghi, O. M. *Science* **2002,** *295* (5554), 469-72.

(12) Chui, S. S.-Y.; Lo, S. M.-F.; Charmant, J. P. H.; Orpen, A. G.; Williams, I. D. *Science* **1999,** *283* (5405), 1148-1150.

(13) Férey, G.; Mellot-Draznieks, C.; Serre, C.; Millange, F.; Dutour, J.; Surblé, S.; Margiolaki, I. *Science* **2005,** *309* (5743), 2040-2042.

(14) Cavka, J. H.; Jakobsen, S.; Olsbye, U.; Guillou, N.; Lamberti, C.; Bordiga, S.; Lillerud, K. P. *Journal of the American Chemical Society* **2008,** *130* (42), 13850-13851.

(15) Tranchemontagne, D. J.; Mendoza-Cortes, J. L.; O'Keeffe, M.; Yaghi, O. M. *Chemical Society Reviews* **2009,** *38* (5), 1257-83.

(16) Lu, W.; Wei, Z.; Gu, Z. Y.; Liu, T. F.; Park, J.; Park, J.; Tian, J.; Zhang, M.; Zhang, Q.; Gentle, T., 3rd; Bosch, M.; Zhou, H. C. *Chemical Society Reviews* **2014,** *43* (16), 5561-93.

(17) Gagnon, K. J.; Perry, H. P.; Clearfield, A. *Chemical Reviews* **2011,** *112* (2), 1034-1054.

(18) Shimizu, G. K. H.; Vaidhyanathan, R.; Taylor, J. M. *Chemical Society Reviews* **2009,** *38* (5), 1430-1449.

(19) Eddaoudi, M.; Kim, J.; Rosi, N.; Vodak, D.; Wachter, J.; O'Keeffe, M.; Yaghi, O. M. *Science* **2002,** *295* (5554), 469-472.

(20) Yaghi, O. M.; O'Keeffe, M.; Ockwig, N. W.; Chae, H. K.; Eddaoudi, M.; Kim, J. *Nature* **2003,** *423* (6941), 705-714.

(21) Caskey, S. R.; Wong-Foy, A. G.; Matzger, A. J. *Journal of the American Chemical Society* **2008,** *130* (33), 10870-10871.

(22) Rosi, N. L.; Kim, J.; Eddaoudi, M.; Chen, B.; O'Keeffe, M.; Yaghi, O. M. *Journal of the American Chemical Society* **2005,** *127* (5), 1504-1518.

(23) Deng, H.; Grunder, S.; Cordova, K. E.; Valente, C.; Furukawa, H.; Hmadeh, M.; Gándara, F.; Whalley, A. C.; Liu, Z.; Asahina, S.; Kazumori, H.; O'Keeffe, M.; Terasaki, O.; Stoddart, J. F.; Yaghi, O. M. *Science* **2012,** *336* (6084), 1018-1023.

(24) Férey, G.; Serre, C.; Mellot-Draznieks, C.; Millange, F.; Surblé, D. S. J.; Margiolaki, I. *Angewandte Chemie International Edition* **2004,** *43*, 6296.

(25) Kim, M.; Cahill, J. F.; Su, Y.; Prather, K. A.; Cohen, S. M. *Chemical Science* **2012,** *3* (1), 126.

(26) Wang, C.; Wang, J. L.; Lin, W. *Journal of the American Chemical Society* **2012,** *134* (48), 19895-908.

(27) Cundy, C. S.; Cox, P. A. *Chemical Reviews* **2003,** *103* (3), 663-702.

(28) Phan, A.; Doonan, C. J.; Uribe-Romo, F. J.; Knobler, C. B.; O'Keeffe, M.; Yaghi, O. M. *Accounts of Chemical Research* **2010,** *43* (1), 58-67.

(29) Pimentel, B. R.; Parulkar, A.; Zhou, E.-k.; Brunelli, N. A.; Lively, R. P. *ChemSusChem* **2014,** *7* (12), 3202-3240.

(30) Chen, B.; Yang, Z.; Zhu, Y.; Xia, Y. *Journal of Materials Chemistry A* **2014,** *2* (40), 16811-16831.

(31) Yao, J.; Wang, H. *Chemical Society Reviews* **2014,** *43* (13), 4470-4493.

(32) O'Keeffe, M.; Peskov, M. A.; Ramsden, S. J.; Yaghi, O. M. *Accounts of Chemical Research* **2008,** *41* (12), 1782-1789.

(33) Park, K. S.; Ni, Z.; Côté, A. P.; Choi, J. Y.; Huang, R.; Uribe-Romo, F. J.; Chae, H. K.; O'Keeffe, M.; Yaghi, O. M. *Proceedings of the National Academy of Sciences* **2006,** *103* (27), 10186-10191.

(34) O'Keeffe, M.; Eddaoudi, M.; Li, H.; Reineke, T.; Yaghi, O. M. *Journal of Solid State Chemistry* **2000,** *152* (1), 3-20.

(35) Baerlocher, C.; McCusker, L. B.; Olson, D. H. *Atlas of Zeolite Framework Types*. 6th revised ed. ed.; 2007.

(36) Wang, K.; Lv, X.-L.; Feng, D.; Li, J.; Chen, S.; Sun, J.; Song, L.; Xie, Y.; Li, J.-R.; Zhou, H.-C. *Journal of the American Chemical Society* **2016,** *138* (3), 914-919.

(37) Xu, L.; Wang, J.; Xu, Y.; Zhang, Z.; Lu, P.; Fang, M.; Li, S.; Sun, P.; Liu, H.-K. *CrystEngComm* **2014,** *16* (37), 8656-8659.

(38) Delgado-Friedrichs, O.; O'Keeffe, M. *Acta Crystallographica Section A* **2007,** *63* (4), 344-347.

(39) Delgado-Friedrichs, O.; O'Keeffe, M.; Yaghi, O. M. *Acta Crystallographica Section A* **2006,** *62* (5), 350-355.

(40) Padial, N. M.; Quartapelle Procopio, E.; Montoro, C.; López, E.; Oltra, J. E.; Colombo, V.; Maspero, A.; Masciocchi, N.; Galli, S.; Senkovska, I.; Kaskel, S.; Barea, E.; Navarro, J. A. R. *Angewandte Chemie International Edition* **2013,** *52* (32), 8290-8294.

(41) Xu, J.-Y.; Qiao, X.; Song, H.-B.; Yan, S.-P.; Liao, D.-Z.; Gao, S.; Journaux, Y.; Cano, J. *Chemical Communications* **2008,** (47), 6414-6416.

(42) Zhang, J.-P.; Zhang, Y.-B.; Lin, J.-B.; Chen, X.-M. *Chemical Reviews* **2012,** *112* (2), 1001-1033.

(43) McDonald, T. M.; D'Alessandro, D. M.; Krishna, R.; Long, J. R. *Chemical Science* **2011,** *2* (10), 2022-2028.

(44) Tonigold, M.; Lu, Y.; Mavrandonakis, A.; Puls, A.; Staudt, R.; Möllmer, J.; Sauer, J.; Volkmer, D. *Chemistry – A European Journal* **2011,** *17* (31), 8671-8695.

(45) Masciocchi, N.; Galli, S.; Colombo, V.; Maspero, A.; Palmisano, G.; Seyyedi, B.; Lamberti, C.; Bordiga, S. *Journal of the American Chemical Society* **2010,** *132* (23), 7902-7904.

(46) Stock, N. *Microporous and Mesoporous Materials* **2010,** *129* (3), 287-295.

(47) Klinowski, J.; Almeida Paz, F. A.; Silva, P.; Rocha, J. *Dalton Transactions* **2011,** *40* (2), 321-330.

(48) Maniam, P.; Stock, N. *Inorganic Chemistry* **2011,** *50* (11), 5085-5097.

(49) Stock, N.; Biswas, S. *Chemical Reviews* **2012,** *112* (2), 933-969.

(50) Accelerator Dual Dosing Station. Chemspeed Ltd.: Augst, Switzerland, 2003.

(51) Chen, S.-C.; Zhang, Z.-H.; Huang, K.-L.; Chen, Q.; He, M.-Y.; Cui, A.-J.; Li, C.; Liu, Q.; Du, M. *Crystal Growth & Design* **2008,** *8* (9), 3437-3445.

(52) Hennigar, T. L.; MacQuarrie, D. C.; Losier, P.; Rogers, R. D.; Zaworotko, M. J. *Angewandte Chemie International Edition in English* **1997,** *36* (9), 972-973.

(53) Withersby, M. A.; Blake, A. J.; Champness, N. R.; Cooke, P. A.; Hubberstey, P.; Li, W.-S.; Schröder, M. *Inorganic Chemistry* **1999,** *38* (10), 2259-2266.

(54) Yaghi, O. M.; Davis, C. E.; Li, G.; Li, H. *Journal of the American Chemical Society* **1997,** *119* (12), 2861-2868.

(55) Park, J.; Feng, D.; Zhou, H.-C. *Journal of the American Chemical Society* **2015,** *137* (36), 11801-11809.

(56) Yuan, S.; Qin, J.-S.; Zou, L.; Chen, Y.-P.; Wang, X.; Zhang, Q.; Zhou, H.-C. *Journal of the American Chemical Society* **2016**.

(57) Feng, D.; Wang, K.; Wei, Z.; Chen, Y.-P.; Simon, C. M.; Arvapally, R. K.; Martin, R. L.; Bosch, M.; Liu, T.-F.; Fordham, S.; Yuan, D.; Omary, M. A.; Haranczyk, M.; Smit, B.; Zhou, H.-C. *Nature Communications* **2014,** *5*.

(58) Bauer, S.; Serre, C.; Devic, T.; Horcajada, P.; Marrot, J.; Férey, G.; Stock, N. *Inorganic Chemistry* **2008,** *47* (17), 7568-7576.

(59) Bao, Y.; Martin, R. L.; Haranczyk, M.; Deem, M. W. *Physical Chemistry Chemical Physics* **2015,** *17* (18), 11962-11973.

(60) Forster, P. M.; Stock, N.; Cheetham, A. K. *Angewandte Chemie International Edition* **2005,** *44* (46), 7608-7611.

(61) Lammert, M.; Bernt, S.; Vermoortele, F.; De Vos, D. E.; Stock, N. *Inorganic Chemistry* **2013,** *52* (15), 8521-8528.

(62) Reinsch, H.; Stock, N. *Microporous and Mesoporous Materials* **2013,** *171*, 156-165.

(63) Reinsch, H.; Waitschat, S.; Stock, N. *Dalton Transactions* **2013,** *42* (14), 4840-4847.

(64) Pagis, C.; Ferbinteanu, M.; Rothenberg, G.; Tanase, S. *ACS Catalysis* **2016,** *6* (9), 6063-6072.

(65) Caminade, A.-M.; Hey-Hawkins, E.; Manners, I. *Chemical Society Reviews* **2016,** *45* (19), 5144-5146.

(66) Li, B.; Chrzanowski, M.; Zhang, Y.; Ma, S. *Coordination Chemistry Reviews* **2016,** *307, Part 2*, 106-129.

(67) Mohamedali, M.; Nath, D.; Ibrahim, H.; Henni, A. Review of Recent Developments in CO2 Capture Using Solid Materials: Metal Organic Frameworks (MOFs). In *Greenhouse Gases*, InTech: Rijeka, 2016; p Ch. 0.

(68) Wang, X.; Fordham, S.; Zhou, H.-C. Metal−Organic Frameworks for Methane Storage. In *Nanomaterials for Sustainable Energy*, American Chemical Society: 2015; Vol. 1213, pp 173-191.

(69) Liu, T.-F.; Zou, L.; Feng, D.; Chen, Y.-P.; Fordham, S.; Wang, X.; Liu, Y.; Zhou, H.-C. *Journal of the American Chemical Society* **2014,** *136* (22), 7813-7816.

(70) Liu, Y.; Howarth, A. J.; Hupp, J. T.; Farha, O. K. *Angewandte Chemie International Edition* **2015,** *54* (31), 9001-9005.

(71) Marx, S.; Kleist, W.; Huang, J.; Maciejewski, M.; Baiker, A. *Dalton Transactions* **2010,** *39* (16), 3795-3798.

(72) Deng, H.; Doonan, C. J.; Furukawa, H.; Ferreira, R. B.; Towne, J.; Knobler, C. B.; Wang, B.; Yaghi, O. M. *Science* **2010,** *327* (5967), 846.

(73) Xie, Y.; Yang, H.; Wang, Z. U.; Liu, Y.; Zhou, H.-C.; Li, J.-R. *Chemical Communications* **2014,** *50* (5), 563-565.

(74) Chen, Y.-P.; Liu, T.-F.; Fordham, S.; Zhou, H.-C. *Acta Crystallographica Section B* **2015,** *71* (6), 613-618.

(75) Viciano-Chumillas, M.; Tanase, S.; de Jongh, L. J.; Reedijk, J. *European Journal of Inorganic Chemistry* **2010,** *2010* (22), 3403-3418.

(76) Britt, D.; Furukawa, H.; Wang, B.; Glover, T. G.; Yaghi, O. M. *Proceedings of the National Academy of Sciences* **2009,** *106* (49), 20637-20640.

(77) Liu, J.; Thallapally, P. K.; McGrail, B. P.; Brown, D. R.; Liu, J. *Chemical Society Reviews* **2012,** *41* (6), 2308-2322.

(78) Zhang, M.; Li, H.; Perry, Z.; Zhou, H.-C. Metal–Organic Frameworks: Gas Storage. In *Encyclopedia of Inorganic and Bioinorganic Chemistry*, John Wiley & Sons, Ltd: 2011.

(79) Tranchemontagne, D. J.; Ni, Z.; O'Keeffe, M.; Yaghi, O. M. *Angewandte Chemie International Edition* **2008,** *47* (28), 5136-5147.

(80) Boydston, A. J.; Williams, K. A.; Bielawski, C. W. *Journal of the American Chemical Society* **2005,** *127* (36), 12496-12497.

(81) Fagan, V.; Bonham, S.; Carty, M. P.; Aldabbagh, F. *Organic & Biomolecular Chemistry* **2010,** *8* (14), 3149-3156.

(82) Sheldrick, G. *Acta Crystallogr. Sect. A: Found. Crystallogr.* **2008,** *64* (1), 112-122.

(83) Spek, A. *Journal of Applied Crystallography* **2003,** *36* (1), 7-13.

(84) Hu, Z.; Zhang, K.; Zhang, M.; Guo, Z.; Jiang, J.; Zhao, D. *ChemSusChem* **2014,** *7* (10), 2791-2795.

(85) Savonnet, M.; Kockrick, E.; Camarata, A.; Bazer-Bachi, D.; Bats, N.; Lecocq, V.; Pinel, C.; Farrusseng, D. *New Journal of Chemistry* **2011,** *35* (9), 1892-1897.

(86) Sun, Y.; Zhou, H.-C. *Science and Technology of Advanced Materials* **2015,** *16* (5), 054202.

(87) Yang, J.-S.; Zhu, J.; Liu, R.-B.; Ni, J.; Chang, Z.-D.; Hu, T.; Zhang, J.-J.; Meng, C.-G. *Inorganica Chimica Acta* **2013,** *394*, 117-126.

(88) Nelson, A. P.; Farha, O. K.; Mulfort, K. L.; Hupp, J. T. *Journal of the American Chemical Society* **2009,** *131* (2), 458-460.

(89) Chen, Y.; Lykourinou, V.; Vetromile, C.; Hoang, T.; Ming, L.-J.; Larsen, R. W.; Ma, S. *Journal of the American Chemical Society* **2012,** *134* (32), 13188-13191.

(90) Hwang, Y. K.; Hong, D.-Y.; Chang, J.-S.; Jhung, S. H.; Seo, Y.-K.; Kim, J.; Vimont, A.; Daturi, M.; Serre, C.; Férey, G. *Angewandte Chemie International Edition* **2008,** *47* (22), 4144-4148.

(91) Zhou, H. C.; Kitagawa, S. *Chemical Society Reviews* **2014,** *43*, 5415-5418.

(92) Zhu, Q.-L.; Xu, Q. *Chemical Society Reviews* **2014,** *43* (16), 5468-5512.

(93) Schaate, A.; Roy, P.; Preuße, T.; Lohmeier, S. J.; Godt, A.; Behrens, P. *Chemistry – A European Journal* **2011,** *17* (34), 9320-9325.

(94) Pearson, R. G. *Journal of the American Chemical Society* **1963,** *85* (22), 3533-3539.

(95) Furukawa, H.; Gándara, F.; Zhang, Y.-B.; Jiang, J.; Queen, W. L.; Hudson, M. R.; Yaghi, O. M. *Journal of the American Chemical Society* **2014,** *136* (11), 4369-4381.

(96) Guillerm, V.; Ragon, F.; Dan-Hardi, M.; Devic, T.; Vishnuvarthan, M.; Campo, B.; Vimont, A.; Clet, G.; Yang, Q.; Maurin, G.; Férey, G.; Vittadini, A.; Gross, S.; Serre, C. *Angewandte Chemie International Edition* **2012,** *51* (37), 9267-9271.

(97) Horcajada, P.; Surble, S.; Serre, C.; Hong, D.-Y.; Seo, Y.-K.; Chang, J.-S.; Greneche, J.-M.; Margiolaki, I.; Ferey, G. *Chemical Communications* **2007,** (27), 2820-2822.

(98) Jiang, H.-L.; Feng, D.; Liu, T.-F.; Li, J.-R.; Zhou, H.-C. *Journal of the American Chemical Society* **2012,** *134* (36), 14690-14693.

(99) Lieb, A.; Leclerc, H.; Devic, T.; Serre, C.; Margiolaki, I.; Mahjoubi, F.; Lee, J. S.; Vimont, A.; Daturi, M.; Chang, J.-S. *Microporous and Mesoporous Materials* **2012,** *157*, 18-23.

(100) Mondloch, J. E.; Bury, W.; Fairen-Jimenez, D.; Kwon, S.; DeMarco, E. J.; Weston, M. H.; Sarjeant, A. A.; Nguyen, S. T.; Stair, P. C.; Snurr, R. Q.; Farha, O. K.; Hupp, J. T. *Journal of the American Chemical Society* **2013,** *135* (28), 10294-10297.

(101) Volkringer, C.; Popov, D.; Loiseau, T.; Férey, G.; Burghammer, M.; Riekel, C.; Haouas, M.; Taulelle, F. *Chemistry of Materials* **2009,** *21* (24), 5695-5697.

(102) Wang, C.; Xie, Z.; deKrafft, K. E.; Lin, W. *Journal of the American Chemical Society* **2011,** *133* (34), 13445-13454.

(103) Wei, Z.; Gu, Z.-Y.; Arvapally, R. K.; Chen, Y.-P.; McDougald, R. N.; Ivy, J. F.; Yakovenko, A. A.; Feng, D.; Omary, M. A.; Zhou, H.-C. *Journal of the American Chemical Society* **2014,** *136* (23), 8269-8276.

(104) Farha, O. K.; Eryazici, I.; Jeong, N. C.; Hauser, B. G.; Wilmer, C. E.; Sarjeant, A. A.; Snurr, R. Q.; Nguyen, S. T.; Yazaydın, A. Ö.; Hupp, J. T. *Journal of the American Chemical Society* **2012,** *134* (36), 15016-15021.

(105) Yuan, D.; Zhao, D.; Sun, D.; Zhou, H.-C. *Angewandte Chemie International Edition* **2010,** *49* (31), 5357-5361.

(106) Wang, C.; Wang, J.-L.; Lin, W. *Journal of the American Chemical Society* **2012,** *134* (48), 19895-19908.

(107) Feng, D.; Gu, Z.-Y.; Li, J.-R.; Jiang, H.-L.; Wei, Z.; Zhou, H.-C. *Angewandte Chemie International Edition* **2012,** *51* (41), 10307-10310.

(108) Alkordi, M. H.; Liu, Y.; Larsen, R. W.; Eubank, J. F.; Eddaoudi, M. *Journal of the American Chemical Society* **2008,** *130* (38), 12639-12641.

(109) Burnett, B. J.; Barron, P. M.; Choe, W. *CrystEngComm* **2012,** *14* (11), 3839-3846.

(110) Gao, W.-Y.; Chrzanowski, M.; Ma, S. *Chemical Society Reviews* **2014,** *43* (16), 5841-5866.

(111) Lee, C. Y.; Farha, O. K.; Hong, B. J.; Sarjeant, A. A.; Nguyen, S. T.; Hupp, J. T. *Journal of the American Chemical Society* **2011,** *133* (40), 15858-15861.

(112) Meng, L.; Cheng, Q.; Kim, C.; Gao, W.-Y.; Wojtas, L.; Chen, Y.-S.; Zaworotko, M. J.; Zhang, X. P.; Ma, S. *Angewandte Chemie International Edition* **2012,** *51* (40), 10082-10085.

(113) Park, J.; Feng, D.; Yuan, S.; Zhou, H.-C. *Angewandte Chemie International Edition* **2015,** *54* (2), 430-435.

(114) Son, H.-J.; Jin, S.; Patwardhan, S.; Wezenberg, S. J.; Jeong, N. C.; So, M.; Wilmer, C. E.; Sarjeant, A. A.; Schatz, G. C.; Snurr, R. Q.; Farha, O. K.; Wiederrecht, G. P.; Hupp, J. T. *Journal of the American Chemical Society* **2013,** *135* (2), 862-869.

(115) Zou, C.; Wu, C.-D. *Dalton Transactions* **2012,** *41* (14), 3879-3888.

(116) Chen, Y.; Hoang, T.; Ma, S. *Inorganic Chemistry* **2012,** *51* (23), 12600-12602.

(117) Fateeva, A.; Chater, P. A.; Ireland, C. P.; Tahir, A. A.; Khimyak, Y. Z.; Wiper, P. V.; Darwent, J. R.; Rosseinsky, M. J. *Angewandte Chemie International Edition* **2012,** *51* (30), 7440-7444.

(118) Feng, D.; Chung, W.-C.; Wei, Z.; Gu, Z.-Y.; Jiang, H.-L.; Chen, Y.-P.; Darensbourg, D. J.; Zhou, H.-C. *Journal of the American Chemical Society* **2013,** *135* (45), 17105-17110.

(119) Feng, D.; Jiang, H.-L.; Chen, Y.-P.; Gu, Z.-Y.; Wei, Z.; Zhou, H.-C. *Inorganic Chemistry* **2013,** *52* (21), 12661-12667.

(120) Morris, W.; Volosskiy, B.; Demir, S.; Gándara, F.; McGrier, P. L.; Furukawa, H.; Cascio, D.; Stoddart, J. F.; Yaghi, O. M. *Inorganic Chemistry* **2012,** *51* (12), 6443-6445.

(121) Sheldrick, G. M. *Acta Crystallographica Section A* **2008,** *64* (1), 112-122.

(122) Okuyama, K.; Hasegawa, T.; Ito, M.; Mikami, N. *The Journal of Physical Chemistry* **1984,** *88* (9), 1711-1716.

(123) Chowdhury, P.; Mekala, S.; Dreisbach, F.; Gumma, S. *Microporous and Mesoporous Materials* **2012,** *152*, 246-252.

(124) Farha, O. K.; Özgür Yazaydın, A.; Eryazici, I.; Malliakas, C. D.; Hauser, B. G.; Kanatzidis, M. G.; Nguyen, S. T.; Snurr, R. Q.; Hupp, J. T. *Nature Chemistry* **2010,** *2* (11), 944-948.

(125) Furukawa, H.; Ko, N.; Go, Y. B.; Aratani, N.; Choi, S. B.; Choi, E.; Yazaydin, A. Ö.; Snurr, R. Q.; O'Keeffe, M.; Kim, J.; Yaghi, O. M. *Science* **2010,** *329* (5990), 424-428.

(126) Kaye, S. S.; Dailly, A.; Yaghi, O. M.; Long, J. R. *Journal of the American Chemical Society* **2007,** *129* (46), 14176-14177.

(127) Koh, K.; Wong-Foy, A. G.; Matzger, A. J. *Journal of the American Chemical Society* **2009,** *131* (12), 4184-4185.

(128) Mason, J. A.; Veenstra, M.; Long, J. R. *Chemical Science* **2014,** *5* (1), 32-51.

(129) Wiersum, A. D.; Chang, J.-S.; Serre, C.; Llewellyn, P. L. *Langmuir* **2013,** *29* (10), 3301-3309.

(130) Feng, D.; Gu, Z.-Y.; Chen, Y.-P.; Park, J.; Wei, Z.; Sun, Y.; Bosch, M.; Yuan, S.; Zhou, H.-C. *Journal of the American Chemical Society* **2014,** *136* (51), 17714-17717.

(131) Liu, T.-F.; Feng, D.; Chen, Y.-P.; Zou, L.; Bosch, M.; Yuan, S.; Wei, Z.; Fordham, S.; Wang, K.; Zhou, H.-C. *Journal of the American Chemical Society* **2015,** *137* (1), 413-419.

(132) Farha, O. K.; Shultz, A. M.; Sarjeant, A. A.; Nguyen, S. T.; Hupp, J. T. *Journal of the American Chemical Society* **2011,** *133* (15), 5652-5655.

(133) Llewellyn, P. L.; Bourrelly, S.; Serre, C.; Vimont, A.; Daturi, M.; Hamon, L.; De Weireld, G.; Chang, J.-S.; Hong, D.-Y.; Kyu Hwang, Y.; Hwa Jhung, S.; Férey, G. *Langmuir* **2008,** *24* (14), 7245-7250.

(134) Song, L.; Zhang, J.; Sun, L.; Xu, F.; Li, F.; Zhang, H.; Si, X.; Jiao, C.; Li, Z.; Liu, S.; Liu, Y.; Zhou, H.; Sun, D.; Du, Y.; Cao, Z.; Gabelica, Z. *Energy & Environmental Science* **2012,** *5* (6), 7508-7520.

(135) Xuan, W.; Zhu, C.; Liu, Y.; Cui, Y. *Chemical Society Reviews* **2012,** *41* (5), 1677-1695.

(136) Anderson, J. S.; Gallagher, A. T.; Mason, J. A.; Harris, T. D. *Journal of the American Chemical Society* **2014,** *136* (47), 16489-16492.

(137) Bettelheim, A.; White, B. A.; Raybuck, S. A.; Murray, R. W. *Inorganic Chemistry* **1987,** *26* (7), 1009-1017.

(138) Toby, B. H.; Von Dreele, R. B. *Journal of Applied Crystallography* **2013,** *46* (2), 544-549.